RICE UNIVERSITY

Photothermoelectric response and hot carrier tunneling in gold nanowires

by

Mahdiyeh Abbasi

A THESIS SUBMITTED
IN PARTIAL FULFILLMENT OF THE
REQUIREMENTS FOR THE DEGREE

Doctor of Philosophy

APPROVED, THESIS COMMITTEE

Douglas Natelson, Chair
Professor of Physics & Astronomy,
Electrical & Computer Engineering, and
Material Science & Nanoengineering

Peter Nordlander
Professor of Physics & Astronomy,
Electrical & Computer Engineering, and
Materials Science & Nanoengineering

Junichiro Kono,
Professor of Electrical & Computer
Engineering, Physics & Astronomy, and
Materials Science & Nanoengineering

HOUSTON, TEXAS
August 2021

ABSTRACT

Photothermoelectric effect and hot electron tunneling in gold nanowires

by

Mahdiyeh Abbasi

The thermoelectric effect is the conversion of electrical to thermal energy and vice versa. In the photothermoelectric effect (PTE), photons are used as a heat source to apply a temperature distribution. Photodetectors based on PTE can be made. If we wisely choose noble metals in our PTE-based photodetectors, we can use the plasmonic characteristic of the metals to our benefit. Plasmons are the incompressible oscillation of electrons that can be excited by (coupled to) light. These oscillations have different energy levels and they depend on the geometry as well as the permittivity of the metal. All plasmon modes can decay nonradiatively and produce heat. Dipolar plasmon modes can couple to the far field. In the first section of this thesis, the design, simulation, and experimental results of single metal (gold) photodetectors that operate based on dipolar plasmon modes of gold nanowires are discussed. Later we discuss how PTE voltages in single-crystal nanowires are sensitive to lattice distortions and trace impurities. As a result, PTE measurement can be used to detect internal properties of gold nanowire. Using COMSOL simulations we can characterize the internal strain as well as platinum impurity concentration in gold single crystalline nanowires.

In the second part of the thesis, we consider the effects on plasmon modes in nanogaps, both in the generation of light through inelastic tunneling, and in their photovoltage response that can be used for photodetection. A nanowire may be broken to form a nanogap. That nanogap, thanks to broken geometrical symmetry, can host localized plasmon modes of a variety of energies. These modes can be excited either by applied light or by inelastic tunneling of electrons under an applied voltage. When these plasmon modes decay, they produce electron-hole pairs. Radiative recombination of these pairs can cause light emission out of the gap. This light emission is shaped by the plasmonic characteristics of the metallic nanostructure. In the presence of high current densities, so that the energy of more than one inelastically excited plasmon can be present at a time in the junction region, the emitted light can be above threshold (photon energy greater than the applied voltage). Here, the simulations of characterizing the plasmonic modes of these nanogaps are discussed.

The localized plasmon modes can be excited by light and can be detected by measuring the open circuit voltage thanks to two different mechanisms. In an unbroken nanowire, an optically generated temperature gradient leads to a PTE voltage. In nanogap structures, hot carrier tunneling can also lead to an open circuit photovoltage. The open circuit voltage after forming the gap is up to 1000× stronger than the PTE voltage in an unbroken nanowire. When the gap is formed, local plasmon modes can be excited. These modes decay and produce hot carriers, these hot carriers tunnel across the gap from one electrode to the other. An open circuit voltage develops to counterbalance this hot electron current. When both

electrodes are made from same metal (same electrical permittivity) and same geometry, the hot carriers don't have a preferred tunneling direction. So, the polarity of the net open circuit voltage is completely random from device to device and depends on the small changes in gap geometry. If the direction of hot carrier tunneling in these devices can be controlled, we can make photodetectors that ×100 times faster with ×1000 times higher responsivity. Here we show the experimental results of preferred hot carrier tunneling direction in gold, platinum MIM structure.

Acknowledgments

“Even after all this time, the sun never says to the earth: You own me! Look what happens with a kindness like that, it lights up the whole sky… “ -Hafiz

This thesis is dedicated to my parents, Mahtab and Ahmad, who put my future before their comfort.

I would like to thank my dear Ph.D. advisor, Prof. Douglas Natelson, whose guidance and passion for science have consistently helped me find my way through difficult problems. Prof. Natelson is very kind and, at the same time, very professional and knowledgeable, which I find a rare and valuable combination to have. I would like to thank current and previous members of the Natelson Lab that I could always benefit from their knowledge and insight: Yunxuan Zhu, Dr. Longji Cui, Dr. Charlotte I. Evans, Liyang Chen, Dr. Xifan Wang, Dr. Pavlo Zolotavin, Dr. Jiawei Yang, Xuanhan Zhao, Dr. Loah Stevens, Dr. Panpan Zhou, Dr. Kenneth Evans, Dale T. Lowder, Renjie Luo, and Shusen Liao.

I would like to thank my Ph.D. committee members, Prof. Douglas Natelson, Prof. Peter Nordlander, and Prof. Junichiro Kono, for their valuable feedbacks and insights on this thesis and my scientific path.

In the past five years, I had the honor to learn from other incredible professors and scientists here at Rice University: Dr. Alessandro Alabastri, Dr. Gururaj Naik, Dr, Jacob T. Robinson, Prof. Behnaam Aazhang, Prof. Frank K. Tittel, Ali Mojibpour, and Dr. Jian Yang. I would like to appreciate our collaborators at

Stanford University: Prof. Jonathan Fan, Lucia T. Gan, Dr. Rui Yang. I would like to thank Bella Martinez and Aki Shimada from the ECE department for their patience and hard work.

Thank you to my dearest friend, Niloofar, for her unstoppable support during every moment that I needed her. I feel so grateful to have supportive and loving friends during these years that without them, taking this path could have been impossible: Omid, Niloofar, Zahra Farhadi, Mahtab, Mohammad, Anahita, Navid, Sahar, Sahand, Atefeh, Yasaman, Hamed, Mina, Zahra Firoozi, Hoorivash, Setareh, Mahdieh, Eduardo, Kshipra, Amruta, Gloria, Negar, Negin, Farzane, and Sogol. I greatly appreciate having Omid on my side during these years. How far he can go to help others and be kind has always surprised me.

I appreciate having a family that is proud and supportive of me; my mother, Mahtab, who barely has missed a day in the past five years to send me at least a 'good morning' message right on time even with a 9-hour time difference, my father, Ahmad, who is supportive of me and my goals, my brother, Mehran, and my sister-in-law, Hastee who are funny, kind, and intelligent, my aunt, Behjat, and my uncle, Mohsen, may he rest in peace, for being supportive of the path that I took. I hope I can pave the way, as the first person who has moved to another country, for future possibilities for my young family members.

Contents

List of Figures

List of Equations

Nomenclature

TE	Thermoelectric effect
PTE	Photothermoelectric effect
COMSOL	COMSOL Multiphysics simulation software
EWFD	Electromagnetic wave, Frequency domain
HT	Heat Transfer
EC	Electric current
FDTD	Finite Difference Time Domain
FEM	Finite Element Method
MIM	Metal-Insulator-Metal
MDM	Metal-Dielectric-Metal
MOM	Metal-Oxide-Metal
NIR	Near-Infrared
FWHM	Full Width Half Maximum
SEM	Scanning Electron Microscope
STM	Scanning Tunneling Microscopy
LSP	Localized Surface Plasmons
LSPR	Localized surface plasmons resonance
SPP	Surface Plasmon Polaritons
PV	Photovoltage
PD	Photodetector
DOS	Density of states

e-h pair	electron-hole pair

Chapter 1

Introduction

The thermoelectric effect is the conversion of electrical to thermal energy and vice versa, and it is of great interest in energy harvesting[1], [2], cooling mechanisms based on the Peltier effect where applied voltage changed the temperature distribution[2], and photodetectors based on the Seebeck effect where temperature distribution causes the electrons to flow[3]. In the photothermoelectric effect or PTE, photons are used to produce thermal energy and a temperature gradient, and then electrical energy.

Photodetectors can be made based on the PTE effect[4]–[6]. Photodetectors based on the PTE effect do not require external bias (no 1/f noise) and cooling units, as they utilize thermal energy to produce an electric signal. The noise of PTE photodetectors is limited by Johnson-Nyquist noise[5]. Plasmons, the incompressible oscillations of the electron liquid in metals, can be utilized to make metallic PTE-based photodetectors spectrally sensitive. On the other hand, the Mott

formula in metals [7] shows that at the nanoscale where the dimensions are in the same order of the mean free path of electrons, it is possible to make single metal thermocouples by changing the geometry across the material. Chapter 2 focuses on the essential physical background of the concepts discussed in all the subsequent chapters. Concepts like TE, PTE, Plasmons, plasmon decay, and electron tunneling in MIM are discussed in this Chapter.

COMSOL simulation results are key to the experiments discussed in Chapters 4, 5, and 7. Chapter 3 guides us through the theories of light mater interaction, heat transfer in solids, and electrical signal used in these simulation models.

The fabrication of these single metal photodetectors that are spectrally sensitive can be simpler than production of semiconductor PTE-based photodetectors. Chapter 4 is about PTE-based photodetectors. In this chapter, experiments and COMSOL simulation results of a single metal photodetector are discussed. We engineer the geometry of these photodetectors in a way to respond differently at different wavelengths based on activation of plasmons in the metallic nanowire as well as the spatially varying Seebeck coefficient map across the device. In this chapter, the responsivity and detectivity of these single metallic PTE-based photodetectors are compared with semiconductor PTE-based photodetectors.

Other than geometry, Seebeck response can be changed by internal properties that can alter the carrier propagation and scattering, factors like internal strain and impurity concentrations[8]. PTE measurement can be utilized to detect the internal properties of metallic nanowires with great accuracy. Chapter 5 focuses

on using COMSOL simulations and experiments to characterize the internal strain and crystal misorientation as well as Pt impurity gradients in single-crystalline gold nanowires, based on the effect on the PTE signal.

It is possible to improve the responsivity, detectivity, and response time of metal-based photodetectors by introducing hot carrier tunneling in metal-insulator-metal (MIM) nanostructures. Chapter 6 shows my experimental results for MIM structures with dissimilar metallic electrodes. Metallic electrodes are made from gold and platinum. Experimental data show that by exciting plasmon modes in the gold electrodes, it is possible to control the directionality of hot carrier tunneling in these planar tunnel junctions. These hot carriers are created by the decay of localized multipolar plasmon modes. [9], [10]

Other than optical excitation of multipolar plasmon modes, we can excite these modes by applying a voltage across the MIM nanostructure[11], [12]. Chapter 7 shows these high-energy plasmon modes make above threshold light emission possible. This chapter focuses on COMSOL simulation results of plasmonic characteristics of these MIM structures.

Finally, Chapter 8 concludes our discussion and mentions the potential application of this thesis.

Chapter 2

Photothermoelectric effect/Plasmons/Electron tunneling

2.1. Thermoelectric effect

Thermoelectric studies are focused on electrical to thermal energy conversion and vice versa. The thermoelectric effect (TE) can be used for energy harvesting[1], [2], the cooling mechanism in refrigerators [2], producing voltage through a thermocouple [3]. For optimizing the behavior of each mechanism, detailed knowledge on charge transfer and thermal transfer in our structure is necessary.

TEs may be grouped into three subcategories: the Peltier effect, which is the use of electric current to pump thermal energy; the Seebeck effect, which is the conversion of thermal energy to electric energy; and the Thomson effect, which is heat production of a current-carrying conductor with a temperature gradient. In this thesis, the focus of Chapters 4, and 5 are on the Seebeck effect. As introduction, all three subcategories are introduced as follows.

2.1.1. Peltier effect and Thomson effect

In Peltier effect, an applied electrical current, causes a temperature gradient across the material (the opposite conversion direction to what happens in Seebeck effect.) Fig. 2.1.a shows the Peltier effect. The direction of applied current forces a temperature gradient between two ends of the structure. Peltier effect can be used as the cooling mechanisms in refrigerators. In Peltier effect the heat generated per unit time is calculated as:

Equation 2.1. Peltier effect

$$\dot{Q} = \Pi I$$

In which Π is the Peltier coefficient and is linearly changes with Seebeck effect by a temperature coefficient.

Equation 2.2. Peltier coefficient

$$\Pi = ST$$

In Thomson effect, both temperature profile and electrical current are applied. This effect is shown in Fig. 2.1b. In this case the heat generated per unit time is calculated as shown below.

Equation 2.3. Thomson effect

$$\dot{Q} = -\mathrm{K}J(T_{hot} - T_{cold})$$

The Thomson coefficient K depends on temperature and Seebeck change due to temperature gradient:

Equation 2.4. Thomson coefficient

$$\mathrm{K} = T\frac{dS}{dT}$$

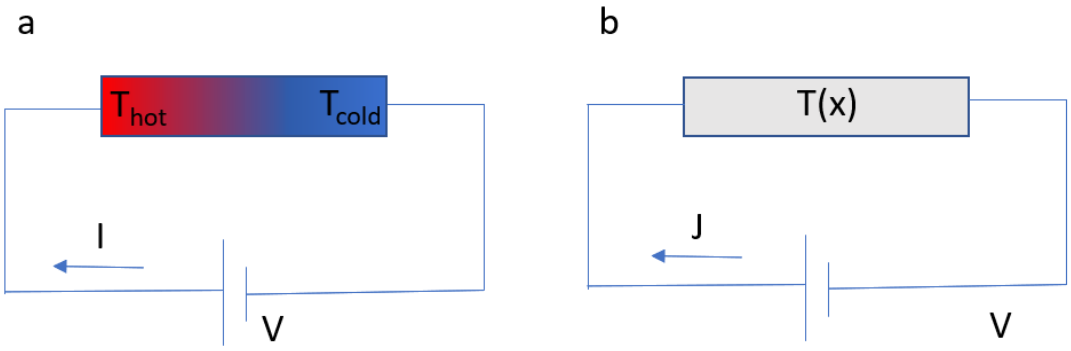

Figure 2.1. a) Peltier effect. b) Thomson effect

In this thesis, out of three thermoelectric subcategories, we utilize the Seebeck effect shown below. Note what happens in Joule heating is that the current flows and it causes dissipated heat and so produces a temperature gradient. Joule

heating is not the same as thermoelectric effects shown here. Thermoelectric effects are all thermodynamically reversable vs Joule heating which is not.

2.1.2. Seebeck effect

A temperature gradient in a material drives the diffusion of charge carriers and vibrational energy in material from hot to cold and perturbs the system's equilibrium. High temperature (high T) spreads electronic population out over a wider range of energies around the Fermi level, based on Fermi-Dirac distribution of electrons. Fermi-Dirac distribution shows the average number of electrons in one quantum state with energy E at temperature T:[13]

Equation 2.5. Fermi-Dirac Distribution

$$f(E) = \frac{1}{e^{\frac{E-\mu}{k_B T}} + 1}$$

where k_B is the Boltzmann constant, μ is the chemical potential. A temperature gradient tends to favor the diffusion of electrons from regions of high temperature. Free electrons can move with this diffusion force. In an open-circuit situation, there must be no net flow of current (J as current density is zero in Eqn. 2.6), so that an internal electric field due to the free electrons' movement must produce a drift current that opposes the diffusion. Also, electron-phonon scattering can cause phonons to drag electrons from the hot side to the cold side as an extra force. This is called the phonon drag and its contribution should be considered in the Seebeck coefficient definition; phonon drag can be a dominant Seebeck

contribution near a material's Debye temperature[14], [15]. Due to the perturbed charge concentration across the system, an open voltage circuit can be measured at a steady state when the material is isolated. This is called the Seebeck effect, and the open-circuit voltage that is produced can be calculated as shown in Eqn. 2.7, in which S is the Seebeck coefficient and ∇T is the temperature difference at two ends of the material.

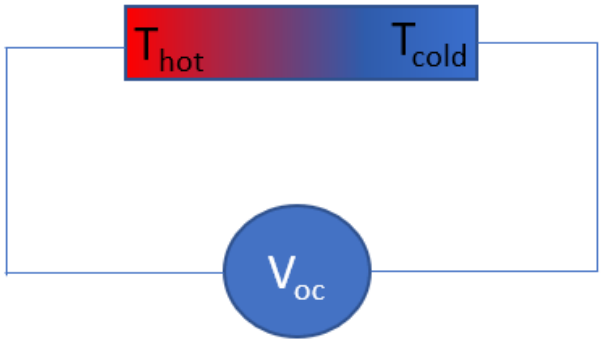

Figure 2.2. Seebeck effect. When there's a temperature gradient, in open circuit wiring, the system will build up an open circuit voltage to counteract the diffusion force of electrons.

Equation 2.6. Total current density.

$$J = -\sigma \nabla V - \sigma S \nabla T$$

Equation 2.7. Seebeck effect

$$\nabla V = -S\nabla T$$

If there are two materials with different intrinsic thermoelectric properties, in case of applying a temperature gradient between the junction of the materials and their ends, the open-circuit voltage can be calculated as the multiplication of temperature difference and difference between Seebeck coefficients. Fig. 3 shows the thermocouple structure and the open-circuit voltage produced in a thermocouple is shown in Eqn.2.8.

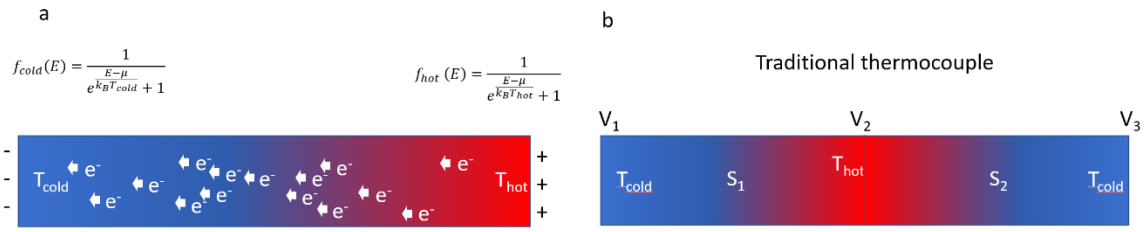

Figure 2.3. a) Electron population gets spread to higher energies at the high-temperature side of material based on Fermi-Dirac distribution and that causes the electron diffusion across materials. b) Two materials in electrical and thermal contact can make a thermocouple.

Equation 2.8. Open circuit of traditional thermocouple shown in Figure 2.3.b.

$$V_3 - V_1 = -(S_2 - S_1) \times (T_{hot} - T_{cold})$$

The structure in Fig. 2.2b is called a thermocouple, and these have been broadly used in research and industry since their 1820 discovery. The Seebeck effect can also be measured via the short-circuit thermoelectric current (I_{sc}) for the case of shorting the two ends of the circuit and measuring the current going through. Alternately, the open circuit voltage V_{oc} may be measured with an ideal voltmeter and no net charge current flowing. *Isc* can easily be converted to V_{oc} by multiplying by the resistance of the circuit. The Seebeck coefficient depends on all the scattering mechanisms in a metal. So, in our study where we study the Seebeck effect in Chapters 4 and 5, we measure open circuit voltages instead of short circuit currents.

The Seebeck coefficient depends on the diffusion of charge carriers, the variation of the chemical potential with temperature, and phonon drag, and all are related to the electronic structure and density of states in the conductor. As it is discussed further in the next sections, thermocouples from a single material can be made by engineering the intrinsic properties like adding impurities, or structural properties like changing the geometry; both can affect the charge carrier scattering properties and hence change the Seebeck coefficient.

2.1.2.1. Seebeck effect in metals

The Seebeck coefficient for metals and degenerate semiconductors can be calculated by Mott's formula[7] which calculates the electronic contribution to *S*, which usually dominates at room temperature. Electron scattering can affect the carrier mean free path.[16]

Equation 2.9. Mott formula for metals [7]

$$S = -\frac{\pi^2 k_B^2 T}{3e}\left(\frac{d\ ln\sigma}{dE}\right)_{E=E_f}$$

Here σ is the electrical conductivity, k_B is the Boltzmann constant, T is temperature, e is the electron charge, E is energy and E_f is the Fermi energy of the metal. Electrical conductivity in metals is related to the mean free path of the electrons. At the nanoscale, where the boundaries in geometry can be comparable to the mean free path of electrons, the electrical conductivity of the metal can be manipulated by engineering the geometry, and therefore the Seebeck coefficient as well. Previous studies have shown that it is possible to create a thermocouple with a single metal [6], [17], [18] with changes in sample geometry. Another factor that can change the Seebeck coefficient is the addition of impurities, because this affects both the band structure and the electronic scattering processes within the material [16]. Surface modification of the nanostructure can also change the Seebeck coefficient[19]. In Chapter 5 characterizing Seebeck coefficient change by internal strain and Pt impurity in single-crystalline gold nanowires are discussed.

2.1.2.2. Single metal thermocouples

A traditional thermocouple is composed of two dissimilar metals with different Seebeck coefficients. Based on Mott formula (Eqn. 2.9), S depends on energy dependent electrical conductivity:

Equation 2.10. Electrical conductivity of a metal[5]

$$\sigma = \frac{e^2 l S_F}{12\pi^2 \hbar}$$

where l is the mean free path of the electron, S_F is the area of the Fermi surface and $\hbar$ is the reduced Planck's constant. When the size of the metal structure is small enough to exhibit the size effect, the scatterings related to the surface and grain boundary will lead to the reduction in the mean free path [18]. in other words, by changing the geometry of metal at the nanoscale, it is possible to change the electrical conductivity and so the Seebeck coefficient. Single metal thermocouples have been made by changing the width of the metallic nanowire[4], [6], [17], [18], [20]. Recent studies in Natelson Lab, investigate single metal thermocouples made from gold nanowires and a fanout gold electrode[21]–[23]. When the nanowire length is less than the laser spot size, the PTE response is antisymmetric due to the symmetric Seebeck map across the device[21], [22]. Decreasing the thermal conductivity to the substrate can increase the open circuit signal, which proves the PTE origin of the open-circuit voltage. [22], [24]

Fig. 2.4 a and b show a thermocouple made from Ni [17]. The *S* changes where the width of the nanowire abruptly changes. By applying current heaters, they heat up due to Joule heating and can heat up the thermocouple junction. With the same electrical wiring, heating up the opposite thermocouple junction can make opposite polarity of open circuit voltage. And when both heaters are on, the opposite polarities of open circuit voltages cancel out and a zero net voltage is produced.

In this thesis photoresponses of metallic-based structures are studied. In what follows we consider TE photoresponse in semiconductors for comparison.

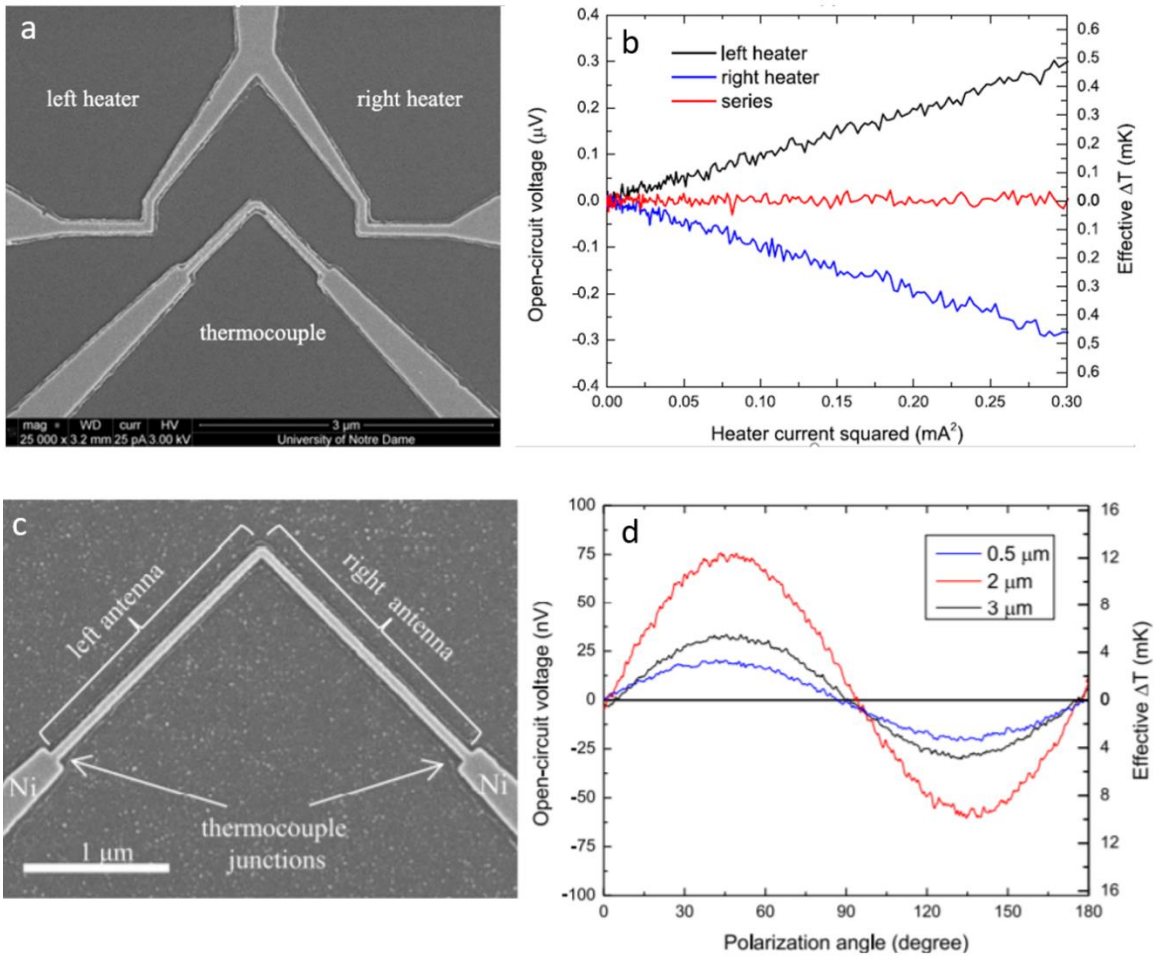

Figure 2.4. single metal thermocouple made from Ni - first row: TE response measured using fixed heaters. [17] Second row: PTE response of single metal Ni structure as a function of polarization of incident light and length of antenna structures.[6]

2.1.2.3. Seebeck effect in semiconductors

In metals, the electronic states near the Fermi level contribute to electronic current. Because the electronic bands in metals are relatively flat near the Fermi level, *S* can be low comparing to semiconductors [1], [25]. In semiconductors, *S* can be

engineered by changing the doping [25], [26]and applying a gate voltage [27], [28] as well as changing the geometry.

Photocurrents in semiconductors can have different origins. They can be due to PTE[3] , or by separation of photoexcited electron-hole pairs across the Schottky barrier at the semiconductor with metallic electrode interface [27], hot carrier tunneling at the Schottky barrier[29] , or based on photovoltaic effects at *p*-*n* junctions (as in conventional solar cells[30]).

2.1.3. Figure of Merit

Studies focused on thermal energy conversion to electrical energy are an opportunity to gain benefits from what would otherwise be considered waste heat. While thermodynamics imposes limitations on efficiency, in the bigger picture, if thermal energy can be vastly converted to useful energies, we can decrease demand for fossil fuels and reduce impact on the environment. Materials that can harvest the waste thermal energy should have high Seebeck coefficient (S) and high electrical conductivity (σ) as well as low thermal conductivity (k). This combination adds up to a high *figure of merit*. The thermoelectric figure of merit is a dimensionless factor that comprehensively evaluate the thermoelectric conversion efficiency of materials, also known as ZT, that can be calculated as: [31]

Equation 2.11. Figure of Merit

$$ZT = \frac{\sigma S^2 T}{k}$$

Metals are less of interest in energy harvesting because their electrical and thermal conductivities are both dominated by the conduction electrons (based on the Wiedemann-Franz Law[32]), and therefore are not independent. Semiconductors are a better choice for energy harvesting materials for higher ZT[1] because their Seebeck coefficient and thermal conductivity can be almost decoupled. At low dimensions, because of the relative size of the electron and phonon contributions, the thermal conductivity can decrease with almost fixed electrical conductivity, that is why 2D[33] and 1D [2], [26], [34] semiconductor structures have higher ZT. Optimization of the figure of merit is not the focus of this study.

2.2. Photothermoelectric effect and its application

The photothermoelectric effect is combination of photothermal heating and the thermoelectric effect. In PTE response, the temperature gradient across the material is caused by heating due to incoming photons. Photodetectors based on the PTE can be made[5]. One important point of utilizing light in the TE response is that we can excite plasmons. In Chapter 4 focuses on PTE based single metal photodetectors that are sensitive to wavelength and polarization of the incoming light due to plasmon resonances. In Chapter 5, the PTE response of the single crystalline gold nanowire can be used to map internal strain and impurity concentration gradients.

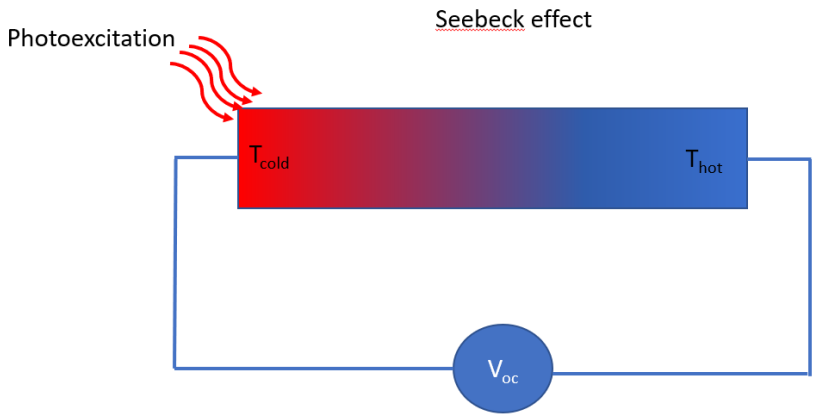

Figure 2.5. Photothermoelectric effect

2.3. Plasmons

Plasmons are the collective oscillations of the incompressible electronic fluid in metals. Like many wave-like excitations, plasmons can be propagating or localized. Depending on the spatial distribution of plasmonic charge motion, there can be a strong coupling between the metallic nanostructure and the incoming light. By controlling plasmon oscillations, we can manipulate matter and light interaction at the nanometer scale, and this opens a new era of application in optical sensing.

2.3.1. Localized Surface Plasmons (LSPs)

In the case of metallic structures much smaller than the incident wavelength, localized surface plasmon resonances (LSPR) can also be excited [35], [36] and the nanostructure collects light from an area larger than its physical size[29], [37]. The frequency of a LSPR for a spherical particle, which is a good reference for comparison, can be calculated as [38], [39]:

Equation 2.12. LSPR frequency

$$\omega_{LSPR} = \frac{1}{2\pi}\sqrt{\frac{ne^2}{\varepsilon_0 m_e(\varepsilon_\infty + 2\varepsilon_d)}}$$

where ε_0 is free space permittivity, ε_∞ is the high-frequency dielectric constant, ε_d is the dielectric constant of medium, and m_e is the effective mass of free carriers and n is the 3D carrier density. Under resonant excitation, the photons strongly couple with the plasmon, and the electromagnetic field is confined around the metal nanostructure, resulting in the increase of the absorption across the metallic nano structure. As shown above, LSPR frequency depends on the dielectric function of the metal and the surrounding. LSPR sensing can be used to find the permittivity of a surrounding medium with unknown permittivity [40], [41]. At certain wavelengths, LSPR oscillations can be controlled with the shape and size of the metallic structure[24], [42], [43]. The resulting light concentration on subwavelength scales can be used in different areas like surface-enhanced Raman spectroscopy[44] and surface chemistry[45].

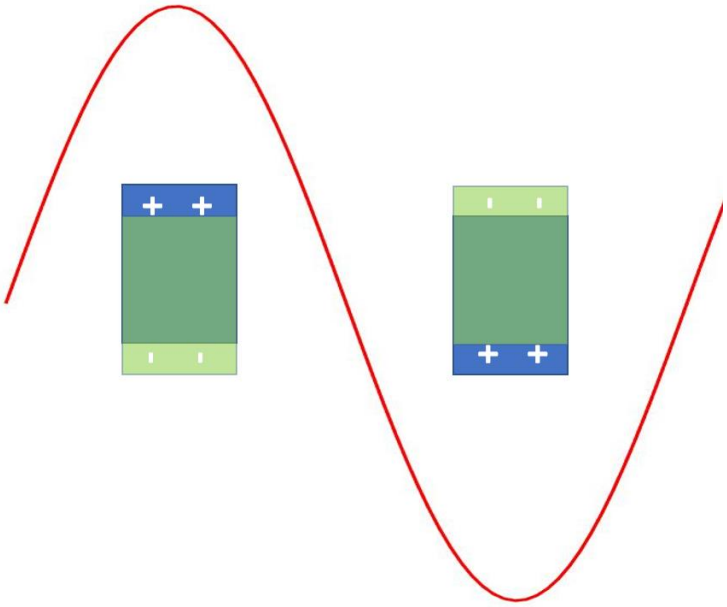

Figure 2.6. Localized Surface Plasmons excited with periodic force from incoming light. Oscillation of electrons is at the opposite direction of applied fiel due to negative charge of electrons.

2.3.2. Propagating Surface Plasmons

At the surface of a metal, a propagating plasmon, called a surface plasmon polariton (SPP)[38], can be excited that can travel around hundreds of nanometers (depending on the metal dielectric function and excitation wavelength) and decay evanescently. To couple light with these modes, the momentum and energy conservation need to be fulfilled; in other words, the dispersion relation of the optical excitation should have an intersect with dispersion relation of the SPP. This can be done either by using a high-index prism to support the momentum matching condition [46], [47] or by breaking the symmetry on the surface through making gratings.[23], [48], [49]

SPPs can be used in remote excitation when heating directly can be destructive to the structure.[23], [48] SPPs can also couple to the LSPs when propagating and this can enhance the remote excitation further[23]. By using near-field photocurrent technology, it is possible to image these propagating plasmons.[50]

2.3.3. Plasmon modes

Plasmons that involve a substantial oscillating dipole moment are known as optically “bright” modes, as they can couple well with optical excitation. Other modes, often involving higher-order multiples, lack an oscillating electric dipole and are known as dark modes [10] . Plasmons have wide applications in various fields like sensors,[4], [29], [36], [51]–[55] photothermal therapies [55], thermal optical data storage, and solar thermal energy harvesting [36]. Materials with negative real and small positive imaginary dielectric are capable of supporting surface plasmon resonance (SPR), and noble metals tend to support good plasmon resonances[36] in the visible and near-infrared.

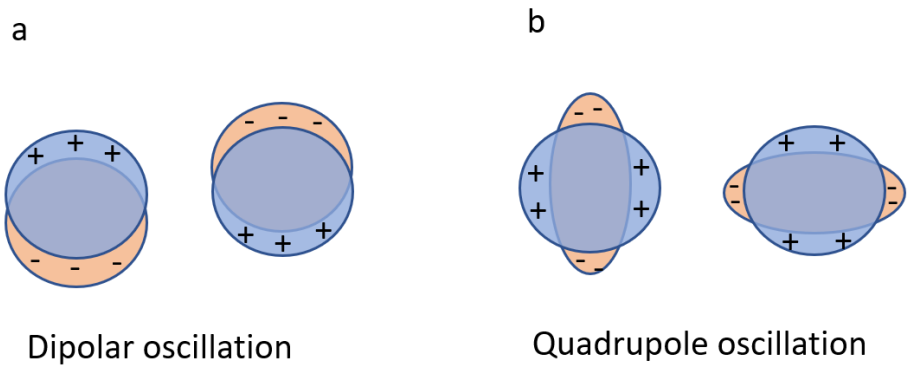

Figure 2.7. LSPR dipole and quadrupole oscillation modes of metallic nanosphere. The orange shows the electron could oscillating around ions (bule) of the metal. Figure reproduced with permission [56]

Dipolar plasmon modes, also known as bright modes, can couple to the far-field, so these modes can be excited by an optical source. As explained later, by hybridization of plasmon modes, dipolar modes can couple with higher-order plasmon modes (dark modes).

Multipolar plasmon modes, often known as dark modes because of their lack of a dipolar coupling to far-field radiation, tend to have higher energies than dipolar modes because they rely on more complicated charge rearrangements at small spatial scales. Multipolar plasmon modes, if they can be excited, can be used for a lot of applications in sensing and chemical reaction. Ways to excite multipolar plasmon modes are by retardation effects[57], using charge excitation[58], and breaking the spatial symmetry of the plasmonic structure [10], [40], [59]. Through symmetry breaking, multipolar modes can couple with dipolar modes through hybridization effect, as explained below. As a result, multipolar modes can acquire some dipolar

character that can couple to the far-field and be excited by incoming radiation [40], [59]. Chapter 6 focuses on hot carrier generation and tunneling that is generated as a result of nonradiative decay of these high-energy plasmon modes in metal-insulator-metal (MIM) tunnel junctions.

When plasmon modes couple together (via the Coulomb interaction from their charge displacements), two modes of higher energy (antibonding) plasmons and lower energy plasmons (bonding) are formed. This process is known as hybridization of plasmon modes. This is analogous to coupling of mechanical oscillators or hybridization of atomic orbitals. These plasmon modes can be seen in the spectral plot of absorption as a function of photon energy. [9], [59], [60]

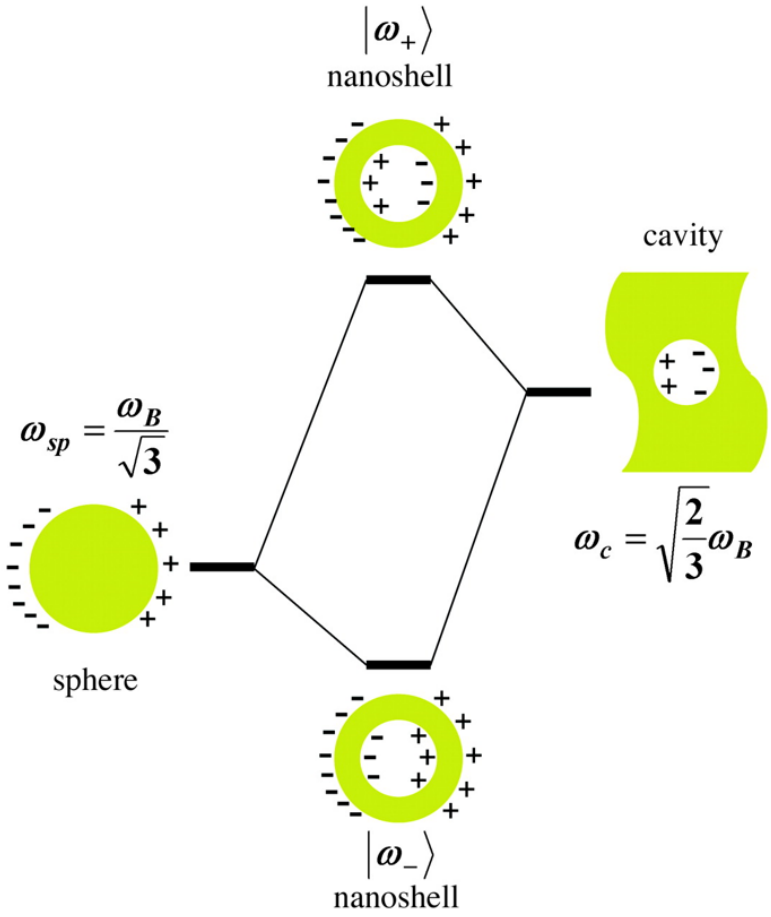

Figure 2.8. Hybrization of plasmon modes that results in a high energy and a low energy plasmon modes. Figure used with permission[9]

2.3.4. Plasmon decay

Plasmons can decay radiatively based on the Larmor formula[61], and mostly nonradiatively through the excitation of incoherent electron-hole pairs at a rate that is directly proportional to the imaginary part of the dielectric function of the metal[60]. On the scale of femtoseconds, “hot” electrons interact with each other, and on the scale of tens of picoseconds with electron-phonon interactions this energy is transferred to the lattice[35], [62]. This heat can be measured in

nanostructures, for example by measuring the conductance decrease of the system[63].

The ratio of two decay mechanisms is determined by the radiance of the plasmon modes, which can be suppressed for structures supporting subradiant (dark) plasmon modes.

In radiative decay, plasmons can decay emitting a photon through Larmor formula [61]. Depending on the phase of plasmon modes, we can have subradiant or supperradiant emissions. Plasmon Fano resonances are caused by radiative coupling and interference of these emission processes.[64], [65]

In nonradiative decay, a plasmon quantum decays and creates one electron-hole pair through Landau damping [66]. Through Landau damping, the plasmon-induced electric field can induce transitions of electrons from occupied to unoccupied states and create an electron-hole pair and it contributes to the imaginary part of the dielectric permittivity of the metal [35]. The energy and momentum distribution of these carriers depends on plasmon energy, the size of the nanostructure, the symmetry of the plasmon modes, and the electronic structure and density of state (DOS) of the material. [35], [62] Nonradiative decay of plasmon mode and generation of hot carriers is illustrated in Fig. 2.9 below. Fig. 2.9a shows the excitation of localized surface plasmons and how the nanoparticle absorbs light in an area larger than its physical size. Landau damping happens in the time scale of 1-100 fs shown in Fig. 2.9b[35]. When the hot electrons have energies smaller than the work function of the metal, they do not escape the metal, and instead they can

form a nonequilibrium Fermi-Dirac-like distribution with high effective temperature T_{eff} in a time on the order of 0.1-1 ps, based on time resolved measurements[67]; Fig. 2.9c. Energies of these hot carriers and T_{eff} depend on carrier lifetime and be calculated by Fermi golden rule. [62] If we do not utilize hot carriers distribution generated in Fig. 2.9c, they further scatter with phonons in times scale of 100 ps to 10 ns and they produce heat; Fig. 2.9d. The localized heating by plasmon decay has been measured and imaged by EELS, photoluminescence, and photothermal imaging [68]. Chapter 4 in this thesis use nonradiative plasmon decays that heat up the lattice and produce a PTE signal. Chapters 6 and 7 utilize hot carrier generation through tunneling in a MIM structure, before these carriers lose their energy to the lattice the lattice; Fig. 2.9c.

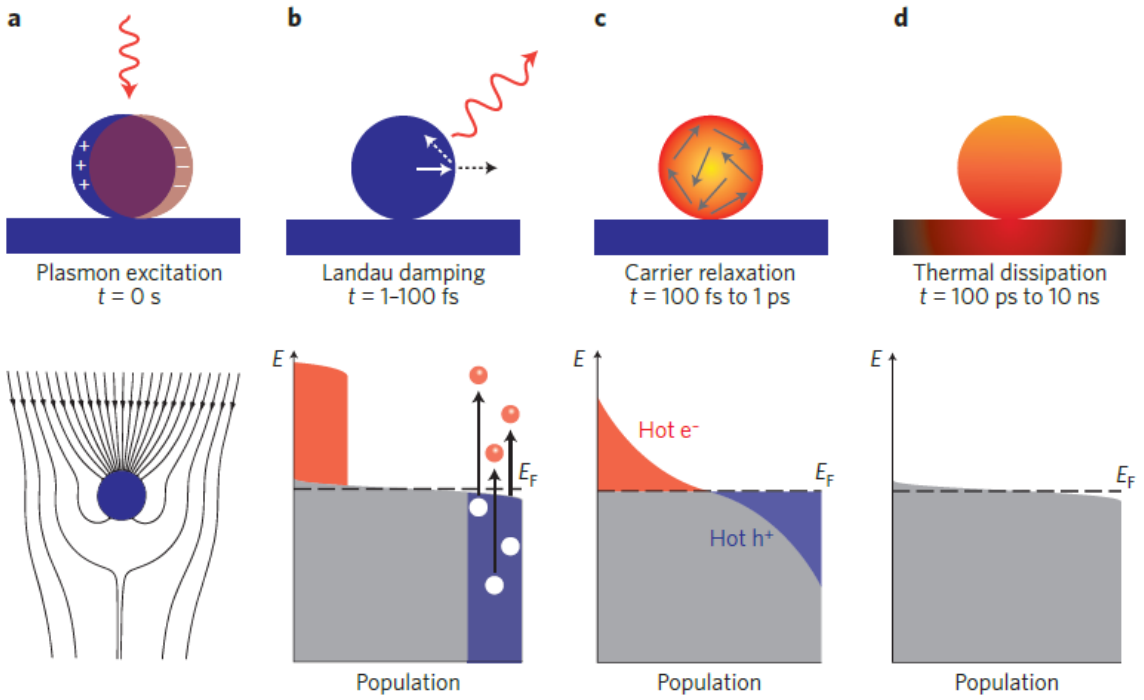

Figure 2.9. a) LSPR redirects the flow of light towards and into the nanoparticle. b) hot carriers are generated through Landau damping. C) the hot carriers scatter with each other and get to a nonquilibtium state with an effective temperature where T_{eff} is different from $T_{lattice}$. d) hot carriers scatter with the phonons and heat up the temperature of the lattice where $T_{eff}=T_{lattice}$. Figure used with permission [35]

2.4. Electron tunneling in MIM structures

Hot carriers produced by plasmon decay, because of their high energy relative to the Fermi level, can tunnel readily across insulating or vacuum barriers. In an open-circuit configuration, this hot carrier tunneling can lead to the generation of readily detected photovoltages, large compared to PTE response of the metal [22], [23]. Nanogap junctions provide a natural means of examining optically driven hot carrier tunneling. Nanogap formation in metallic nanowire can be formed by

electromigration [13, 10, 23, 24] or self-aligned [10,73] methods. Chapter 6 focuses on hot carrier tunneling through a metallic nanogap formed by electromigration. In what follows the electron tunneling in MIM structures is introduced.

2.4.1. Internal photoemission, external photoemission, and electron tunneling

Since 1970, the MIM structures have been used in different integrated designs [74]. In a metal-insulator-metal structure (MIM structure, similar to metal-dielectric-metal or MDM structure. A subcategory of MIM structures is metal-oxide-metal or MOM), when an incoming photon has enough energy to release an electron form the metal to the vacuum level (photon energy > work function of the metal), it's called external photoemission. This photoemitted electron can later be harvest by another metallic electrode [75]. If the energy of the incoming photon is smaller than the work function of the metal but larger than the insulator potential barrier, the excited electron can emit over the insulator barrier to an unoccupied state in the other electrode. When the insulator is thick that the tunneling probability is negligible, the dominant photocurrent mechanism in MIM structure is through internal photoemission. Direct wavelength determination of a monochromatic light in a power independent open circuit voltage measurement has been done using internal photoemission [76]. In a MIM structure with thin insulator layer, for an electron excited to the energy levels smaller than the insulator potential barrier, electrons can tunnel though the barrier. Electrons with energies closer to but smaller than the barrier height contribute significantly with to the electron

tunneling because the effective barrier height and thickness are smaller. For measuring the asymmetry of the insulator barrier, methods like dielectric breakdown [69] or detecting a change of slope in the logarithmic current-voltage plot in Fowler-Nordheim tunneling [70] can be used. If the photons are applied to both metallic electrodes and the photoemitted electron generation on both metallic electrodes are the same, then the probability of tunneling from metal 1 electrode to metal 2 electrode is the same as tunneling in the other direction. If we used applied bias as shown in Fig. 2.10d the effective potential barrier for photo-generated electrons on the metal 1gets thinner, so the probability of electron tunneling from metal 1 to metal 2 dominates. Photodetectors made with applied bias has another noise component (1/f noise)[71]. One way to avoid applying external voltage and still have a preferred tunneling direction when both electrodes are illuminated is using dissimilar metallic electrodes with different plasmonic properties. This is the focus of Chapter 6. In what follows, a tunneling current calculation in a general case of dissimilar MIM structure with arbitrary barrier shape is shown. In MIM designs there is also another form of photocurrent mechanism that is based on perturbation in the tunneling barrier cause by illumination. This depends strongly on the interface properties and is challenging to reproduce[72]. This process that is called photo-assisted tunneling is not the focus of this thesis.

In a MIM structure with dissimilar metal electrodes, at thermal equilibrium, the Fermi levels of two metals line up and the net tunneling current is zero. In Fig. 2.12 the black dotted plots correspond to thermal equilibrium energy plots.

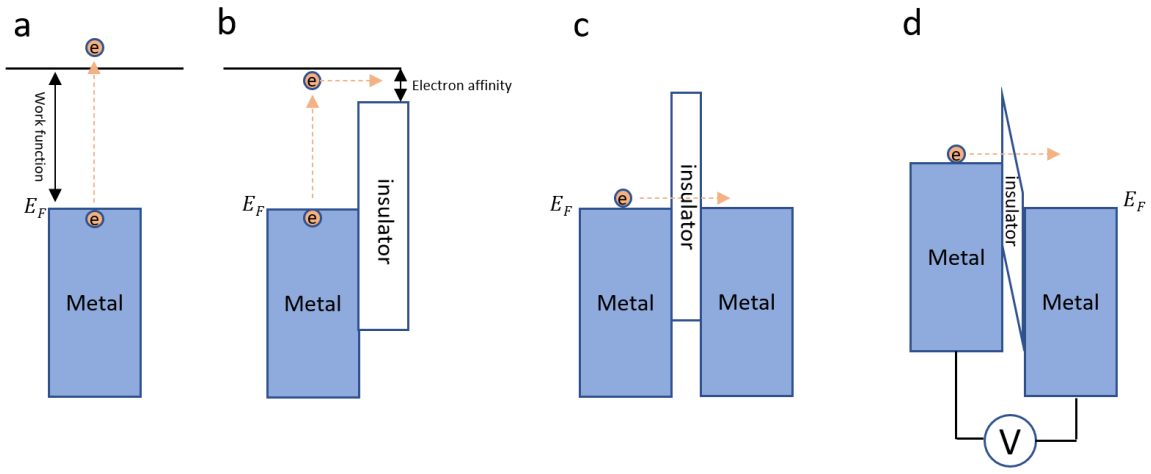

Figure 2.10. Different electron emission in MIM structures with similar metallic electrodes. a) external photoemission when E>W. b)internal photoemission when U<E<W. c,d)electron tunneling through insulator when E<U. c)symmetrical MIM structure with no bias applied. d) symmetrical MIM structure with V applied. The effective barrier thickness decreases in d due to applied voltage.

2.4.2. Electron tunneling current dissimilar MIM structures

In the fully quantum mechanical picture, the solution of the Schrodinger equation for a potential wall shown in Fig. 2.11 is as follows:

For z <0; $\Psi = a_1 \exp(ik_1 x) + a_2 exp(-ik_1 x)$ which is the sum of incident and the reflected waves. For 0<z<L; $\Psi = b_1 \exp(k_2 x) + b_2 exp(-k_2 x)$, and for z>L; $\Psi = c_1 \exp(ik_1 x)$ which is the transmitted wave. In these wave equations $k_1 = \frac{\sqrt{2mE}}{\hbar}$, $k_2 = \frac{\sqrt{2m(U-E)}}{\hbar}$, and $\hbar$ is the Planck's constant. The transparency coefficient is defined as the ratio of the probability flux density of the transmitted particles to the

probability flux density of the incident particle and for this system can be calculated as: [73]

Equation 2.13. Transparency coefficient in quantum physics picture

$$D = (cosh^2(k_2L) + \frac{1}{4}(\frac{k_2}{k_1} - \frac{k_1}{k_2})^2 \times sinh^2(k_2L))^{-1}$$

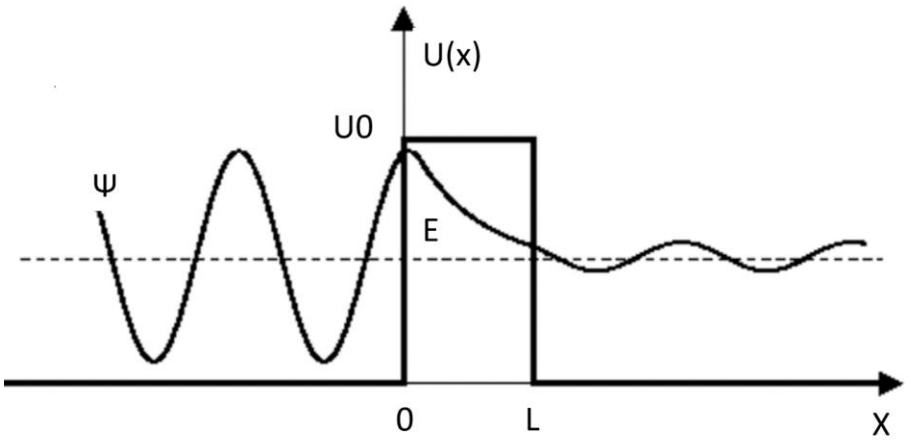

Figure 2.11. rectangular potential barrier and wave fucntion of particle Ψ

In a semiclassical picture, first applied by Wenzel, Kramers, and Brilliouin, known as WKB, in which the de Broglie wavelength of the particle (electron here) is smaller than length of the barrier (L)[74], the transparency coefficient can be calculated as [14]

Equation 2.14. Transparency equation in semiclassical picture

$$D \propto \exp\left(-\frac{2}{\hbar}\int_0^L \sqrt{2m(U(x)-E)}dx\right)$$

In both the fully quantum mechanical picture and the semiclassical picture, the D decreases exponentially with increasing barrier width.

Using the semiclassical picture mentioned above and the Sommerfeld model for electrons in a metal, the number of electrons tunneling from electrode 1 to electrode 2 and vice versa with an applied bias V across the MIM structure can be calculated. Using Simmons model, the net tunneling current can be calculated as: [75], [76]:

Equation 2.15. Tunneling current in semiclassical model

$$J = \int_0^{E_\infty} D(E_x)\xi(E_x, eV)dE_x$$

In which

Equation 2.16. This term is proportioanl to the net electron flow (N_1-N_2)

$$\xi(E_x, eV) = \xi_1 - \xi_2 = \frac{me}{2\pi^2\hbar^3}\int_0^\infty [f_1(E) - f_2(E+eV)]dE$$

By substituting $D(E_x)$ and $\xi(E_x, eV)$ tunneling current can be calculated by:

Equation 2.17. Tuennling current in semiclassical model

$$J = \frac{\alpha}{L^2}\{\varphi \exp(-AL\sqrt{\varphi}) - (\varphi + eV)\exp(-AL\sqrt{\varphi + eV})\}$$

In which: $\varphi = \frac{1}{L}\int_0^L U(x)dx$ is the averaged of the arbitrary barrier function. $A = 2\beta\sqrt{\frac{2m}{\hbar^2}}$, $\alpha = \frac{e}{4\pi^2\beta^2\hbar}$, and β is dimensionless factor in which for an arbitrary function *f(x)*:

Equation 2.18. β dimentionless factor calculation

$$\int_0^L \sqrt{f(x)}dx = \beta\sqrt{\frac{1}{L}\int_0^L f(x)dx} \times L$$

Tunneling current calculated above based on the Simmons model has neglected any thermal contribution to the current flow (T~0). It's been found that the tunneling current itself is insensitive to the temperature and the Fermi level. [77] The tunneling current presented above can be simplified for different applied voltage region. [75], [76]

When potential barrier is larger than *eV*:

Equation 2.19. Tunneling current in semiclassical model and when $eV < \varphi$

$$J = \frac{\gamma\sqrt{\varphi}V}{L}\exp(-AL\sqrt{\varphi})$$

Where $\gamma = \frac{e\sqrt{2m}}{4\beta\pi^2\hbar^2}$

The equation above shows that at low voltage region, a MIM junction behaves as an ohmic structure. In this region the forward bias and reverse bias behave similarly. [78] This is the region that it is presented in Chapter 6. The hot carrier generated in one side of the dissimilar MIM junction is ~1.5 V which is smaller than the work functions the metallic electrodes (~5 eVs). Note that in the formulation presented here, the applied bias causes the tunneling current to flow, but in results discussed in Chapter 6, tunneling hot carriers force a voltage across the junction to counteract hot carrier tunneling in an open circuit condition. In this ohmic region where open circuit voltage and tunneling current are changing linearly we can use the same formulation for calculating the hot carrier tunneling based on open circuit we measured and the resistance of our MIM structure. Other hot carrier tunneling models also are consistent with the ohmic behavior in these MIM nanogaps [22], [78].

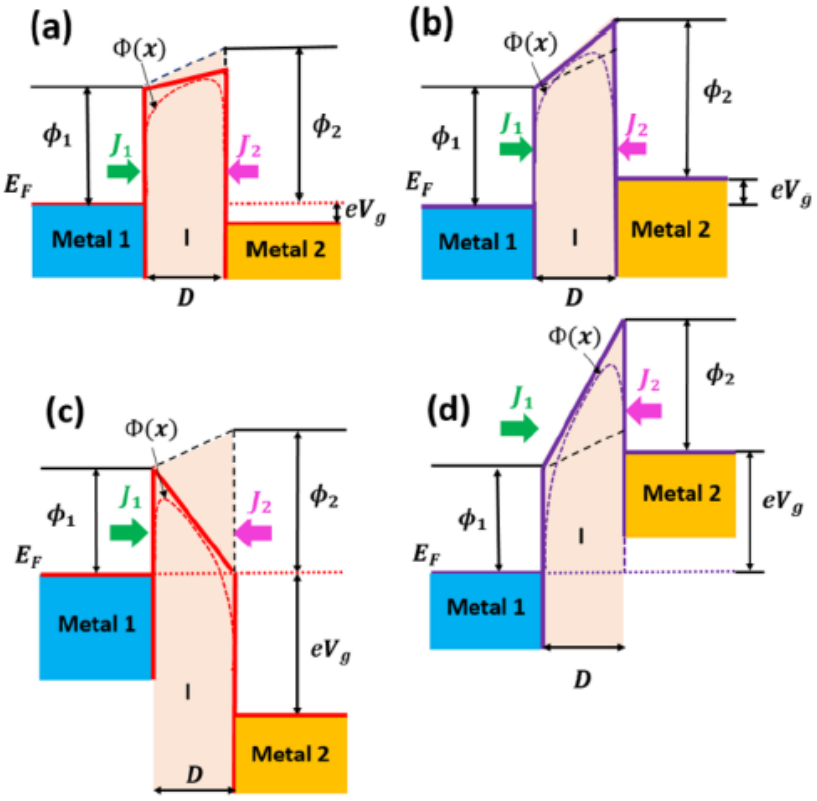

Figure 2.12. Electron tunnling in dissimilar MIM strucutres with different biases applied [88]. a and c show reverse bias with low and high applied bias respectively. b and d show the forward bias with low and high applied bias respectively. a and b behave similarly as in this region the junction is ohmic. Figure used with permission. [78]

In Simmons theory presented above the image charge potential effect has been considered but the electron space charge potential and the electron exchange-correlation potential inside the insulator thin films are ignored. So, the Simmons model fails at higher applied voltages. For high applied bias region, a better model has been developed. [78]

2.4.3. Plasmons and hot carrier tunneling in MIM tunnel junctions

Plasmons have been utilized in MIM stacked also known as heterosystems for photodetection applications [71]. In these structures, plasmons can contribute to the electron tunneling in 2 ways: hot carrier generation in the nanoparticles in the surface of the top metal by exciting LSPRs in nanoparticles, or by exciting SPPs at the interface of the metal insulator [79], [80]. In heterosystems, the optical excitation is applied to the top surface and electrical signal caused by electron tunneling is measured. The hetero design of these structures helps with the directionality of the hot carrier tunneling because the light is incident on the top surface. And the signal can further be increased by adding nanoparticles or a grating on the top electrode [81]. These hetero structures are usually large in size that can be limiting their application in compacted sensing circuits. Planar MIM junctions, on the other hand, are easier to fabricate and they do not consume a lot of space. In our planar MIM structures presented in Chapter 6, we form gaps in metallic nanowires by electromigration[82]. In this structure we benefit from exciting and coupling the multipolar plasmon modes with dipolar plasmon modes through breaking the symmetry in nanometer size gap [10], [22]. In these structures because the gap size (~1 nm) is far smaller than the incoming optical excitation spot size (~2 μm), the optical source hits both metallic electrodes at the same. This makes the polarity of the signal not stable in same metal MIM tunnel junctions [22]. MIM structures presented in Chapter 6 are made with dissimilar metal electrodes: gold and Pt. Au is plasmonically active vs the Pt which is not. Even though the laser hits both sides of the junction simultaneously, the hot carriers generated from plasmon decay are

generated on Au side and so they tunnel to the Pt electrode and so we can control the directionality of hot carrier tunneling in planar tunnel junction. This directionality is also insensitive to tiny geometry changes in nanometer sized tunnel junction, which was the main reason the polarity changed a lot in previous studies [22].

High energy plasmon modes in these metallic tunnel junctions can be either excited either by optical source or by applied bias through inelastic electron tunneling. Excited optically, these high energy plasmon modes decay nonradiatively and create hot carriers that tunnel from one metallic electrode to the other, and this hot carrier tunneling can be used for photodetectors that are fast with high responsivity comparing to PTE based photodetectors [4]. These high energy plasmon modes can also be excited by applying voltage through inelastic electron scattering. These plasmon modes can decay either radiatively and produce below threshold light emission [11], [83] or nonradiatively and create high energy e-h pairs [12]. These high energy e-h pairs when recombined can cause above threshold light emission possible. Hot carrier generation through optical excitation is introduced in Chapter 6 and hot carrier generation through inelastic electron tunneling are introduced in Chapter 7. Chapter 7 mainly focuses on characterizing the plasmonic behavior of these structures.

Chapter 3

COMSOL Multiphysics simulations

3.1. Motivation:

In this thesis COMSOL simulation results for plasmon resonances, temperature increases in nanostructure, and the photothermoelectric effect have been shown in different chapters. In this Chapter different Multiphysics simulations are discussed. The particular focus is on COMSOL Multiphysics which we use in our modeling.

3.2. FEM vs FDTD

Both Finite Difference Time Domain (FDTD) and Finite Element Method (FEM) solve differential form of Maxwell's equations. The FDTD solves the equations in time domain and FDTD solve them in frequency domain. Each of these methods has its own pros and cons. In FEM, any arbitrary details in geometry can be resolved

due to flexibility in mesh elements vs in FDTD, the grids are in Cartesian directions which cannot resolve the curved shape geometries. The meshing mechanism in FEM can be very powerful for complex objects but it needs proper optimization to save calculation time[84]. FDTD algorithm can be parallelized which can make FDTD method faster than FEM.[85] Boundary Element Method (BEM) solves integral form of Maxwells equations in frequency domain (Green's functions). BEM can also be faster than FEM and FDTD but it may be only used for linear and homogeneous structures. [86]

COMSOL solves differential equations based on FEM. We use FEM to simulate our structure because of asymmetric, random shaped of our geometries (for example in nanogap structures after electromigrating the nanowire) and also because of high accuracy of the method. We specifically use COMSOL because of its unique ability to couple different physics interfaces together and solve them all at once. Also because of its strong postprocessing tools. There's room to grow for the software but among Multiphysics FEM based simulation software COMSOL is the strongest tool.

3.3. Ewfd simulations: equations and model

Electromagnetic wave, frequency domain (ewfd) interface models light and matter interactions in classical physics. In other words, it solves Maxwell's equations in frequency domain assuming a sinusoidal excitation and linear media:

Equation 3.1. Maxwells equations, frequency domain

$$\nabla \times {\mu_r}^{-1}(\nabla \times E) - k_0^2\left(\varepsilon_r - \frac{j\sigma}{\omega\varepsilon_0}\right)E = 0$$

In which μ_r, ε_r, ε_0, σ, k_0, and ω are relative permeability, relative permittivity, permittivity of vacuum, electrical conductivity, wave number in vacuum, and angular frequency on incident beam respectively. In this equation dielectric and conduction losses are considered by defining imaginary part permittivity in which:

Equation 3.2. Complex refractive index

$$\varepsilon_{complex} = \varepsilon - j\frac{\sigma}{\omega} = \varepsilon_0(\varepsilon' - j\varepsilon'')$$

This model is used to model plasmonic behavior of the structures throughout this thesis. The dissipated power in the structure can later be used as a heat source in a heat transfer model to calculate the temperature distribution across the device. Using this interface, *E* field enhancement relative to the field from incident radiation can also be calculated. *E* field enhancement gives us a lot of information about the plasmon behavior and clarifies our expectations from experiments. For example, in surface enhanced Raman spectroscopy (SERS), the emitted signal increases approximately with $|E|^4$ [10], [87]; the probability for photon absorption is proportional to the local intensity (square of the local electric field) inside the metal [35]; HC production likewise follows optical absorption. Optical transition rates are proportional to internal $|E|^2$ [35], [88]. Surface enhanced infrared absorption

(SEIRA) signal is likewise proportional to $|E|^2$ [89], [90]. Plasmon resonances make the field enhancement polarization and wavelength dependent, while the geometric "lightning rod effect" can cause the non-resonant field enhancement.[91]. Mie theory provides detailed formulization for plane wave and sphere nanoparticle interaction for homogeneous and isotropic materials.[92], [93] This theory is a semi-analytic method for solving limited cases of scattering problems; sphere nanoparticles and infinite cylinders.

The plasmonic response of nanostructures can be found via simulation by defining the material properties and geometry, and then using the electromagnetic wave, frequency domain (ewfd) interface, which solves Maxwells equations. The temperature distribution models have used the heat transfer (ht) interface. For calculating how much heat is caused by an applied optical source, a coupled model of ewfd and ht is used. For simulating PTE signal, a coupled model of heat transfer(ht) and electric current (ec) physics interfaces is used.

For optical simulations, the maximum mesh size for each domain is the effective wavelength in that domain divided by 5 ($\mathrm{l}/n/5$, where n is the index of refraction). Maximum mesh size for the gold film is smaller than the skin depth of the gold film at the applied wavelength. For the thermal and electrical simulation, a coarser mesh is sufficient.

For optical simulations, the real and imaginary parts of the dielectric permittivity, ε, are critically important. The permittivity parameters for particular materials are extracted from the literature. [94]–[97] Permittivity determines how

incident light interacts with the material. Interband transitions in metals contribute to the damping and primarily contribute to the imaginary part of the permittivity. The imaginary part of epsilon corresponds to the optical losses in metals [92]. The nonradiative decay of plasmons is proportional to the imaginary part of the permittivity. The ohmic heat per unit volume generated locally is proportional to imaginary part of the permittivity:

Equation 3.3. Joule heating and permittivity

$$Re\left[\vec{E}.\vec{J}\right] = Re\left[\vec{E}.\frac{d\vec{P}}{dt}\right] = Re\left[\vec{E}.i\omega\vec{P}\right] = \omega Im\left[\vec{E}.(\varepsilon - 1)\vec{E}\right] = \omega|E|^2 Im[\varepsilon]$$

3.4. Heat transfer in solids simulation: equations and model

The heat transfer in solids physics interface in COMSOL solves heat balanced equations shown below [98]. In these equations the variation of internal energy in time is balanced by convection of internal energy, thermal conduction, radiation, dissipation of mechanical stress and additional volumetric heat sources. For solids this balance at steady state can be written as:

Equation 3.4. Heat transfer in solids, steady state

$$\rho C_p u.\nabla T + \nabla.q = Q + Q_{ted}$$

In which ρ, C_p, u, and T are density, heat capacity at constant stress, velocity vector, and absolute temperature respectively. $q = -k\nabla T$ is the sum of heat fluxes by conduction (k is the thermal conductivity). Q_{ted} is the thermoelastic damping and accounts for thermoelastic effects in solids:

Equation 3.5. Thermoelastic damping for solids

$$Q_{ted} = -\alpha T : \frac{dS}{dt}$$

S is the entropy and the $: \frac{d}{dt}$ operator is called material derivative which also accounts for spatial transformation as well as time derivative:

$$: \frac{d}{dt} = \frac{\partial}{\partial t} + u_{(x,y,z)} . \nabla_{(x,y,z)}$$

In this equation $u_{(x,y,z)} . \nabla_{(x,y,z)}$ corresponds to convection in case of fluids, or convected quantity by translational motion of a solid.

In the balanced equation shown above, Q is any additional heat source. When coupling ewfd physics interface with heat transfer in solids, the dissipated power cause by an optical source is used as external heat source (Q) to this equation. So, we can model the temperature distribution cause by plasmon oscillations in metallic nanostructures. These simulations are used in Chapter 4 in which temperature increase due to plasmon oscillation help us model the characteristic of single metal photodetectors and their PTE signal.

3.5. Electrical circuit: equation and model

This interface solves a current conservation for the scalar electric potential V. In steady state these equations are as follows:

Equation 3.6. Electric field and electric signal equations

$$E = -\nabla V$$

$$J = \sigma E + J_e$$

$$\nabla . J = 0$$

In these equations, J_e is externally generated current density. This term is needed for PTE simulation (see below). This interface can be coupled to heat transfer in solids through electromagnetic heating node in which the Q in balanced heat transfer equation is the ohmic losses:

Equation 3.7. Ohmic losses

$$Q = \vec{E} . \vec{J}$$

For simulating the PTE, the thermoelectric node needs to be added so that $J_e = -\sigma S \nabla T$ is added to the current density and heat flux term $q = PJ$,in which $P = ST$, is added to the heat transfer in solid equation.

In Chapter 4 and 5 for simulating PTE signal in single metal photodetectors and in single crystalline gold nanowires, all modules presented here are coupled as

described above. For simulating the plasmonic characteristic of nanogap in Chapter 7, the ewfd module is used with very dense meshing in the nanogap. Proper boundary conditions as well as material properties in thin films need to be applied in these simulations.

Chapter 4

Plasmonic based single metal photodetectors

This chapter is based in part on the publication "Single Metal Photodetector Using Plasmonically- Active Asymmetric Gold Nanostructures," **M. Abbasi**, C. I. Evans, L. Chen, and D. Natelson, ACS Nano, 14, 17535-17542 (2020).

4.1. Motivation and Introduction

PTE based photodetectors do not require a cooling unit or an external bias, which makes them good candidates in compacted designs. This study focuses on understanding the PTE response of metallic gold nanostructures, and the structural engineering of gold films to get larger electrical signals for photodetection applications. For photodetection considerations, detailed knowledge of charge carrier and energy flow when an optical heat source is applied to metal at the nanoscale is necessary. In other words, understanding the factors that affect the Seebeck coefficient in metallic nanostructures is necessary. In this Chapter, by engineering the geometry of single metal nanowire, we are able to make asymmetric

structures with different plasmonic behavior on each side of the device, as well as an asymmetric Seebeck map across the device. This combination helps us to produce a net voltage when the device is flood illuminated. These photodetectors are spectrally sensitive and polarization dependent due to plasmon activation. We employ gold as the best option, thanks to its chemical resistance, ease of fabrication, and strong plasmonic resonance in the near infrared for our device designs.

Plasmonic-based photodetectors are receiving increased attention because simple structural changes can make the photodetectors spectrally sensitive. In this study, asymmetric gold nanostructures are used as simple structures for photodetection via the photothermoelectric response. These single metal photodetectors use localized optical absorption from plasmon resonances of gold nanowires at desired wavelengths to generate temperature gradients. Combined with a geometry-dependent Seebeck coefficient, the result is a net electrical signal when the whole geometry is illuminated, with spectral sensitivity and polarization dependence from the plasmon resonances. I show experimental results and simulations of single-wavelength photodetectors at two wavelengths in the near IR range: 785 and 1060 nm. Based on simulation results and a model for the geometry-dependent Seebeck response, I demonstrate a photodetector structure that generates polarization-sensitive responses of opposite signs for the two wavelengths. The experimental photothermoelectric results are combined with simulations to infer the geometry dependence of the Seebeck response. These results can be used to increase the responsivity of these photodetectors further.

The geometry of metallic nanostructures can be tuned so that localized surface plasmons (LSPs) are resonant at particular incident wavelengths and polarizations [99], [100]. This resonant coupling to light leads to enhanced scattering and absorption. [101] Plasmon-induced heating is directly proportional to the imaginary part of the dielectric function of the metal [101]. Optically driven heating can be used in conjunction with thermoelectric response to enable photodetection via the photothermoelectric (PTE) effect [5]. Charge carriers in a conductor heated under a temperature gradient tend to diffuse from high to low temperatures. In an open-circuit configuration, an internal electric field builds up to offset this diffusion, producing an open circuit voltage (the Seebeck effect), such that, locally, $\nabla V = -S \times \nabla T$, in which S is the Seebeck coefficient and ∇T is the temperature gradient. A traditional thermocouple can be made by having two conductors with different S in contact with each other. When that junction is heated relative to the ends of the materials, the open circuit voltage is proportional to the difference in S as well as the temperature gradient. The electronic contribution to the Seebeck coefficient S is often modeled by Mott's formula [7] (see Eqn. 2.9). This equation shows that Seebeck coefficient of metals at room T depends on σ; the energy-dependent electrical conductivity, k_B; the Boltzmann constant, T; temperature, e; the electron charge, E; the electron energy, and E_F; the Fermi energy of the conductor. The energy-dependent electrical conductivity is related to the scattering processes in the conductor [63]. When the conductor dimensions are comparable to the mean free path of carriers, the electrical conductivity and thus S can be manipulated by engineering the geometry. As a result, it is possible to make

thermocouples with a single conductor [6], [17], [18], [20], [102]. Other factors that can tune the Seebeck coefficient include surface chemistry [19], impurity concentration [103], strain,[21], [104] and modifications to band structure. Photodetectors based on PTE do not require external bias, so their intrinsic noise source is mainly Johnson–Nyquist thermal noise [5]. PTE-based photodetectors have been put forward based on bolometric metal structures, [102], [105] plasmonic metal structures coupled to semiconductor materials,[106], [107] and devices incorporating 2D materials.[3], [108]–[110] In this study, we demonstrate integrated photodetection structures combining the geometric spectral tunability and polarization sensitivity of LSPs and the structural engineering of Seebeck response. We show experimental results and matching finite-element simulations for gold plasmon-resonant single-wavelength PTE detectors designed for 785 and 1064 nm incident wavelength. With this understanding and a model for geometric dependence of Seebeck response, we demonstrate a PTE-based single metal structure that generates polarization-sensitive photovoltages of opposite signs for the two wavelengths. The experimental response confirms the consistency of the assumed geometry dependence of the Seebeck coefficient.

4.2. Experimental setup

4.2.1. PTE maps or more generally photovoltage (PV) maps measurements

Fig. 1a shows the experimental approach for measuring the steady-state PTE response, using a scanning laser as the incident light source, with spot size tuned via

the objective/sample distance. The open circuit voltage is measured with a lock-in amplifier with its frequency locked to the frequency of the chopper that modulates the laser intensity incident on the sample, as is shown in Fig. 4.1. The open circuit voltage is measured with the lock-in amplifier after being amplified with the voltage preamplifier. The integrated open circuit voltage at a fixed position of heat source is calculated as in Eqn. 4.1, that is the integral of the open circuit voltage gradient at all points along the device. The modulation period of the chopper is much longer that the thermal time scales of the structures,[49] so that all the data are recorded in the steady state. To be effective for unfocused photodetection applications, the net PTE response for a structure under flood (unfocused) illumination must be nonzero. In a single-metal structure symmetric about its midpoint (such as bow-tie constriction connected to two pads), the temperature profile when uniformly illuminated and the Seebeck distribution are both spatially symmetric. This leads to a local PTE map acquired under focused illumination that is antisymmetric. This implies that when the whole geometry is uniformly illuminated, the net open circuit voltage would be zero and there would be no photodetection. An asymmetric geometry, conversely, in general has an asymmetric temperature profile when uniformly illuminated as well as an asymmetric Seebeck distribution, so when the whole geometry is illuminated, the open-circuit voltage should be a nonzero value. In this work, we create asymmetric structures to have a plasmonic resonance and hence enhanced absorption and elevated temperatures on one side, combined with a spatially asymmetric Seebeck distribution.

Equation 4.1. The open circuit voltage measured at each point in a PTE map

$$V = -\int_0^l S(x,T)\nabla T(x)$$

Here $S(x,T)$ is the Seebeck coefficient of a device that is a function of position and temperature. $\nabla T(x)$ is the gradient of the temperature distribution along the device, and l is the length of the device along the two pads from which the open circuit is measured.

This scannable method can be used to probe internal properties of the single metal nanowires by characterizing the Seebeck map when the geometry is constant across the device. This is the focus of chapter 5.

Detail of the opto-electrical measurement setup is as follows. The CW laser is focused on the structure using a Zeiss Epiplan-Neofluar 50× objective with an NA of 0.55. During scanning measurements, two Thorlabs DRV001 stepper motors control the 2D movement of the sample stage in the plane perpendicular to laser direction and the integrated steady-state open circuit photovoltage signal of the entire device is measured at each spot in the stationary state to obtain the PTE maps. In the PTE maps presented here, the pixel size is 0.5 μm × 0.5 μm. The smallest laser spot diameters in the present setup for the 1060 and 785 nm CW lasers are 3.5 and 2.7 μm, respectively. The spatial resolution is limited by a combination of optics (the laser spot size, the scanning pixel size) and the thermal properties that set the laser induced temperature profiles (thermal conductivity of the metal and substrate, thermal boundary resistance between the metal and substrate, and environment

temperature). All the measurements are done at room temperature and at ambient conditions.

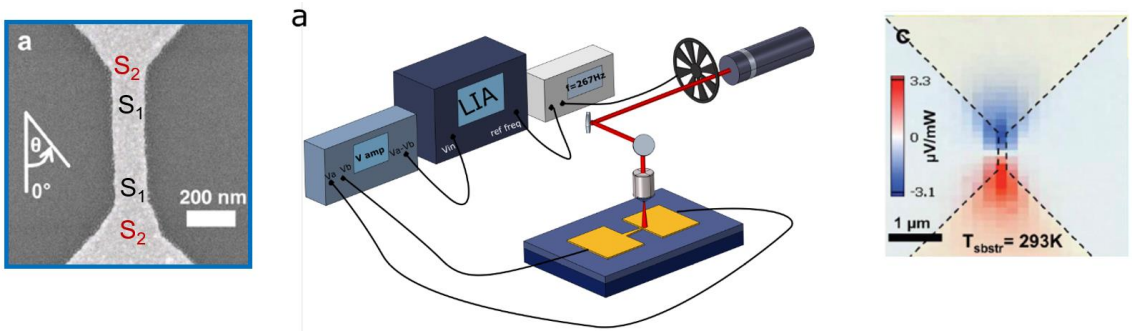

Figure 4.1. PTE maps or more generally PV (photovoltage) maps measurement. a) SEM image of a symmetric bowtie structure with antisymmetric Seebeck coefficient map. b) Experimental setup scheme. A CW laser is used as a scannable heat source. A chopper modulates the laser, and the open circuit voltage is measured using a lock-in-amplifier with its frequency locked to the chopper frequency. c) False color SEM image ovrelaied with PTE map. a and c are used with permission [21]

4.2.2. Fabrication of the devices

The gold structures are made on a thermally oxidized silicon substrate with an oxide thickness of 2 μm. Gold has a strong plasmonic resonance in the near-infrared (IR) and exhibits high chemical stability. Large gold pads are patterned on the substrate using photolithography and e-beam evaporation of 60 nm Au with a 5 nm Ti adhesion layer. The plasmonic structures with tapered gold nanowires are patterned by electron beam lithography using an Elionix e-beam writer followed by e-beam evaporation of 18 nm Au with 1 nm Ti adhesion layer and liftoff by acetone.

A K&S 4526 wire bonder is used to electrically connect the large pads on the geometry to chip carrier using gold wires with 100 μm in diameter.

4.2.3. Knife edge measurement

The focus of the laser and hence the spot size on the device is controlled by moving the sample stage toward the objective using a Thorlabs MTS50 1D stage motor. The size of the expanded beam is measured using knife-edge measurement.[111] The focused laser diameter is measured using the laser's white light image on the CCD. The edge of the laser beam is positioned on the edge of a gold film. Then, the sample stage moves in one direction using a Thorlabs BCS102 motor controller and Thorlabs DRV001 stepper motor with step sizes of 0.1 microns until the laser is passed from the edge. Laser diameter is the same size as the stage movement. The expanded laser diameter is measured by the knife-edge measurement. The knife-edge here is a razor blade. The razor blade is moved farther and closer to the objective focus point by a Thorlabs MTS50 1D stage motor and a Thorlabs KDC101 motor controller. A Thorlabs MTS25 1D stage motor is used to move the razor blade from one side to the other to block the laser. A PM100D Thorlabs power meter is used to measure the fraction of the laser power that is not blocked with the razor. The results of the knife-edge measurements are shown in Fig. 4.2. Based on these results, the laser diameter change vs. change of distance from the objective is calculated by a linear fit through all the experimental results. The laser diameter at each distance from the objective focus point can be calculated by having the focused laser size and the knife-edge measurement results.

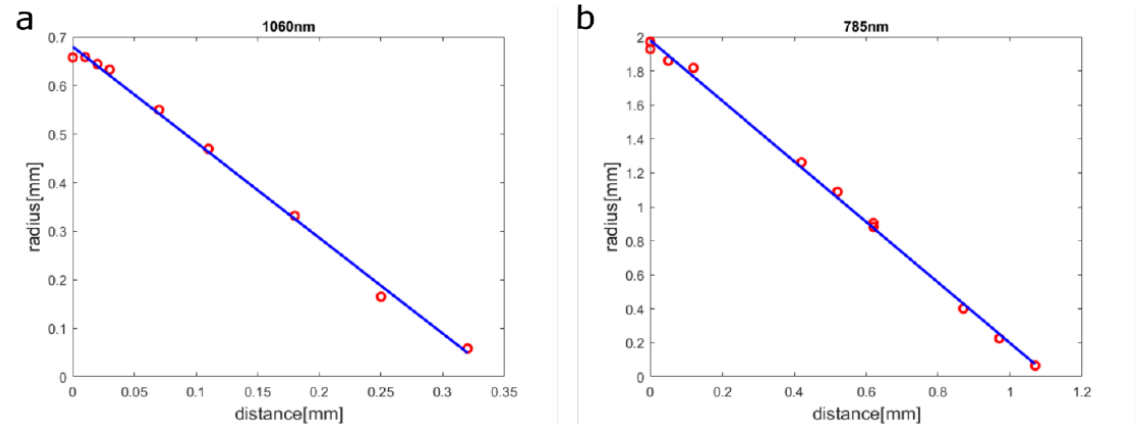

Figure 4.2. Knife-edge measurement results for two CW lasers used in the experiment. a) knife-edge measurement of 1060 nm CW laser. b) knife-edge measurement of 785 nm CW laser. The blue lines show the linear fit to the experimental data

4.3. Asymmetric plasmon based single metal photodetectors

The LSP mode employed here is the dipolar transverse mode of a gold nanowire, excited when incident polarization is aligned transverse to the wire's long axis. For a wire with a fixed thickness, there will be wavelength-dependent width that resonantly couples to the optical source. We find the resonant width for a given incident wavelength by calculating the width dependence of the absorption of a nanowire using the finite element method (FEM) package COMSOL Multiphysics. In these simulations, a plane wave with a transverse polarization is applied to a cross-section of a nanowire at a certain width and thickness and the total integrated absorption power is calculated as a function of wire width. Absorption calculations

for two wavelengths in the near IR range are shown in Fig. 4.3. In these simulations, the thickness of silicon oxide is 2 μm, the thickness of the nanowire is fixed at 18 nm, and the width of the gold nanowire varies from 50 to 1000 nm. Absorption plots for other gold thicknesses and silicon oxide thicknesses are shown in Fig. 4.4. The peaks in the absorption plots correspond to the transverse LSP resonant width at each wavelength. Based on these simulations, we can design an optimized photodetector for each of the wavelengths. A single-wavelength photodetector device is shown in Fig. 4.3. The nanowire in the middle of the device is tapered such that the wider side is plasmonically resonant for the designated wavelength (where the peak happens in the Fig. 4.3 plot), and the narrower side's width is farther away from the plasmonic resonance. Based on Fig. 4.3, for detectors active at 1060 nm wavelength, the width of the wider side of the tapered nanowire is ~300 nm, and the narrower side's width is ~100 nm. For detectors active at 785 nm wavelength, the widths are ~170 nm and ~50 nm, respectively. By designing the wider side to be plasmonically resonant, the responsivity of the photodetectors at a single wavelength is much higher because of the enhanced absorption (via resonance and metal area) coupled with the spatial dependence of the Seebeck coefficient. Modifications to the Mott formula have been proposed that account for boundary scattering effects on the carrier mean free path.[112] Based on this, when the wire width is larger than the carrier mean free path in the unbounded metal film, the narrower the nanowire, the smaller the Seebeck coefficient will be due to boundary scattering (assuming a positive S). Thus, from where the width suddenly decreases from the fan-outs to the wider side of the nanowire, the local Seebeck coefficient

drops suddenly (S1 < S0 in Fig. 4.3). The Seebeck coefficient continuously decreases along the tapered nanowire (S2 < S1). Finally, the narrower side of the tapered wire connects to the fan-out and the Seebeck coefficient abruptly increases again (S0 > S2). The expected spatial dependence of the Seebeck coefficient of the device in Figure 4.3 is shown in Fig. 4.14, showing a model that the change in S is inversely proportional to the width of the nanowire.[112] With one side of the device being connected to the ground and based on the Seebeck map, if the heat source is localized on the wider side junction (where S0 changes to S1 in Fig. 4.3), the sign of the thermovoltage is the same as if the heat source is located in the middle of the device (where S1 gradually changes to S2). Conversely, the thermovoltage is of the opposite sign if the heat source is instead located on the narrower side junction (where S2 changes to S0). For higher responsivity for this plasmonically based photodetector, we need the sign of the Seebeck change on the tapered nanowire (and hence the sign of the PTE signal when heating is located on the nanowire) to be the same as the sign of the Seebeck change where the plasmonically resonant nanowire end joins the fan-out (and hence the sign of the PTE signal when heating is located at that location). The sign of the thermovoltage at the tapered nanowire is important for two reasons. First, the plasmonic resonances shown in Fig. 4.3 are comparatively broad, so that when one side of the nanowire has the transverse plasmon coupling resonantly with the optical source, the other widths across the tapered nanowire still contribute measurably even though they are off resonance. Second, when the laser is focused on the nanowire, the local temperature increases more than when the laser is closer to the fan-outs because the fan-outs have

improved thermal conduction and behave as a heat sink. The simulation results of the temperature profile of a 1060 nm photodetector at two polarizations and different laser positions are shown in Fig. 4.10. Other than width, other factors that change the overall absorption across the device are simulated and shown in Fig. 4.4. Thinner gold film, thicker silicon oxide substrate and removing Ti adhesion layer are some factors that we can increase the optical absorption across the device. For better yield of fabrication as well as increasing the absorption across the device, the thickness of films are 18nm with 1 nm Ti as adhesion layer and 2 microns silica thickness.

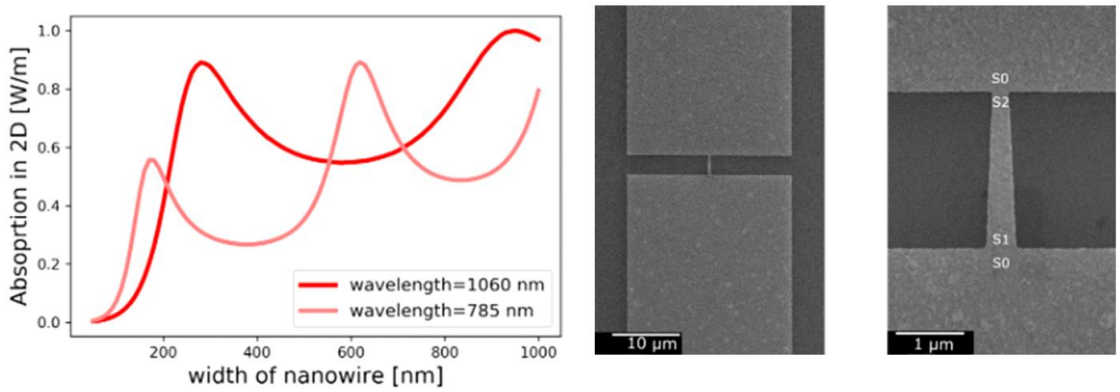

Figure 4.3. a) Simulated absorption across section of a gold nanowire for two wavelengths of 1060nm and 785nm as a function of wire width. Dipole resonance peak for 1060 nm and 785 nm for gold nanowire happens at widths

of 300nm and 180nm respectively. B) SEM images of a single metal photodetector designed for 1060nm wavelength.

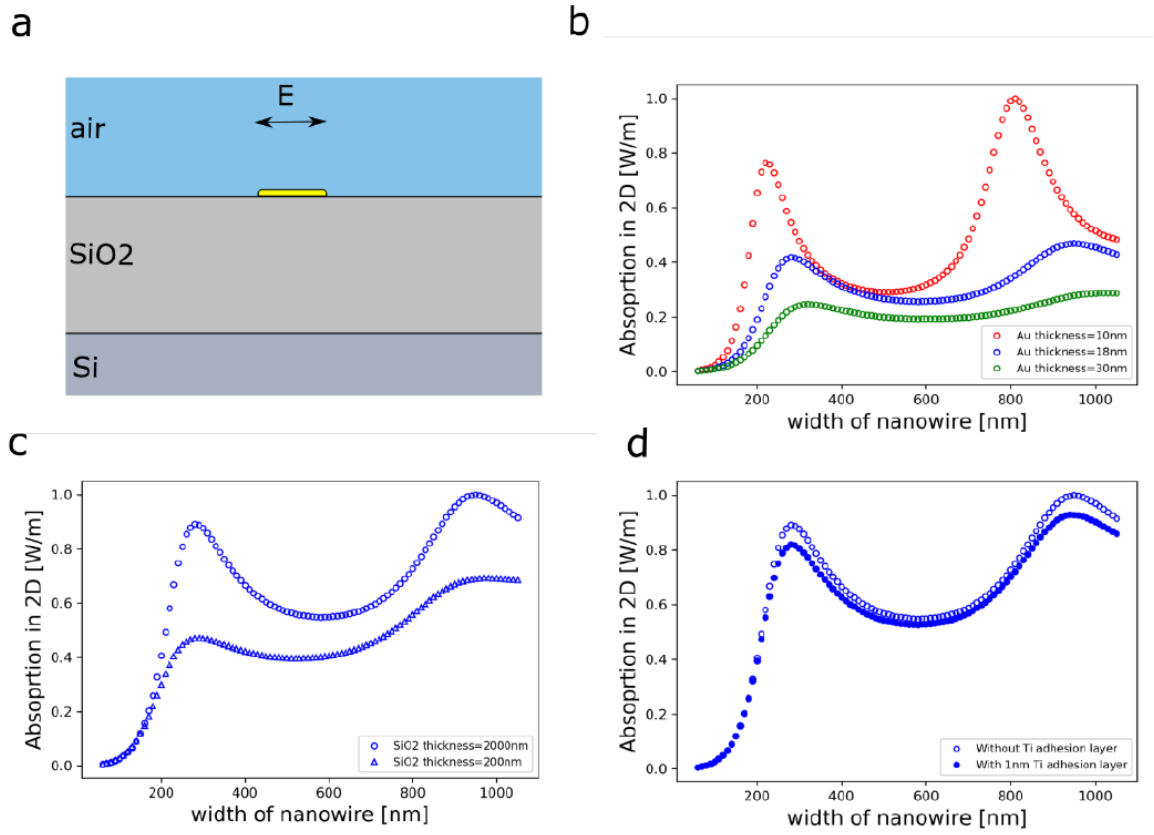

Figure 4.4. Other factors that affect the absorption. Absorption versus width of the nanowire at different thicknesses for Au, SiO_2, and with and without adhesion laser. a) Absorption plots when SiO_2 thickness is fixed at 2 μ m and Au thickness changes. b) Absorption plots when Au thickness is fixed at 18 nm and SiO_2

PTE maps for focused laser scans of two single-wavelength photodetectors designed for 1060 and 785 nm wavelengths are shown in Fig. 4.5. All of the open circuit voltage data are normalized to the incident power, helpful because of the linear optical power dependence of the PTE signals. The device that is presented in

Fig. 4.5 is designed for 1060 nm incident wavelength. The top row of Fig. 4.5 shows the PTE map of the device when the laser has longitudinal polarization, and the bottom row shows the results when the incident laser has transverse polarization. Columns in Fig. 4.5 show the PTE map with different laser spot sizes (degrees of defocus). Fig. 4.5b shows the polarization dependence of the same device under flood illumination when the laser is expanded the most (spot size 43 μm as determined by knife edge) and the laser is positioned in the middle of the device. As shown in Figure 4.5b, the response of the photodetectors is polarization dependent. Fig. 4.5c and d shows the results for a different detector device designed for 785 nm incident wavelength. These results show that when the laser is expanded to approach flood illumination, the signal from the plasmonically resonant side dominates at transverse polarization. The responsivities of these devices are 11.3 mV/W and 10.3 mV/W for the single-metal devices in Fig. 4.5a and c, respectively, using the effective area inferred from simulations in COMSOL. See section 4.6.

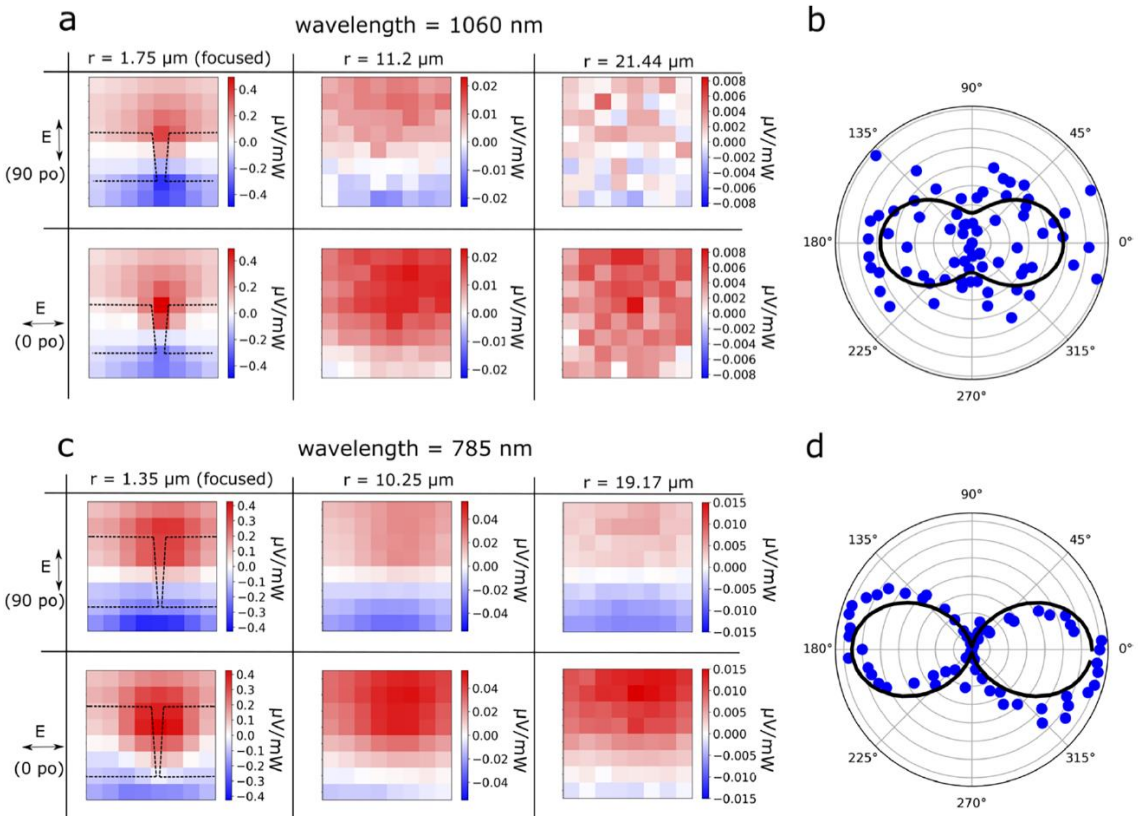

Figure 4.5. Single metal photodetector at 1060 nm and 785 nm

To show that these photodetectors behave most effectively at our desired wavelengths, we measured photodetectors presented in Fig.4.5 at another wavelength. Fig. 4.6 shows PTE responses of the PD designed at 1060nm at two wavelengths of 1060nm and 785nm. As it is shown, the PD response at desired wavelength at flood illumination is stronger as expected by our design.

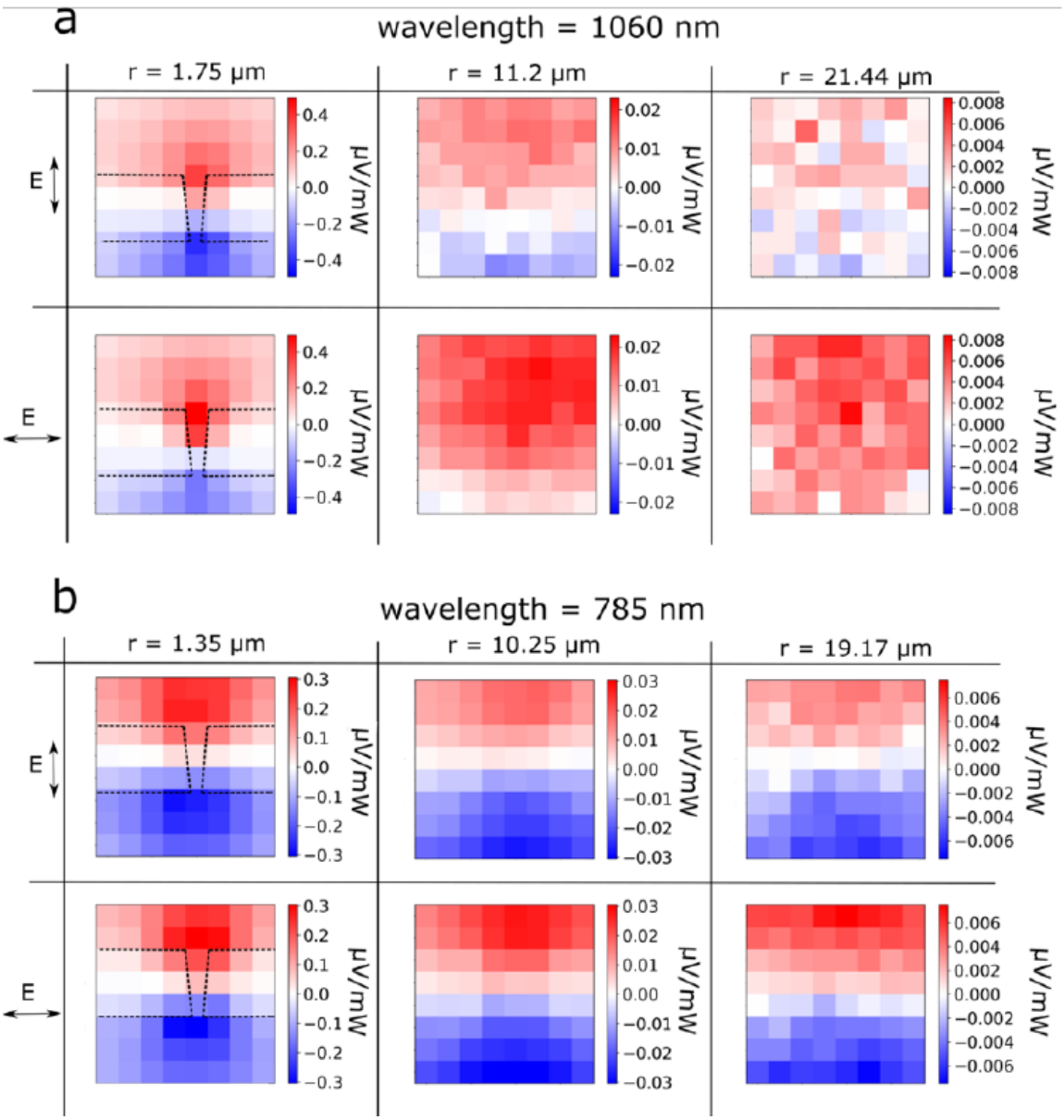

Figure 4.6. PTE map result for a device designed to detect 1060 nm efficiently at two wavelengths of 785 nm and 1060 nm. a) PTE map at differe polarization and different laser sizes when a 1060 nm CW laser is used as the heat source. When the laser is expanded, the signal is dominated by the nanowire's active polarization side at transverse polarization. b) PTE results of the same device when a 785 nm laser is used as a heat source. When the laser is expanded,

neither of the sides is dominant. This proves that each simple structured photodetector can be optimized for each wavelength.

4.4. Designing a photodetector behaving differently at two NIR wavelength of 785 nm and 1060 nm

Based on the logic and approach above, it is possible to design a single photodetector that detects and discriminates two wavelengths. Fig. 4.7 shows the structure of a photodetector such that upper half of the device is plasmonically resonant at 1060 nm and the bottom half is plasmonically resonant at 785 nm. The PTE results of this structure are shown in Fig. 4.8. Fig. 4.8a,b shows the response of this structure at 1060 nm, and Fig. 4.8c,d shows the response of this structure at 785 nm. The sign of the thermovoltage at the upper tapered nanowire is different from the sign of the signal on the bottom tapered nanowire because of the geometry and the resulting mirrored Seebeck coefficient change. As shown in Fig. 4.8, when the laser is maximally expanded with transverse polarization, the upper tapered nanowire dominates the sign of the photovoltage signal at 1060 nm, while at 785 nm, the signal is dominated by the bottom tapered nanowire. The responsivity of this photodetector at 1060 nm is 5.15 mV W , and at 785 nm the responsivity is 7.10 mV W . The reason that the responsivity of this device is smaller than the photodetectors designed solely for 785 or 1060 nm (Fig. 4.5) is that two opposite signs of the photovoltage at two tapered nanowires work against each other. This results in a net decrease of the impact of the plasmonically resonant side, compared to the single-wavelength-optimized detectors. To improve this device's responsivity

and to optimize this approach in general, we need to know quantitatively how much the Seebeck coefficient changes when metal wire widths change in these devices. See section 4.5.

As is evident in Fig. 4.8. when the laser is expanded, the positive signal is dominating the PTE map at transverse polarization, which corresponds to the resonant plasmon response at 1060 nm.

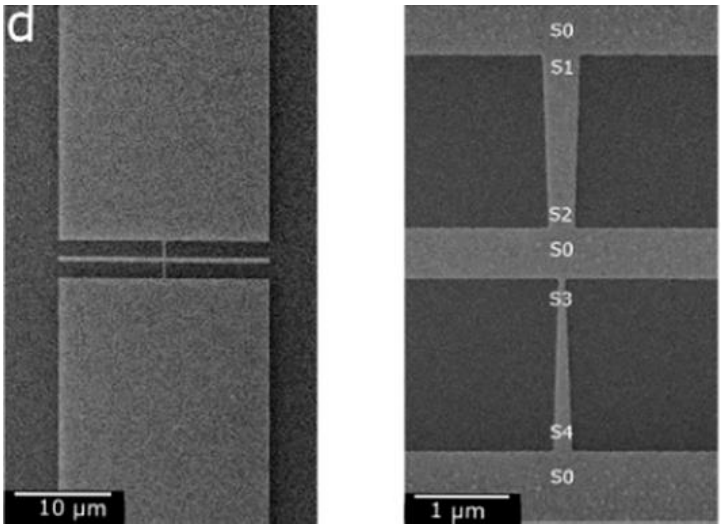

Figure 4.7. SEM iamge of a PD desinged for two wavelengths of 785nm and 1060nm

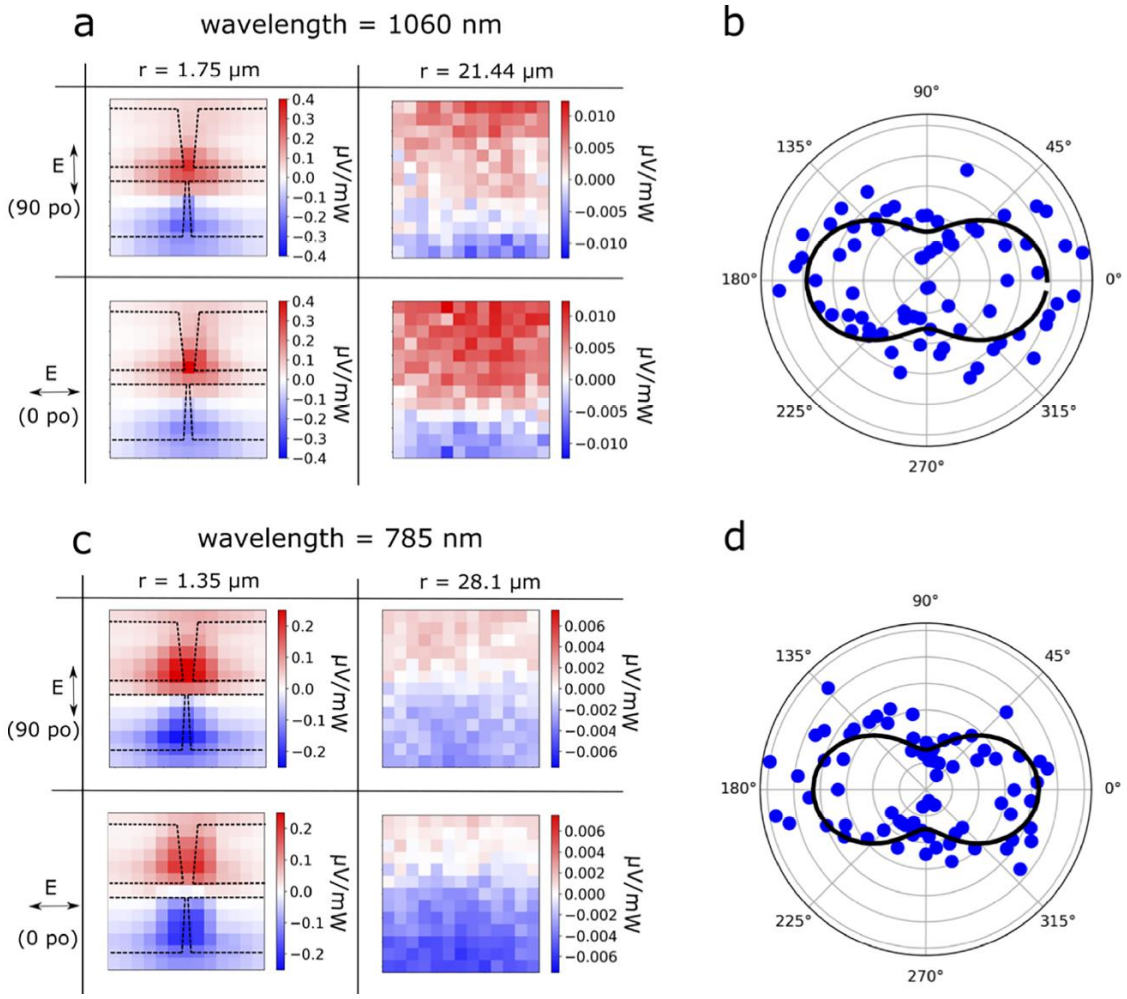

Figure 4.8. PTE results for a photodetector designed to respond to both 1060 and 785 nm wavelengths but with opposite signs of the signal. (a) PTE map for 1060nm wavelength. The first row shows the PTE map for longitudinal polarization for focused and expanded laser. The second row shows the PTE map for transverse polarization. The parameter r is the radius of the laser spot hitting the surface of the sample. (b) Polarization plot of the device shown in Fig. 3a, while the laser diameter is 43 μm and positioned in the middle of the device. The black line shows the (A × cos2 θ + B) fit result. (c) PTE map of the same device when a 785 nm CW laser is used as a heat source. In this case, when the laser is expanded, the negative signal is dominating the signal at transverse polarization, which corresponds to the transverse resonance of plasmons at 785 nm. (d) Polarization plot of the same device

when the 785 nm laser diameter is 56.2 μm and positioned in the middle of the device. The black line shows the (A × cos2 θ + B) fit result.

Fig. 4.9 below shows the simulated temperature distribution of the device shown in Fig. 4.8 when 1060nm and 785nm plane wave with the same intensity as the expanded Gaussian beam in experiment with transverse polarization is applied to the PD. It is obvious that when 1060 nm is applied, the wider side gets hotter, so the PTE signal is dominated by this side and when 785 nm is applied, the thinner side gets hotter and the PTE signal is dominated by the thinner side.

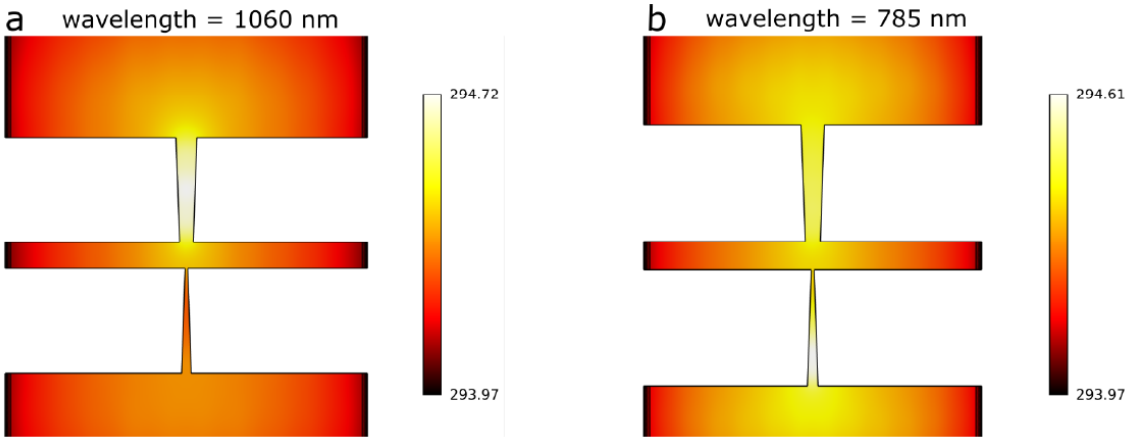

Figure 4.9. Simulation results of the temperature profile for the double wavelength photodetector presented in Fig. 3. a) 1060 nm plane wave with transverse polarization and with the same intensity and power as the expanded laser with a diameter of 43 μ m is applied to the geometry. b) 785 nm plane wave with transverse polarization and with the same intensity and power of the expanded laser with a diameter of 56.2 μ m is applied to the geometry. The temperature values are in Kelvin. Diameter of the expanded laser is the same as experimental results in Fig. 3.

4.5. Extracting the Seebeck map in tapered gold nanowires using simulations

We were able to infer reasonable values for Seebeck coefficient spatial distributions from several single tapered devices based on the experimental PTE maps by comparison with simulations in COMSOL Multiphysics. First, we use a modified Seebeck coefficient model and adapt it for our structure. Later, we simulate PTE response of out single metal PDs using COMSOL. Simulated PTE response match well with experiment PTE response. Also, the Seebeck map obtained from COMSOL matches well with the modified Seebeck coefficient model.

4.5.1. Modified Seebeck coefficient model

The Seebeck coefficient change in a thin film when the thickness is larger than the mean free path of the bulk can be written as:[112], [113]

Equation 4.2. Modified Mott formula for metals

$$\nabla S_F = S_{bulk} - S_F = S_{bulk}\frac{U}{U+1}\times\frac{3l}{8(1-p)t}$$

In which S_F and S_{bulk} are the Seebeck coefficients of the film and the bulk, respectively, l is the mean free path of electrons in bulk and $U = \frac{dl(E)}{dE}$ $(E = E_F)$, p is the scattering coefficient. Here we assumed S_{bulk} for gold is 1.5 μV/K . [114] U and p are respectively -0.6 [115] and 0.1 for polycrystalline gold films, and l is estimated based on (Eqn.2.9 can also be used)

Equation 4.3. Electrical conductivity of metals.

$$\sigma = \frac{ne^2}{mv_f} l$$

in which σ, n, e, m, v_f are electrical conductivity, density of charge carriers, electron charge, mass of charge carriers, and Fermi velocity respectively. In our tapered devices, the thickness is fixed and the widths of the nanowire change. All widths are larger than the mean free path of electrons in the gold bulk (also larger than the mean free path of a thin film). We adapted the same formula and substituted thickness with width, and instead of using the mean free path of electrons in the bulk (l in the formula), we used the estimated mean free path of electrons in the gold film with a thickness of 18 nm [116]. The black line in Fig. 4.14b represents the Seebeck coefficient change across the tapered nanowire using this model.

In this study, first, we calculated the Seebeck coefficient for an Au film with 18 nm thickness and infinite width and length and then used a similar formula to account for the width change across the device. Fig. 4.14a shows the assumed Seebeck map across the length of the tapered nanowire.

4.5.2. Simulating PTE signal

First, we simulated the temperature profile across the device when laser is focused and scans the length of the nanowire with 0.5 μm steps (same as the pixel

size in PTE maps in experiments). We also simulated the temperature profile when the laser is expanded and positioned in the middle of the device at two polarization The *T* profile simulations for a photodetector at 1060 nm are shown in Fig. 4.10. Later, we simulated the open circuit voltage at each laser position and each polarization by using the calculated T profiles. We assumed the difference in local Seebeck coefficient across the device to be α/w where α is a constant and $w(x)$ is the width across the tapered nanowire. We found the α that causes minimum deviation between PTE signal from simulation and experiment; In the case of applying a focused laser, first, the photovoltage signals across the length of the nanowire from the experiment and simulation are normalized to the maximum value from the experiment. This process is done for both polarizations. Then the square root of the sum of the square of the differences between simulation and experiment is calculated. The same process is done for the case when the expanded laser with transverse polarization is positioned in the middle of the device (for the expanded laser with longitudinal polarization, the signal amplitude is too small; Fig. 4.5a). The α corresponding to the minimum value for the sum of errors is recorded as the where the filled points are in Fig. 4.14. When the error is increased by 30%, the corresponding α is recorded as the top and bottom value of the error bars in Fig. 4.14. The dash lines in Fig. 4.12 show the PTE signal along the cut-through direction along the length of the tapered nanowire, and the blue plots in Fig. 4.12 are the cut-through signals across the length of the nanowire from the experiment. The cut-through simulated results for two polarization for a photodetector designed for 785 nm is shown in Fig. 4.12 in pink. Later, the results are plotted as the Seebeck

coefficient *vs*. the inversed width of the nanowire that is shown in Fig. 4.14b. The error bars for the simulation fits are dominated by systematic uncertainties in the experiment. As explained in the main text, the diameter of the focused laser on each device in the experiment might not be exactly the same size, but in the simulations, the focused laser has a fixed size. Each pixel size in PTE maps is 0.5 μm by 0.5 μm and the focused laser diameters for 1060 nm and 785 nm lasers are 3.5 μm and 2.7 μm, respectively. Both diameters are larger than the widths of the tapered nanowires. This causes a little shift to the cut-through plots when the window of the PTE map shifts for less than 0.5 μm. For example, the cut-throughs for two consecutive measurements are shown in Fig. 4.13. Here, the window in the second measurement is shifted by 0.3 μm in x and in the y-direction. The shifts in these cut-throughs are obvious. Also, the fabricated devices might not have perfect edges across the length of them. Imperfections can randomly change the scattering pattern across the length of the device and change the Seebeck coefficient based on the discussion in the introduction of the main text. The blue plot in this figure corresponds to the device described in Fig. 4.12. In these simulations, S_0 is assumed to be 1.5 μV/K, which is the absolute Seebeck coefficient of gold, [114] but this number does not change the PTE result simulations, as the open circuit voltage depends on relative Seebeck coefficients

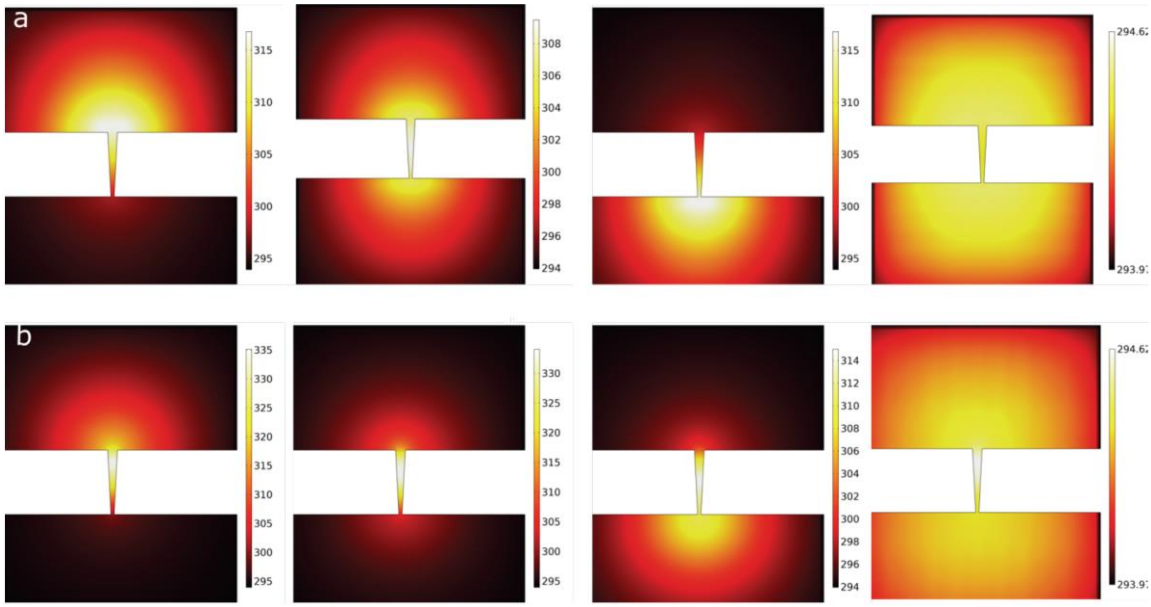

Figure 4.10. Temperature profiles of the device when using different laser positions and polarizations for the 1060 nm detector shown in Fig. 2a. a) When a longitudinal polarized laser is used. The laser is positioned on the top, middle, and bottom of the nanowire, respectively from left to right. The rightest plot shows the temperature profile when the laser is expanded with diameters of 43 μ m. For the expanded simulation, a plane wave with the same intensity as the expanded Gaussian beam is used as the optical source in simulations. b) the same results when a transversely polarized laser is used. All the temperature values are in Kelvin. The laser wavelength is 1060 nm in all the results. These results show that the plasmons increase the absorptions when transverse polarized light is used. When the laser is expanded, the temperature goes higher in the tapered nanowire when transverse

polarization is used. This proves the polarization dependency of these photodetectors.

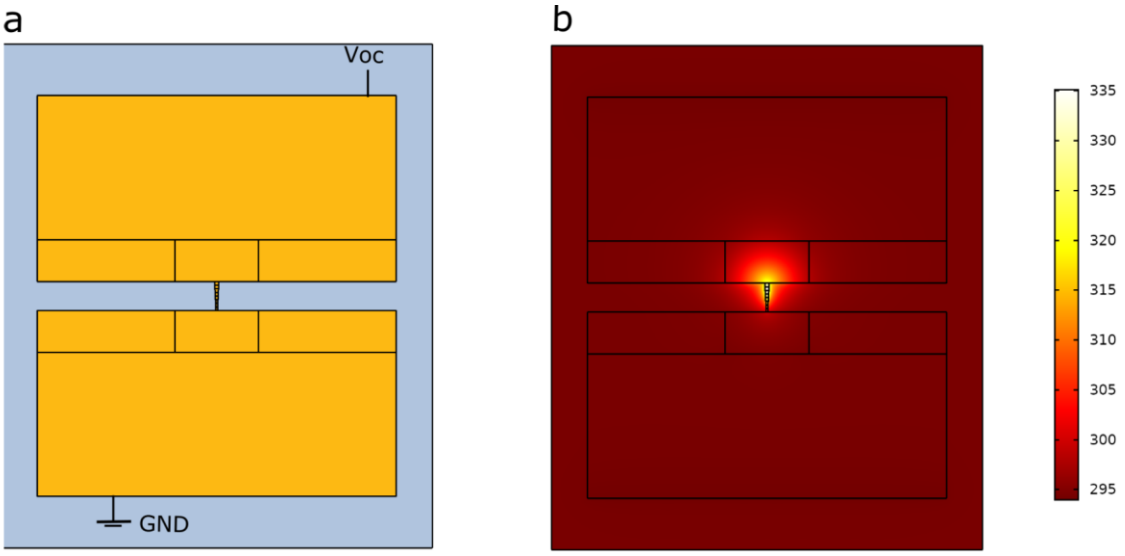

Figure 4.11. Simulation structure in Joule Heating simulations. a) the electrical boundary conditions, as well as the geometry, is shown. One side of the device is grounded, and the open circuit voltage is probed from the other end. b) temperature profile of the device. The temperature is imported from

electromagnetic and heat transfer simulations that their results are presented in Fig. 4.10. The temperature unit is in Kelvin.

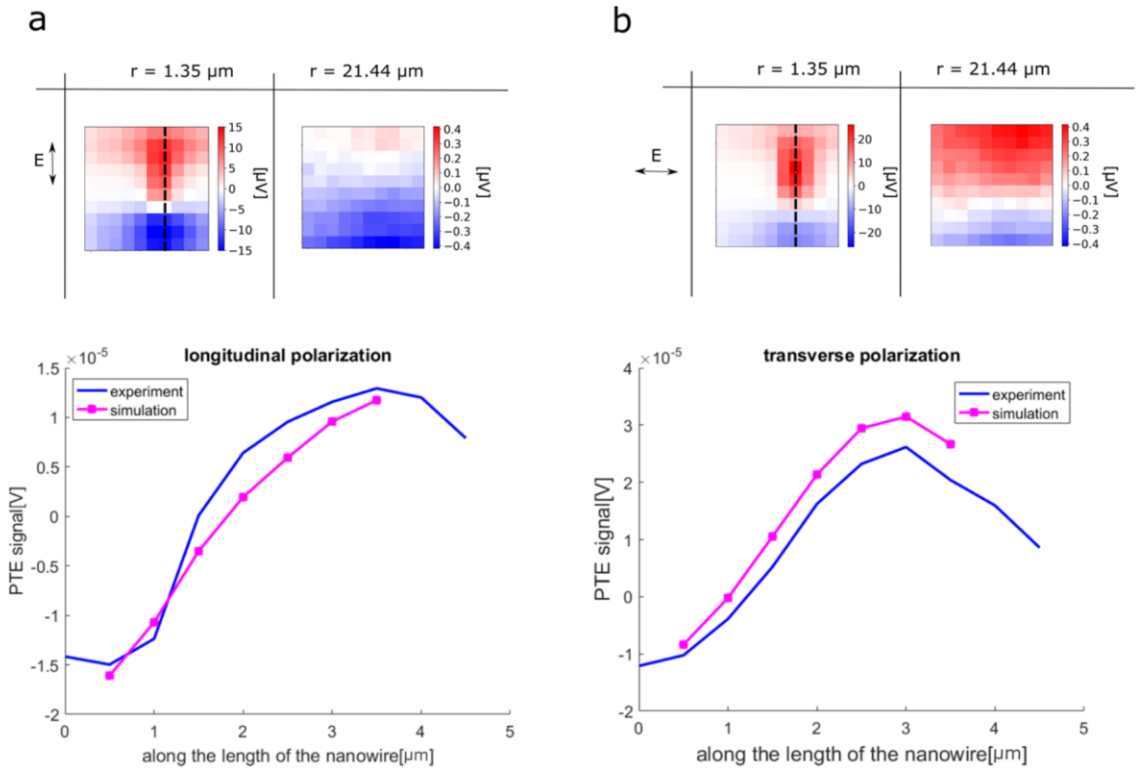

Figure 4.12. The simulation fit results for the Seebeck map of a single tapered nanowire photodetector. a) shows the results for longitudinally polarized laser. Focused laser and expanded laser results are shown on the top. The cut-through PTE signal from the dashed line on the focused PTE map is plotted on the bottom. The expanded signal from the middle of the device is considered to find the first fit parameters. The simulation results based on the calculated fit parameters are plotted in the bottom in pink for comparison with the experiment. The temperature profile for each of the dots in the pink plot is first calculated in COMSOL, then fit parameters, as well as calculated

temperature, are used to simulate photovoltage for each spot location. b) shows the same results for the transversely polarized laser.

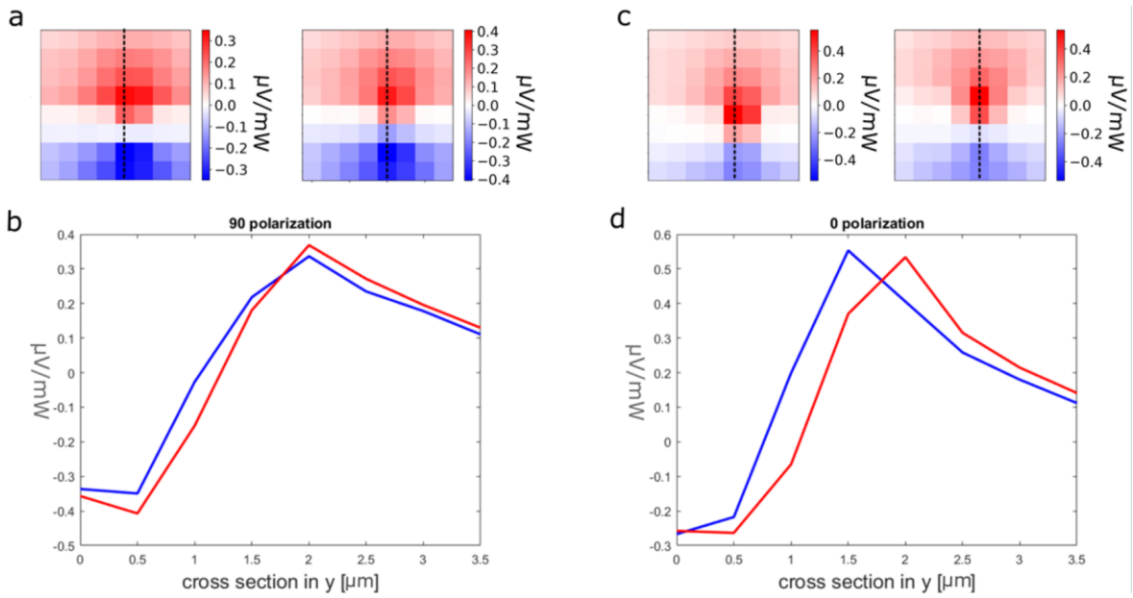

Figure 4.13. These plots show that when the PTE map measurement window is shifted for 0.3 μ m in x and y, the cut-through plot can change. a) two consecutive measurements at transverse polarization when the laser is focused. The second measurement window is shifted by 0.3 μ m in x and 0.3 μ m in the y-direction. b) cut-through from the dotted line on PTE maps in Fig. S5a. c and d) the same measurements in transverse polarization.

Fig. 4.14b shows simulation fit results of the Seebeck coefficient versus the inverse width of the Au nanowire at the thickness of 18 nm. Points of each color correspond to one device. The error bars in Fig. 4.14b for the simulation fits are dominated by systematic uncertainties in the measurements. For example, the diameter of the focused 1060 nm laser is close to the length of the tapered nanowire

(~3 μm), and each pixel size in the PTE map is 0.5 μm × 0.5 μm, so a small shift in the PTE map can change the inferred PTE cross section (see Fig. 4.13). More importantly, while acquiring PTE maps, there is some variation in the focus of the laser spot, while the spot is always assumed to be its minimum size in the simulations. As a result, the simulated temperature profiles and calculated PTE differ from experiments when the laser focus is poor. In Fig. 4.14b, the red data points correspond to a measurement taken with a defocused laser, which clearly has poor consistency with the other data sets and the simple theoretical model of the width variation of S. The Seebeck coefficients in Fig. 4.14a and b are plotted relative to S_0 shown in Fig. 4.14a. These simulations give us a good insight into the Seebeck coefficient relation as a function of the width of a gold nanowire at fixed thickness. These fits are consistent with the results with previous studies [112] plotted in black.

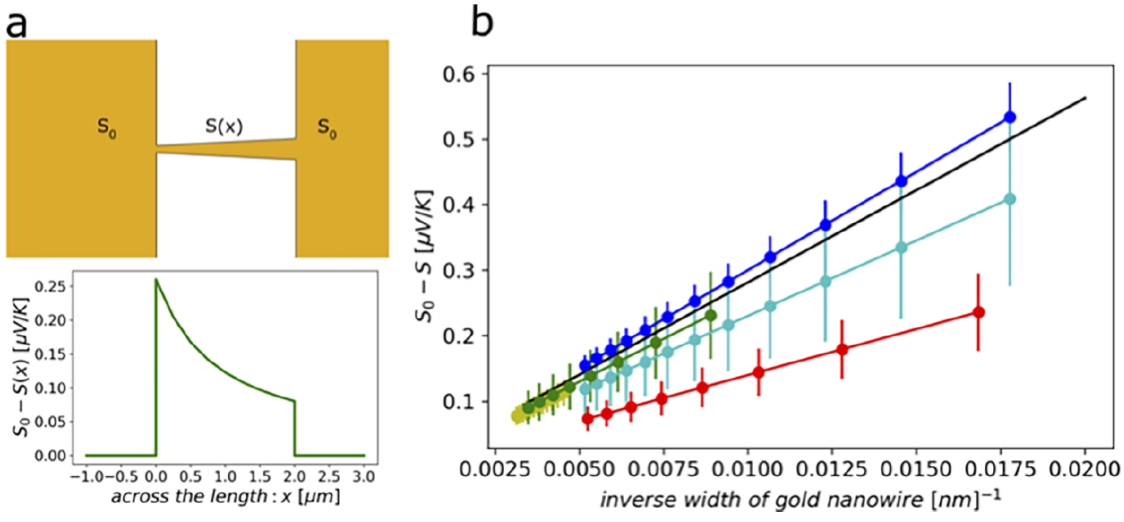

Figure 4.14. Simulation results of the Seebeck coefficient vs width of the gold nanowire. (a) Seebeck coefficient map across the length of the tapered

nanowire. Local deviation of Seebeck coefficient from the bulk value is assumed to be proportional to the inverse of the width of the nanowire (see the Supporting Information). (b) Results of the simulation fits of Seebeck coefficient vs inverse width of the gold nanowires with a thickness of 18 nm for five different devices. Each color represents a particular device. The black line represents the theory expectation (see the Supporting Information). The red and light blue plots correspond to a measurement with a defocused laser.

4.6. Characteristics of these photodetectors

4.6.1. Responsivity

For calculating the responsivity of these PDs (~10 mV/W), we used COMSOL simulations to calculate the effective area as it is described below. For comparison of this responsivity with semiconductor based PDs refer to Section 4.7.

The resistivity of the photodetectors can be increased by increasing the thermal boundary resistance to the substrate which either can happen by using a substrate with lower thermal conductivity or by measuring at lower environmental temperature [24]. Suspended structures can greatly increase the responsivity of these photodetectors.[116], [117]. It is also possible to design absorption unit separate from voltage active unit to improve the device responsivity [108], [118], [119]. Other studies achieved higher responsivity by designing cavities [120], antennas which achieve the impedance matching between light and nanoscale specimens, and improve light absorption efficiency. [121]

4.6.1.1. Effective area

For calculating the effective area, the field enhancement when the optical source is applied to the structure is simulated. In these simulations, an incident plane wave with the same intensity as the expanded Gaussian beam is applied to the photodetector to optimize between the accuracy and the computational power. The polarization of the laser is transverse to excite plasmon modes that are the basis of these photodetectors. The intensity of the optical source matches the experiment. The area that encloses 35% of the maximum field enhancement and above is defined as the effective area, which is an estimation for 90% of the response area defined in [96]. Fig. 4.15 shows the effective area for each of the photodetector described in the main text. Simulations show that the effective areas for the devices presented in Fig. 4.5a and Fig. 4.5c are 0.424 μm^2 and 0.265 μm^2, respectively. The effective area of the device presented in Fig. 4.8 differs at different wavelength. At 785 nm, the effective area is 0.393 μm^2 and at 1060 nm, the effective area is 0.863 μm^2.

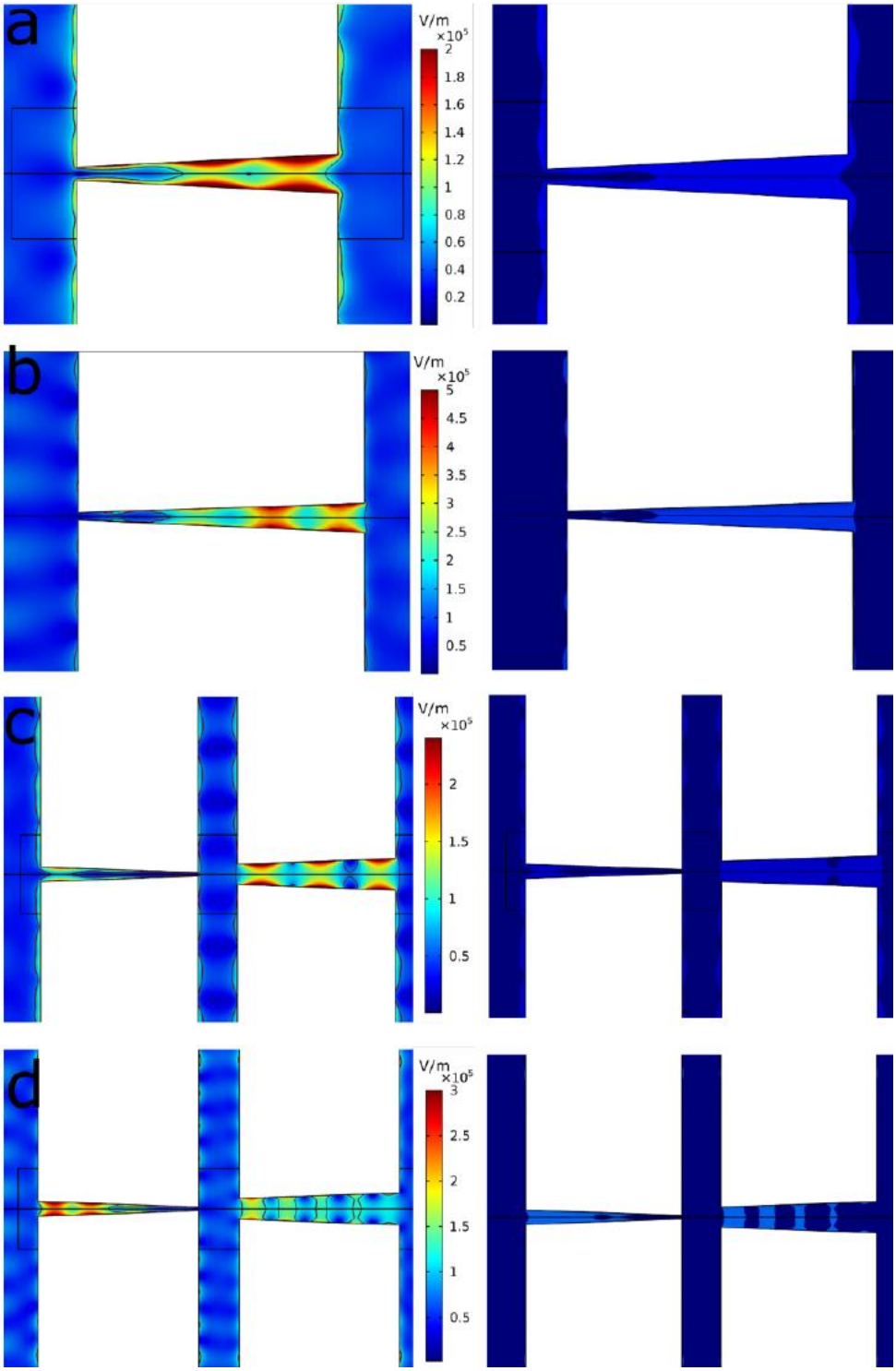

Figure 4.15. Effective area simulation of different photodetectors. The right column in each figure shows the total electric field plots overlapped with the effective area boundaries. The right column shows the effective area clearly.

The light blue areas on the right figures show the effective area and the dark blue is outside of effective area. a) Field enhancement and the effective area results for a detector designed for 1060 nm wavelength (Fig. 2a) at 1060 nm incident wavelength with transverse polarization. b) Field enhancement and the effective area results for a detector designed for 785 nm wavelength (Fig. 2c) at 785 nm incident wavelength with transverse polarization. c) Field enhancement and effective area results for the photodetector presented in Fig. 3 at 1060 nm. d) Field enhancement and effective area results for the photodetector presented in Fig. 3 at 785 nm.

4.6.2. Detectivity

The effective area and the noise results of these photodetectors are used to calculate the detectivity. In the following equations, D*, A, and NEP are detectivity, effective area, and noise equivalent power, respectively. The noise measurement is described in the next section.

Equation 4.4. Detectivity formula for a photodetector

$$D^* = \frac{\sqrt{A}}{NEP}\left[\frac{m\sqrt{Hz}}{W}\right]$$

Equation 4.5. Noise equivalent power formula for a photodetector

$$NEP(noise\ equivalent\ power) = \frac{noise\left[\frac{V}{\sqrt{Hz}}\right]}{Responsivity\left[\frac{V}{W}\right]}$$

Similarly, in an ideal device with the noise solely limited by Johnson-Nyquist noise in the antenna itself, the NEP would be 11.9×10-8 W/$Hz^{1/2}$, and D^* would be 5.47 m $Hz^{1/2}$/W.

4.6.2.1. Noise measurement

To find the thermal noise of the detector, the sample was mounted on a custom low-frequency measurement probe and inserted into a cryostat (Quantum Design PPMS) with temperature stability better than 0.02% in the relevant temperature range. The measurement wirings are twisted pairs to reduce magnetic field induced noise. The sample, transmission lines, and the first pair of pre-amplifiers are shielded by a Faraday cage to reduce environmental noise. The voltage noise in the device is collected by two separate amplifier chains, each consisting of two preamplifiers (NF LI-75 and Stanford Research SR560, each with gain of 100). The two amplified signals are recorded by a high-speed data acquisition system (Picoscope 4262). Each time series containing 2,000,000 data points is taken with a sampling rate of 10 MHz. The two voltage time series are cross-correlated, revealing the true sample noise since the amplifier noise is nominally uncorrelated between the chains. We measured the Johnson noise at five temperatures around room T; 292.5-294.5 K. This is a relevant temperature range, as the simulation results show that while using an expanded laser with transverse polarization, T goes up by ~1 K; Fig. S4.10. The results of the noise measurements are shown in Fig. 4.16a. The results match well with the theoretically expected value for our device with ~115 ohm resistance. ($4k_BTR$= 1.84×10-18 [V^2/Hz]). The

thermal noise is measured 15 times at each temperature point. The vertical lines in Fig. 4.16a show the standard deviation of the thermal noise measurements at each temperature. Thus, the minimal noise theoretically possible in the detector operated at room temperature is about 1.35×10-9 V/Hz$^{1/2}$. To measure the noise of the unoptimized measurement system, the PTE map of the same device has been acquired with the laser being completely blocked. The chopper is still on and the lockin amplifier's reference frequency is locked to the chopper frequency. The bandwidth of the lockin amplifier with the time constant of 200 ms and the output filter slope of 12 dB/Oct is 0.84 Hz. An example of the measured noise as a function of mapping position in this case is shown in Fig. 4.16b. As shown here and in four successive identical mapping runs with the laser off, the maximum noise amplitude of the PTE signal, is ~30 $\frac{nV}{\sqrt{Hz}}$. This significantly exceeds the theoretical limit of the detector thermal noise. The measurement setup noise floor may be improved through the use of a voltage preamplifier optimized for the detector impedance. At our measurement frequency and at room T, the present voltage amplifier (Stanford SR560) has a minimum noise for a resistance as large as 100 kΩ. The low resistance of our devices, ~120 Ω, increases the noise of the preamplifier

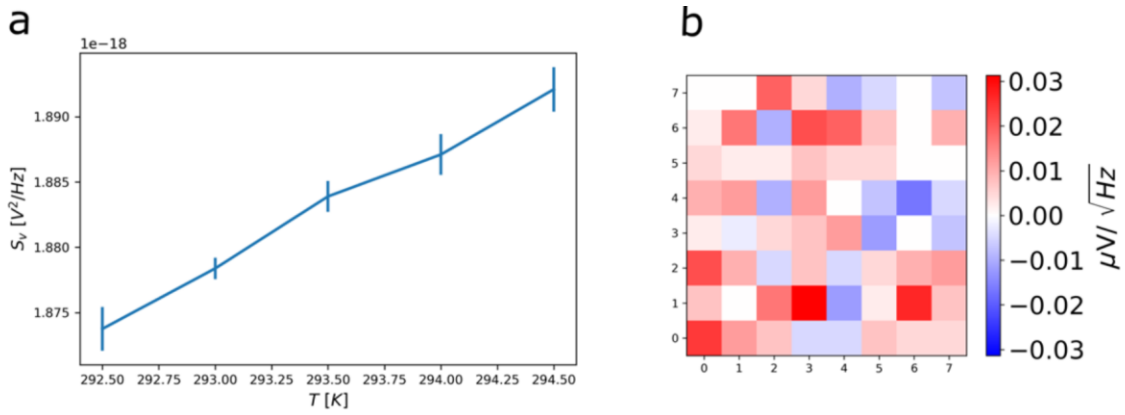

Figure 4.16. Noise measurement. a) Thermal noise measurement of a device at five points around the room T. The thermal noise is measured 15 times at each temperature. The vertical lines define the standard deviation of the measurements. b) PTE map of the device when laser is off.

4.6.3. Response time

COMSOL simulations of the PTE response have three steps: 1- wave optics simulations in a frequency domain where the light-matter interaction is simulated and the losses in the gold film is calculated. 2- heat transfer in a stationary state where the heat source comes from the losses calculated in the previous step and the temperature profile across the device is calculated. 3- joule heating where the temperature profile comes from the previous step and the open circuit voltage based on the Seebeck coefficients across the device is calculated. Time dependent simulations for the second and third steps can give us a good estimation of the response time of these photodetectors. The results are shown in Fig. 4.17, where it shows a response time of around 8 microseconds.

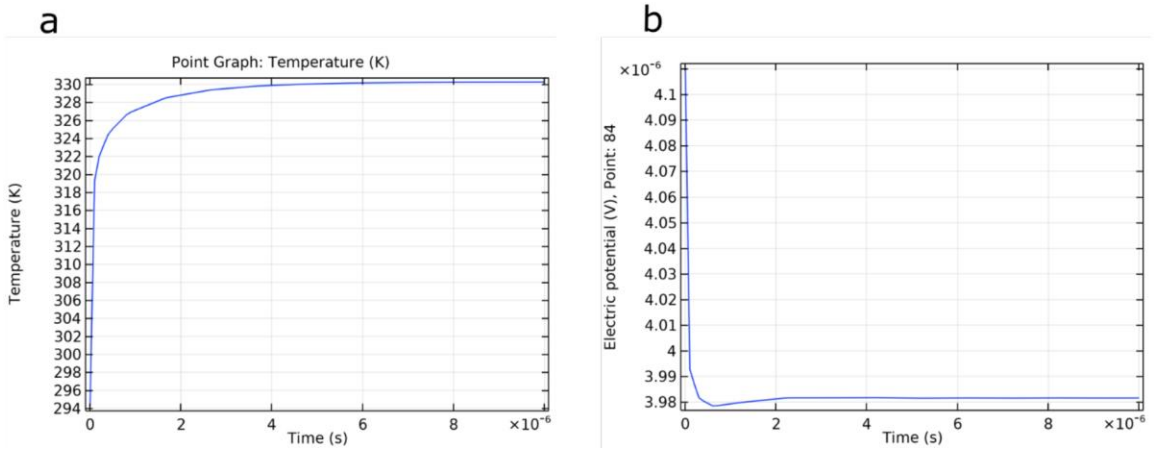

Figure 4.17. Time dependent simulations. a) Time dependent thermal simulation that shows stationary behavior at ~10 μ s. b) Time dependent PTE signal simulation that shows stationary behavior at ~8 μ s.

4.7. Comparison of different photodetectors

The responsivity of PTE photodetectors based on semiconductors can be as large as volts per watt.[5], [108] Semiconductors have a higher Seebeck coefficient and smaller heat capacity compared to metals. The single-metal structures in this work have responsivity comparable to some graphene-based photodetectors [5], [122] and have a comparatively simple (single-material) fabrication process, streamlining large-scale fabrication. Because of plasmonic resonances, such plasmonic PTE structures can harvest light over an area larger than their geometric size,[101] with polarization and wavelength selectivity. While gold has comparatively poor Seebeck response, its structures are chemically stable and

enable plasmon-based photodetection in the near IR range. Simulation results show that the responsivity of a metallic based photodetector comprising several thermocouples made by two different metals with high S difference can be as large as 112 mV W. [105] The fabrication process of a single metal photodetector is much easier. The response time of these detectors is set by the thermal time scales for the structures and is estimated to be slower than the photodetectors based on hot carriers [27], [123] and faster than some photodetectors based on semiconductors.[5], [108]. It is possible to increase the responsivity of photodetectors presented here by fabricating several of them in parallel. Decreasing the thermal conductivity to the substrate also can increase the responsivity by increasing the temperature rise for a given incident optical power. Changing the substrate or decreasing the temperature of environment [24]. As it is shown, the response time of the PTE based photodetectors are limited phonon interactions, which is typically on the order of milliseconds [124]. Photovoltaic based photodetectors are faster, have better responsivity and noise level but their response is limited by the active material bandgap. Spectral measurements have been used to distinguish PTE vs PV responses [125], [126]. PTE based PDs have linear I-V characteristics vs PV based PD do not as they have nonlinear I-V characteristics because of their built-in electric field. Using low-dimensional materials can improve the speed of PTE based photodetectors by introducing hot-carrier-assisted photodetection in which the heat is generated by charge carrier while the lattice remains cool. [123] Hot-carrier-assisted happens when the channel

length is shorter than the cooling length of hot carriers. The estimated cooling length is calculated as [127]:

Equation 4.6. Cooling length

$$\xi = \sqrt{\frac{k}{\gamma C_{el}}}$$

where k is the thermal conductivity, γ is the cooling rate, and C_{el} is the electronic heat capacity. Note that in this regime, the carriers move diffusively. When channel length is less than the mean free path of charge carriers the transport is in ballistic regime which is the focus of Chapter 6.

Metallic PTE based photodetectors have lower resistance than semiconductor PTE based photodetectors on average. This causes lower Johnson noise level. The fabrication of the single metal PTE based photodetectors presented here are easier than semiconductor PTE based photodetectors as well as metallic PTE based photodetector using several metals. Plasmons can be excited in metallic based photodetectors that enhance the light-matter interaction.

4.8. Conclusion

Simple geometrical variation in gold nanowires can change the Seebeck coefficient as well as the plasmonic resonance behavior of gold nanostructures. Here, we combined these two traits to fabricate photodetectors with a single metal

based on the photothermoelectric effect. These wavelength-dependent and polarization-dependent photodetectors are simple to fabricate, and by understanding the system, it is possible to engineer and design a photodetector that can detect and discriminate two target wavelengths. Using knowledge of the mechanisms at work, the Seebeck coefficient variation versus width change of the nanowire at 18 nm thickness is extracted from experimental results using comparison to finite element method (FEM) simulations. We can further increase the responsivity of these devices by changing the thermal conductivity to the substrate and by optimizing the Seebeck map based on the Seebeck coefficient change versus width of the nanowire. For photodetectors in other operating wavelength ranges, other plasmonically metals can be used, for example, Al or Ag.

Detectivity, responsivity, and response time of these photodetectors can be improved in metallic based photodetectors by introducing hot carrier tunneling to the picture. This will be the focus of Chapter 6.

Chapter 5

Characterizing internal strain and Pt impurity on PTE response of single crystalline gold nanowires

This chapter is based in part on the publications:

"Thermoelectric response from grain boundaries and lattice distortions in crystalline gold devices," C. I. Evans, R. Yang, L. T. Gan, **M. Abbasi**, X. Wang, R. Tralor, J. A. Fan, and D. Natelson, PNAS, **117**, 38, 23350-23355 (2020), and

"Detection of trace impurities in noble metals by the photothermoelectric effect," C. I. Evans, L. T. Gan, R. Yang, **M. Abbasi**, X. Wang, R. Tralor, J. A. Fan, and D. Natelson, J. Phys. Chem. C, **125**, 31, 17509-17517 (2021),

5.1. Motivation

It has been discussed in Chapter 1 that based on Mott formula [7], by manipulating the mean free path of the electrons, it is possible to change the Seebeck coefficient in metals. In Chapter 3 single metal photodetectors are discussed that are designed by changing geometry across plasmonic asymmetric nanostructures. Beside geometry, there are other factors that can change the scattering pattern and so the Seebeck coefficient in metals. Previous results show that when the length of the nanowire in single metal gold structure is larger than the laser spot size, the PTE signal shown the localized variation in the Seebeck coefficient in long nanowires with fixed geometry [21]. In our lab we have characterized factors like crystal misorientation and strain [104], impurity[103], and surface chemistry [19] in Seebeck coefficient change. This Chapter focuses on how Seebeck coefficient changes in single crystalline gold nanowires by crystal misorientation and strain [104] and impurity [103]. Long single crystalline gold nanowires and bi crystalline gold nanowires with single grain boundary are fabricated in Prof. Fan lab; Fig. 5.2. In these devices the electron scattering off of grain boundaries are eliminated that enables us to characterize different factors in sets of controlled measurements described below. By matching the COMSOL simulations with the experiments, it is shown how much magnitude of Seebeck coefficient is needed for the voltage map seen in experiments. Further this knowledge can be utilized to probe internal strain and impurity of an unknown structure with high accuracy using a simple opto-electrical measurement.

There are other ways for measuring the Seebeck coefficient variation with spatial higher resolution, like using scanning tunneling microscopy [128] with a temperature difference between tip and sample, or using AFM with conducting tip [129], [130]. In these measurements, getting high resolution at the order of the atomic scale is possible so each small defect can be mapped. Related approaches are also useful for measuring the Seebeck coefficient of a single molecule junction [131]. In our study, with a simple opto-electronic measurement, we can infer the localized Seebeck coefficient variations that are caused by factors like nanometer-sized changes in the geometry, strain, and impurities.

Comparing with current methods for measuring strain and impurity: measuring open circuit voltage is better than measuring short circuit current as applying current anneals devices and perturbs the impurity distribution in devices.

The PTE experiments described in this chapter were largely performed by Dr. C. I. Evans and discussed in her doctoral thesis. I performed the simulations that allowed the interpretation and analysis of the PTE data, and these efforts are described below.

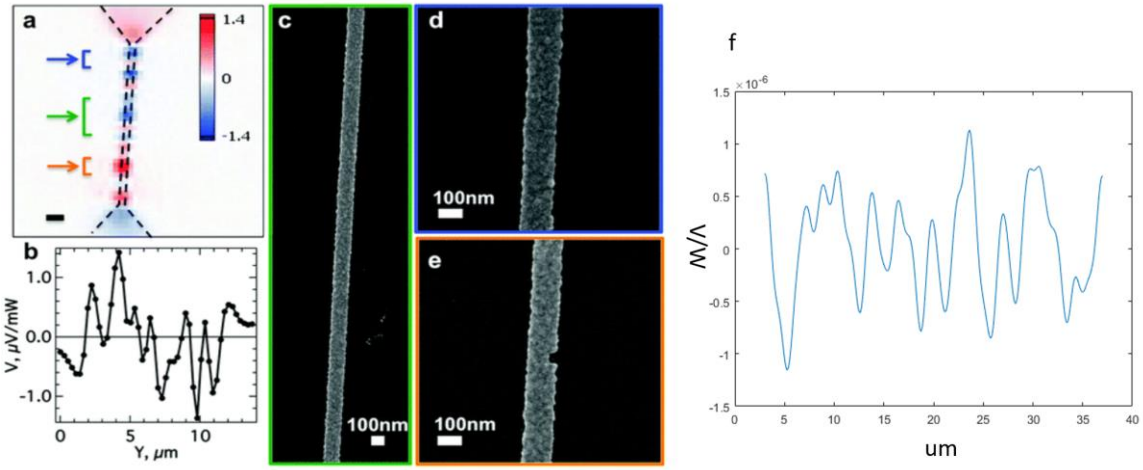

Figure 5.1. Bowtie devices with long nanowires display extreme spatial variability of the PTE voltage along the nanowire. (a) PTE voltage map of a typical 10 μm long and 100 nm wide Au/Ti device, in units of μV mW−1 of laser power on the sample. Scale bar is 1 μm. Substrate temperature is 5 K. (b) Variation of the PTE voltage along the length of the device. (c) SEM image of the central part of the nanowire; the displayed area is highlighted in (a) by the arrow in the center. (d), (e) the same as (c), but in the top and bottom section of the device. Figures a-e with permission from [21]. f)COMSOL simulation PTE results of a randomly changing S (between 5.9-7 μV/K) across the nanowire with similar geometry proeprties as device shown in c.

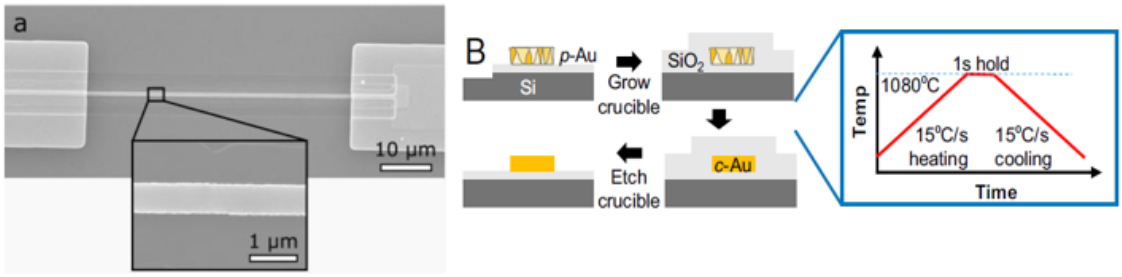

Figure 5.2. a) bicrystal gold nanowire with single grain boundary. Zoomed in SEM image clearly shows the single grain boudary in this structure. b) fabrication steps of a single crystalline gold nanowire. First, the polycsytalline gold nanowire is encapsulated with silicon oxide. The system is heated up

with high rate of 15 defree/second to 1080 degrees celcius where the gold is melted. After a second, the structure is cooled down with the same rate to form single crystalline gold nanowires. In the end, the crucible is etched away, the nanowire is formed by ion milling, and the large gold pads are fabricated on top. Figure with permission from [132]

5.2. Simulation details and results

In this section, the simulation steps to extract the Seebeck coefficient map across single crystalline gold nanowires are presented.

First, a traditional thermocouple consisting of two metals in contact with each other was simulated. The device geometry is seen in Fig. 5.3a and matches that of an actual bicrystal device. Each grain had identical thermal properties but were assigned a unique S, varying by ~ 10%, which assumed to be grain-to-grain variation in S that could describe the magnitude of PTE voltages measured in previous works involving polycrystalline wires [21]. The thermal conductivity for the 100 nm gold film was 200 W/m·K [49], [133]. A Gaussian heat source with the same FWHM as the laser beam in the experiment, 1.8 μm, is applied to the surface of the structure. Because the diameter of the heat source is much smaller than the length of the wire, the two ends are kept at a constant room temperature. The temperature of the bottom of the substrate is also set to be at room temperature, which serves as a heat sink. One end of the structure was assigned to have zero voltage and the open circuit voltage was probed from the other end of the device as the heat source scanned the length of the wire. Fig. 5.3b shows an example of the temperature profile of device with the heat source located in the middle.

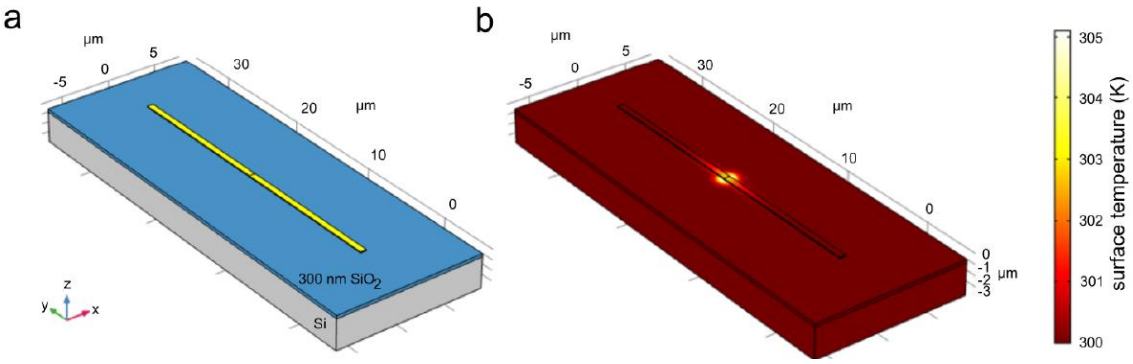

Figure 5.3. a) Geometry of a traditional thermocouple in COMSOL Multiphysics. b) Temperature profile of the structure when a Gaussian heat source heats up the junction between two metals.

The power for the heat source in the Joule Heating physics simulation is obtained by calculating the total absorption power for the structure when the Gaussian beam is applied to the structure using Electromagnetic Waves (*emw*) physics. The polarization of the field is perpendicular to the length of the wire, the same polarization as the experiment. The total absorption calculated from *emw* is used as heat source power in Joule Heating physics simulation. The resulting open circuit voltages are normalized to the incident power calculated from the *emw* simulations (1 mW) to compare to the normalized experimental results. Fig. 5.4a shows the geometry of the nanowire used in the *emw* simulations when a Gaussian beam propagating in the +*z*-axis illuminates the nanowire. The permittivity of gold was taken from Johnson-Christy values [94]. Fig. 5.4b shows the total power

absorbed by the gold structure when illuminated by a 1.8 μm FWHM, 785 nm CW beam. Absorption occurs on the order of the skin depth which depends on frequency and intrinsic material properties.

The total absorbed power changes with device width. Gold wires with width of 600 nm and 700 nm absorb 33.3 μW/mW and 35.5 μW/mW, respectively. Because the widths of the wires are smaller than the diameter of the beam profile, the total power of the heat source was corrected. The power for a Gaussian beam in focus ($w(z) = w0$) in the range for x between –0.3 μm and 0.3 μm and y in range of -1 to +1 can be calculated as:

Equation 5.1. Correcting optical absorbed power for the heat source power

$$P = \int_{-\infty}^{+\infty} \int_{-0.3\mu m}^{0.3\mu m} \frac{1}{2z_0} \exp\left(\frac{-2r^2}{\omega_0^2}\right) dxdy = 0.5633P_0$$

As a result, the total power of Gaussian heat source for devices with width 600 nm and 700 nm should be 67.255 μW and 62.67 μW, respectively, for Joule Heating simulations. Simply assigning each grain in the bicrystal device its own S results in behavior of a traditional thermocouple, Fig. 5.5, where the largest signal occurs when the heat source is incident on the interface of the two materials. This behavior is not observed in experiment.

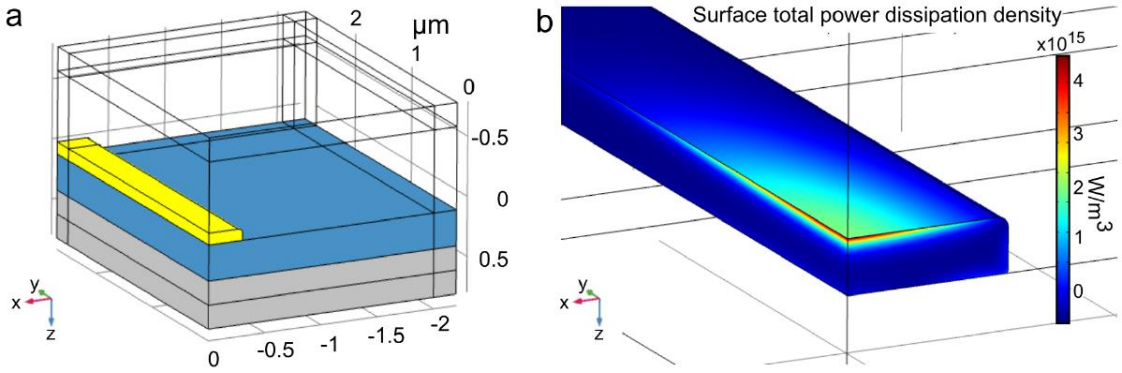

Figure 5.4. a) Geometry of the structure in electromagetic simulations in COMSOL Multiphysics. A quarter of the structure is simulated due to symmetry. b) The zoomed-in plot of the total absorbed power by the gold

structure when a Gaussian beam with diameter of 1.8 μm and power of 1 mW is applied to the structure.

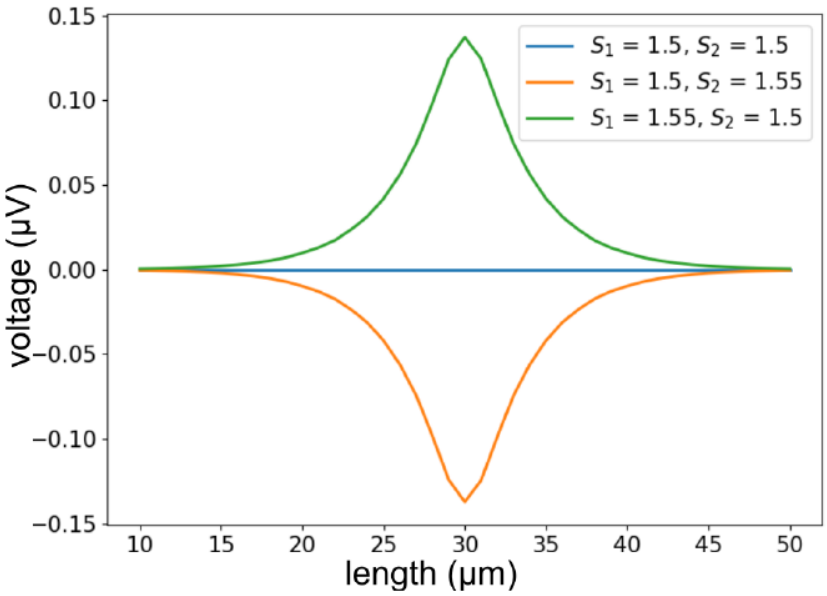

Figure 5.5. Simulation results of treating the bicrystal as a traditional thermocouple, assigning each grain its own value of S. green: The first grain is assigned S = 1.55 μV/K and the second is assigned S = 1.5 μV/K. black: The S values in the green curve are swapped, resulting in the same magnitude but opposite polarity. blue: Both grains are assigned the same S value, resulting in no change of signal when the interface is heated.

Some defects result in large PTE signal that changes polarity when the defect is heated [104]. One way to observe this change of polarity is to assign the defect its own S. Fig. 5.6a shows the simulation results of assigning different S_{def} values to a 3 nm stripe inserted between two long wires with a constant S = 1.5 μV/K depicted in Fig. 5.4a. In this type of structure, heating the 3 nm stripe results in a change of polarity with equal magnitudes of PTE voltage on either side of the defect as

observed in experiment. As the difference of *S* between the defect and the two crystals become large, the resulting open circuit voltages become larger. The total magnitude at high *dS* becomes saturated due to limited temperature boundary differences in the 3 nm length when the heat source diameter is 1.8 μm. Normalizing the open circuit voltages show that different d*S* between the defect and the bulk do not change overall length scales that are set by the size of the heating source (Fig. 5.6b).

Changing the thermal boundary resistance between the two long wires can change the overall magnitude of the resulting open circuit voltages. Fig. 5.7a demonstrates that decreasing the thermal conductivity of the 3 nm stripe results in increasing open circuit voltages due to a less spread out temperature profile. At room temperature, the thermal boundary resistance at the interface of the two gold crystals should be reasonable [134]. Fig. 5.7b shows the normalized plots seen in Fig. 5.7a, showing that the observed length scales are unchanged that are set by the size of the heating source.

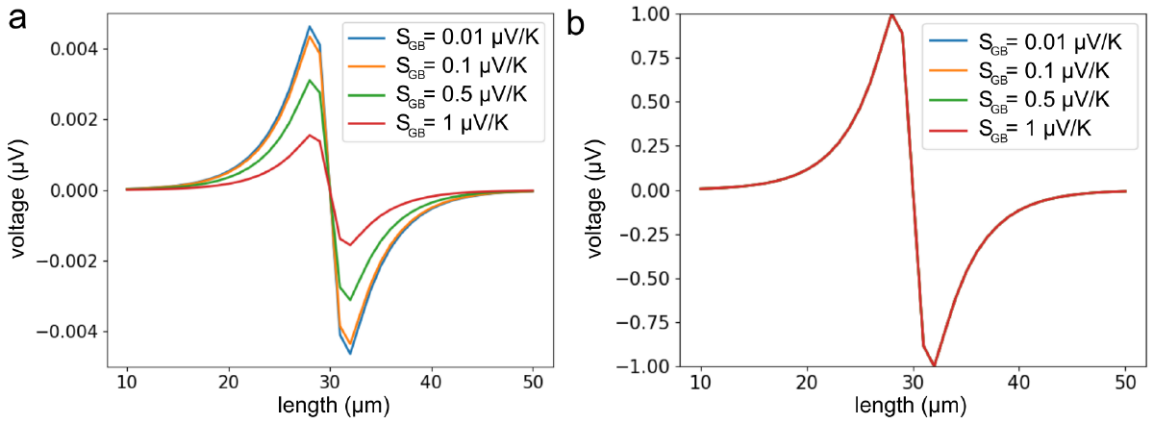

Figure 5.6. Assigning a 3 nm wide stripe with a unique S value results in a change of polarity. a: Resulting open circuit voltage when a 3 nm wide stripe with a unique SGB value, Sdef , is placed between two long wires assigned with *S* of bulk gold (1.5 μV/K). b: Normalized plots from a show that the length scales are unchanged with changing S_{def} .

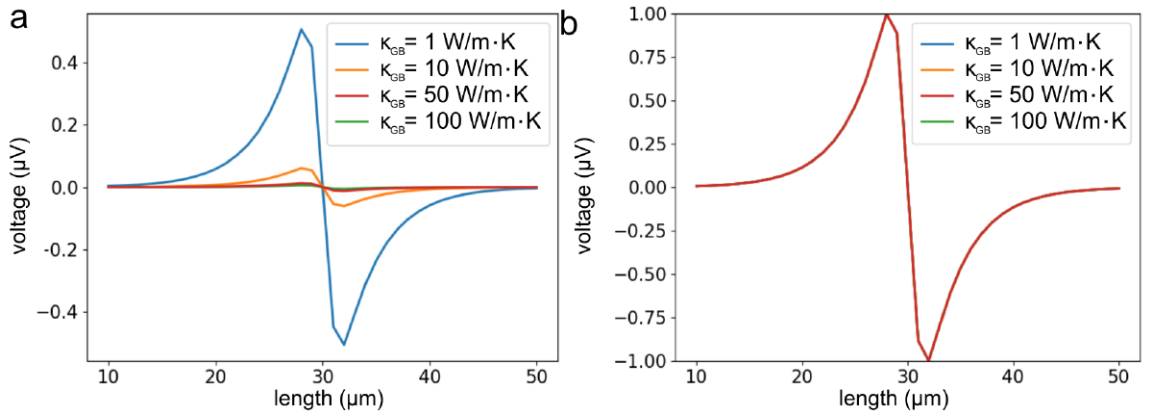

Figure 5.7. Controlling the amplitude of the peaks by changing the thermal conductivity of the 3 nm defect, S_{def} . a: Results when the thermal conductivity of the 3 nm stripe is changed while Seebeck coefficient of the stripe is fixed to 0.5 μV/K and the Seebeck coefficient of both long wires are 1.5 μV/K. b:

Normalized plots from a show that the length scales are unchanged with changing thermal conductivity of the defect.

In order to observe the length scales and magnitudes of the PTE voltages observed in experiment, the Seebeck coefficient needed to vary along the length of the wire. Fig. 5.8 shows the geometry of a simulated device consisting of two large pads at either end and a long wire divided into 0.5 μm long sections. Each section is assigned its own S and each pad was assigned S of bulk gold (1.5 μV/K). Spatially varying S along the wire, as shown in Fig. 5.9 and 5.9, resulted in open circuit voltages of length scales and magnitudes that closely matched that of experiment, Fig. 5.9a and 5.9c. While this is not a unique inversion of PTE voltage to $S(x)$, it is illustrative of the magnitudes of variation required for $S(x)$ to lead to the observed PTE profile. Fig. 5.10 shows the comparison of the simulated and experimentally measured open circuit voltages of the annealed and unannealed bicrystal devices, as well as the corresponding Seebeck coefficients that provide these simulated voltages. The Seebeck coefficient for the annealed device requires smaller spatial variations than that of the unannealed device to observe the magnitudes in the open circuit voltages seen in experiment, as seen in Fig. 5.10b and 5.10d respectively. S changes with a comparably larger step at the interface between nanowire and the pads. The pads made from polycrystalline gold and have more thickness comparing to the nanowire. So the scattering patterns changes a lot at the interface. [17], [18], [135]

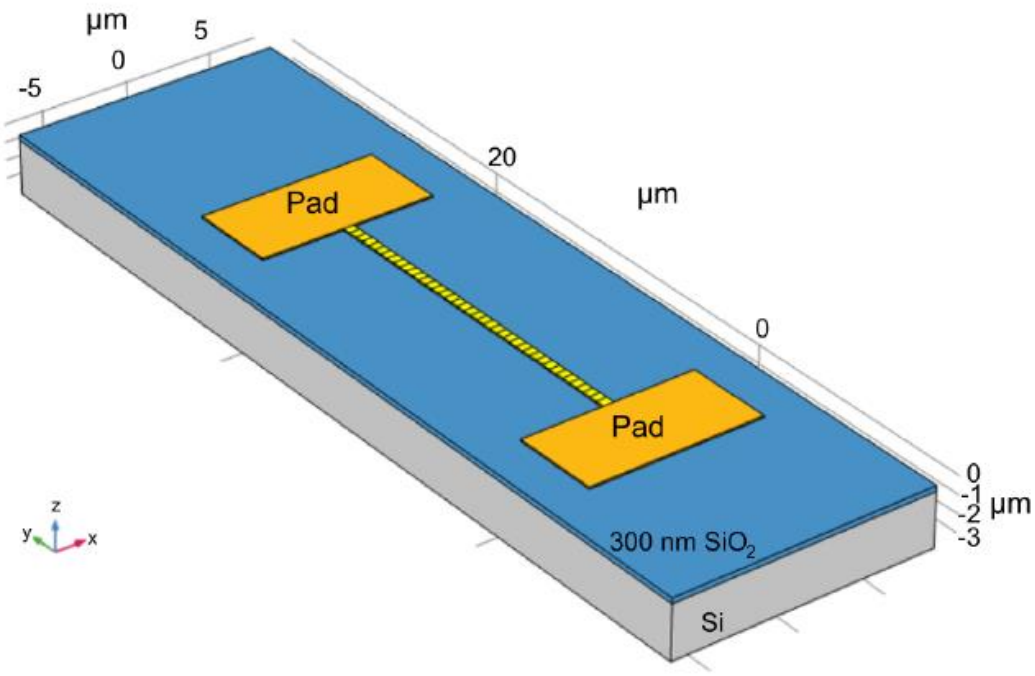

Figure 5.8. Structure of the nanowire divided into 0.5 μm long pieces.

For each simulation fit presented here, first, the optical absorption based on geometry is simulated as described, then the gradient of Seebeck coefficient similar to Fig. 5.8 is simulated several times to find the best Seebeck coefficient map by fitting to the PTE maps obtained from the experiments.

5.3. Internal strain and crystal misorientation effects on S

5.3.1. Crystal misorientation

EBSD is a SEM-based technique in which backscattered electrons form a diffraction pattern that provides information about the local crystallographic structure of the imaged sample. EBSD data are used to plot a 2D intragranular misorientation maps (IGM) to uncover small changes between neighboring points in the crystal [104]. By comparing IGM data with PTE measurements; Fig. 5.9a and Fig. 5.9c, we find strong correlation between a small misorientation in the single crystal and the PTE signal. By extracting the Seebeck map using COMSOL (inset in Fig5.9.b and Fig5.9.d), ~2 degree misorientation in single crystalline gold nanowires can cause ~0.045 μV/K Seebeck coefficient change in these devices. (S varies ~0.2% over 1 μm). Although there is not a single unique solution for the spatial variation in S, the simulations provide insight on the overall magnitudes of changes in required to produce the magnitude and length scales of the S observed PTE voltages. For a sense of scale, measurements on bulk polycrystalline gold wires imply that tensile strain of 100% would change the bulk S by 6.3 μV/K [136]. The small changes in S inferred from the simulations would then correspond to effective local tensile strains of ~0.15%, although caution is warranted in any comparison with macroscopic measurements on polycrystalline wires.

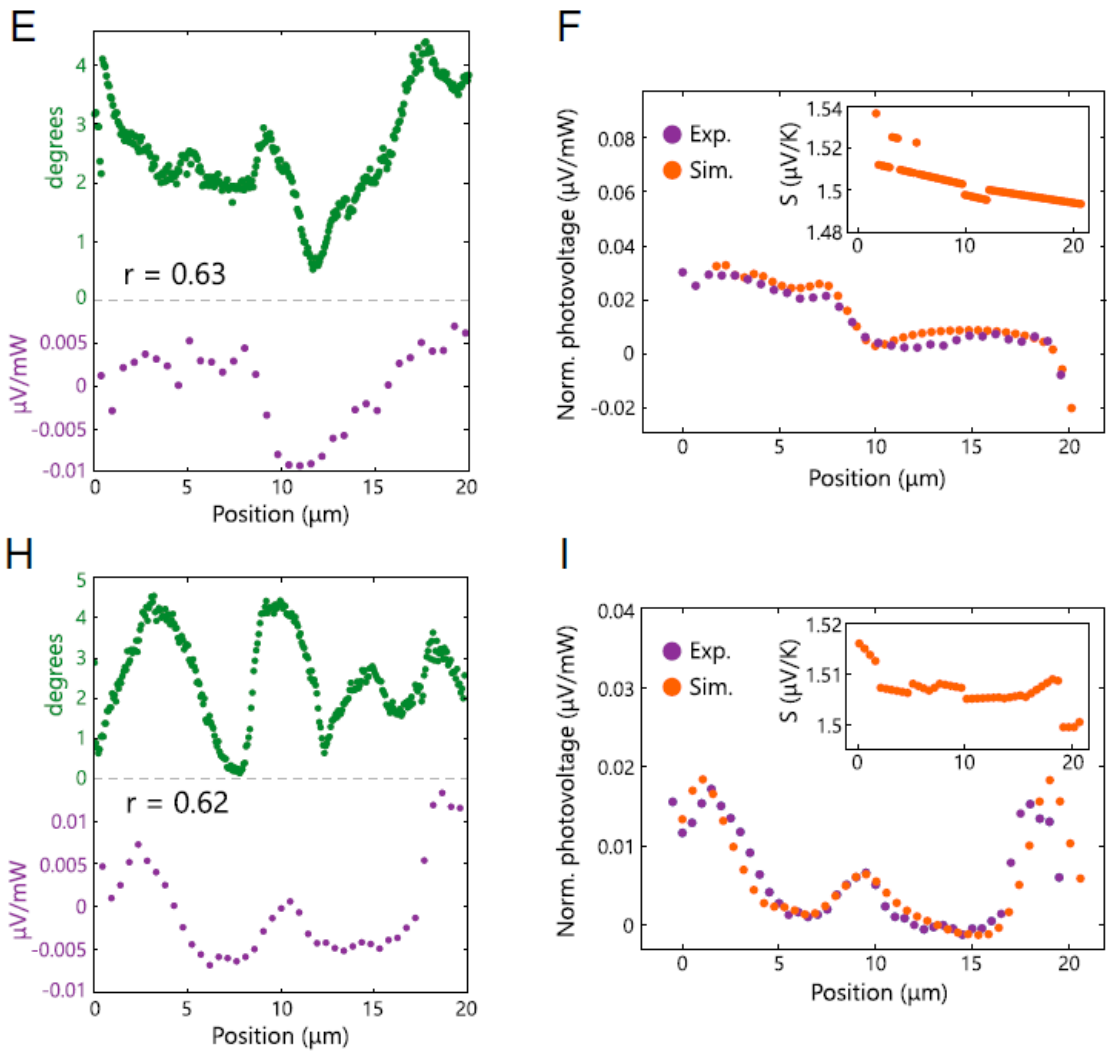

Figure 5.9. Strong coupling between crystal misorientation and PTE cross section. Simulation results show S changes ~0.2% over 1 μm. The Pearson correlation coefficient *r* was computed to determine the linear correlation.(E and H) Scatter plots of (Top) IGM angle and (Bottom) normalized PTE voltage as a function of laser position along the length of the wire, with a linear-in-position background subtracted to highlight the spatial variations (SI Appendix). The r values are 0.63 and 0.62, respectively, indicating a strong degree of linear correlation between the PTE voltages and IGM angles. (F and I) Scatter plots comparing the experimentally measured and simulated PTE

response. (Insets) Examples of the local variation in Seebeck coefficient resulting in the PTE response simulated via finite-element modeling.

5.3.2. Internal strain

Bicrystal gold nanowire with single grain boundary were also measured and their Seebeck coefficient maps were characterized. These results can show how much scattering from grain boundaries is important in PTE signal variation in polycrystalline gold nanowires. In the figures below, location of the grain boundary is shown with dash black line across PTE and Seebeck coefficient cross sections across the bicrystalline gold nanowires. Annealed bicrystalline gold nanowires are also measured as well as unannealed bicrystalline gold nanowires. Annealed devices were annealed at 400 degree C for 1 h prior to measurement. Previous analyses suggest that annealing reduces the internal distortions [137].

The IGM data show a small degree of change in misorientation around the grain boundary, whereas the PTE photovoltage remains relatively low in signal, showing that individual abrupt grain boundaries do not behave detectably as thermocouples relative to the long-range misorientation. Finite-element simulations detail the change of S required to observe the PTE voltages observed in experiment (Fig. 5.10), which implies that different grain orientations must have S values that differ by less than 0.013% (0.0002 μV/K) over 500 nm. Although the PTE response due to grain boundaries is negligible, the measurement is sensitive to long-range misorientation changes on either side of the boundary. These observations imply

that the spatially varying S(x) responsible for the complex PTE maps seen in polycrystalline wires [21] arises from a complex combination of geometry, strain, and dislocation formation, rather than the grain boundaries themselves. Note that an abrupt change in Seebeck coefficient would manifest itself as a peak in the PTE voltage as a function of laser position (Fig. 5.5), as expected for a simple thermocouple heated at the junction between dissimilar materials. An inclusion of a small (relative to spot size) region of different *S* than the surrounding material creates back-to-back thermocouples, leading to an antisymmetric PTE feature as a function of laser position (Fig.5.6).

Unannealed bicrystals typically have larger PTE responses than annealed devices. Fig. 5.10 *A*–*B* and *C*–*D* compare the PTE voltage profiles of unannealed and annealed devices, respectively. The annealed devices were annealed at 400 °C for 1 h prior to measurement, as mentioned previously. The profiles of the unannealed devices have on average, greater spatial variation and signal magnitude than those of the annealed devices. Based on Seebeck map obtained from simulations, the unannealed bicrystal devices have an average signal of 0.026+-0.006 μV/mW and annealed devices have an average signal of 0.0096+-0.0003 μV/mW. On average, unannealed bicrystals have a 2.7 times larger signal than the annealed ones, demonstrating that defect annihilation and strain relaxation during annealing can contribute considerably to the local S. We note that annealing at 400 °C does not modify the crystalline character sufficiently to produce large detectable changes in the IGM maps. Previous analyses suggest that during annealing, dislocations rearrange and coalesce to form stable arrays that reduce the dislocation density

over long ranges [137], which could be the source of lower PTE magnitudes. This implies that the PTE response arises from a combination of crystallographic defects, only some of which manifest themselves in the IGM signal.

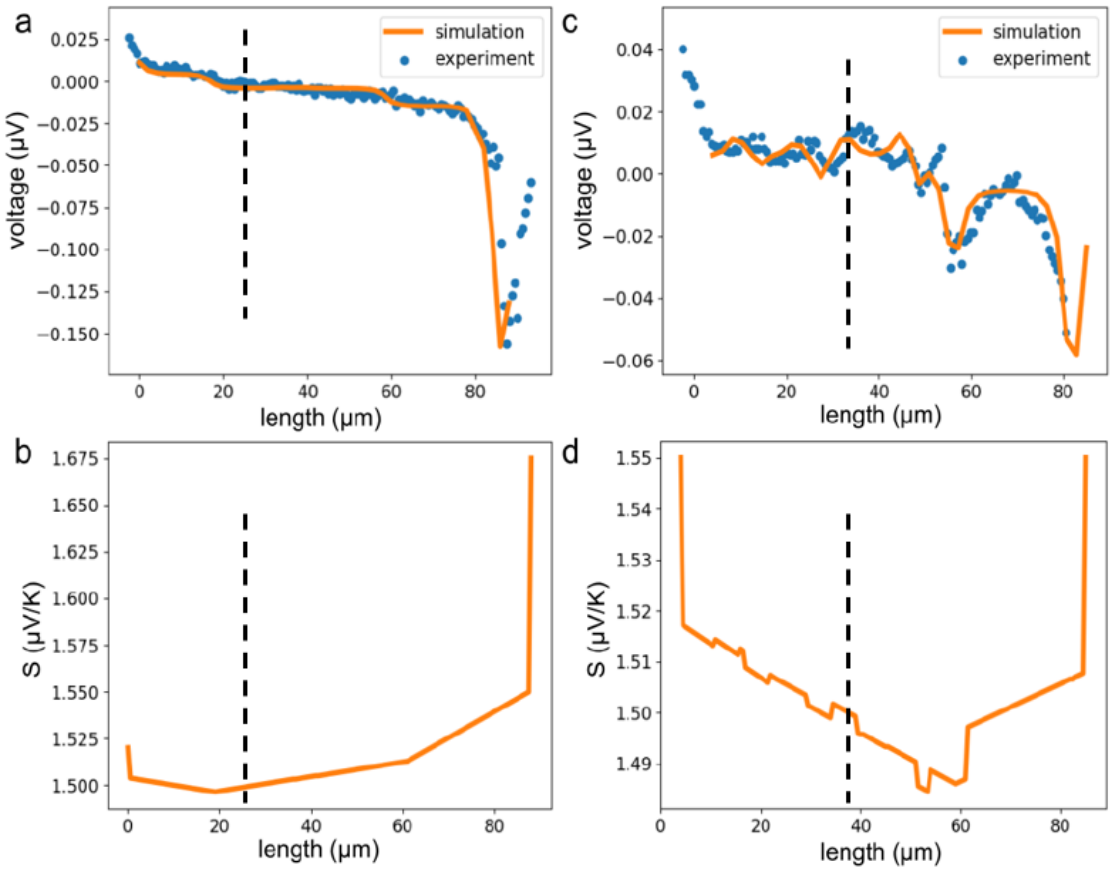

Figure 5.10. Open circuit voltage plot and b, d corresponding Seebeck coefficient plot of the annealed and unannealed bicrystal devices seen. Dash

lines show the location of the single grain boundary. As shown, grain boudary effect in PTE signal is not more important than internal strain.

5.3.3. Resolution of these measurements

Assuming good thermal contact to the substrate. The spatial resolution is limited by the laser spot size, which is ~1.8 μm with the assumption of proper thermal conductivity to the substrate.

The spatial variation of the PTE voltages in this experiment and in previous works were on the order of and smaller than the laser spot size [21], [22]. To determine the resolution of the experiment, a geometry shown in Fig. 5.11a consisting of a stripe of varying length *d* between two long wires was used in simulations. 3 nm long defects are placed on either side of that variable length stripe and assigned their own Seebeck coefficient compared to the bulk value assigned to the long wires and the variable length stripe. Fig. 5.11b shows the corresponding open circuit voltages as the length *d* varies. For a laser spot size of 1.9 μm FWHM, the smallest length for *d* with distinguishable signal is 1.8 μm which is smaller than the spot size. This resolution depends not only on the laser spot size but also the thermal conductivity of the device. Although the thermal conductivity can change the overall response of the open circuit photovoltages observed in experiment, we argue that the main contributor to these photovoltages is the variation of the local Seebeck effect and not variations in the thermal conductivity. In order to observe variations of the open circuit photovoltages within the laser spot size as observed in

experiment due to changes in thermal conductivity, it would require nontrivial spatial variation of the thermal path along the wire. Although large changes in the thermal path have been observed in nanoscale devices [135], this observation would be very unlikely in steady-state illumination of single-crystal nanowires under relatively large laser spot sizes.

The measurement resolution clearly also depends on the steps size in PTE measurement. Here because PTE measurement step size is much smaller than the laser spot size (0.5 μm vs 1.8 μm), the measurement resolution is not limited by the step size.

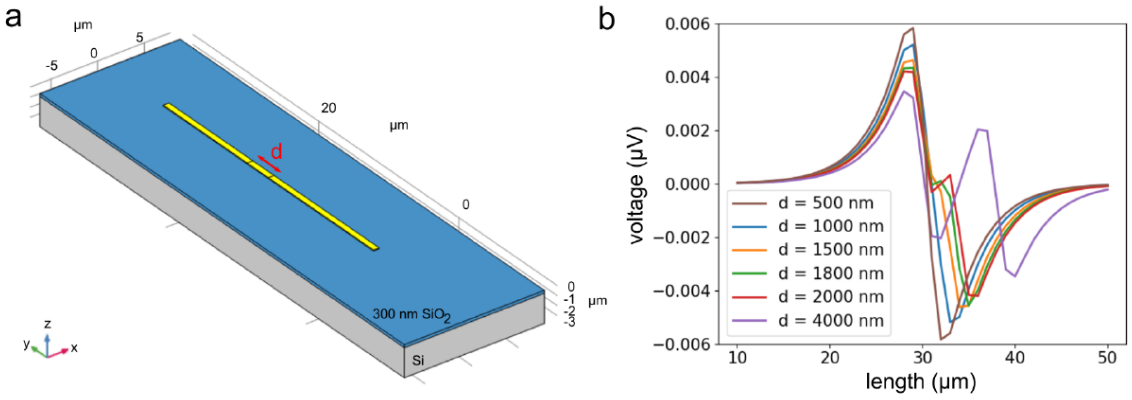

Figure 5.11. Simulation of the experimental resolution. a: A stripe with variable length d is placed between two long wires, all assigned S of bulk gold. On either side of the stripe are 3 nm long defects assigned their own S. b: Corresponding open circuit voltages as a function of heater position with 1.9 μm of devices with various lengths of d. The open circuit voltage has a

detectable peak when the two defects are 1.8 μm apart which is smaller than the heater spot size.

5.3.4. Impurity detection

These single crystalline gold nanowires have Pt seeds on one end. During fabricating single crystalline gold nanowires, when the temperature reaches ~1080 degrees C, shown in Fig. 5.2 Pt diffuses from the solid seed region into the encapsulated liquid gold. As the structure cools from melt, the Pt concentration decreases away from the seed resulting in Pt concentration gradient. Gold bicrystal wires with single grain boundary are seeded symmetrically by two Pt seeds one at each end of the wire. Bicrystal devices studied in this section are close to the Pt seeds. The bicrystalline gold nanowires presented in previous section (internal strain) are 200 μm of microns away from the Pt seeds so the Pt impurity eliminated based on Pt diffusion model [103]. The amplitude of PTE signal caused by Pt impurity in gold crystalline nanowires are ~100 times larger than the PTE signal caused by internal strain and crystal misorientation presented in previous section. Pt gradient plays a key role in single crystal growth, and in bicrystals, it forces the grain boundary to form at the center of each wire regardless of the crystal orientation of adjacent grains. Secondary ion mass spectrometry (SIMS) is a common doping measurement technique that generally offers the highest sensitivity for detecting impurity. However, this method lacks the sensitivity to accurately and quantitatively reflect the entire Pt impurity in Au nanowires. One reason is due to the fact that Pt and Au stable inotropes have similar mass and secondly [103].

Through finite element modeling, the spatially varying S is inferred and demonstrates that a variation of Pt concentration as little as 0.01% per μm can be detected with PTE measurement. At room temperature 0.5% Pt impurity can change the sign of S in gold nanowires from positive to negative, as the impurity changes the energy dependent scattering pattern, which affects both the photonic and electronic contributions to S. [6], [138]

PTE signals across these bicrystalline gold nanowires are shown in Fig5.12, 5.13. Each of these figures correspond to a separate fabrication run. The overall shape of PTE signal on each chip is the same, and there is chip to chip variation. The reason is that the Pt diffusion is extremely sensitive to the maximum temperature. Fig 5.12 correspond to 1080 ℃ and Fig. 5.13 corresponds to 1063 ℃.

The structures were heated at Stanford in a rapid thermal annealer (RTA) system, which lacks precise control at high temperatures. As seen in the phase diagram, changing the peak annealing temperature by a few degrees can significantly change the initial platinum composition. To demonstrate this effect, we estimate the platinum concentration from the simulated S profiles using literature values and fit a Scheil-Gulliver profile to the data (Fig. 5.16), which shows that even a 6℃ variance from the desired maximum annealing temperature could account for the difference in PTE response.

When the laser is incident on the grain boundary, which defines the device's geometric axis of symmetry, the PTE voltage is near zero. On either side of the grain boundary, the voltage is of opposite polarity and varies approximately linearly over

30 μm, over 15 times larger than the focused laser spot FWHM. The largest signal magnitude occurs close to the electrodes approximately 15 μm on either side of the grain boundary. Simulations suggests that a 1.8 μm FWHM focused beam diameter results in a temperature rise of ~2 K and should not appreciably heat the grain boundary at a distance greater than 10 μm around the boundary (Fig. 5.15), which indicates that the maximum signal is neither set by the grain boundary itself nor the laser spot size. Seebeck coefficient map extracted from these PTE signals show a gradient of S that varies approximately linearly at a rate of 0.22μV/K per μm. Previous experiments have shown that alloying gold with increasing Pt concentration from 0.11% to 0.5% can change S by approximately 1.6 μV/K [139], [140]. Based on these literatures, simulation results suggest that variations in Pt concentration of ~0.01% per μm have detectable impact on S and can lead to the measurable PTE signal. Though we cannot obtain the absolute S through these simulations, we can use the simulated S values to estimate the potential Pt concentration gradient in the structures using literature values.

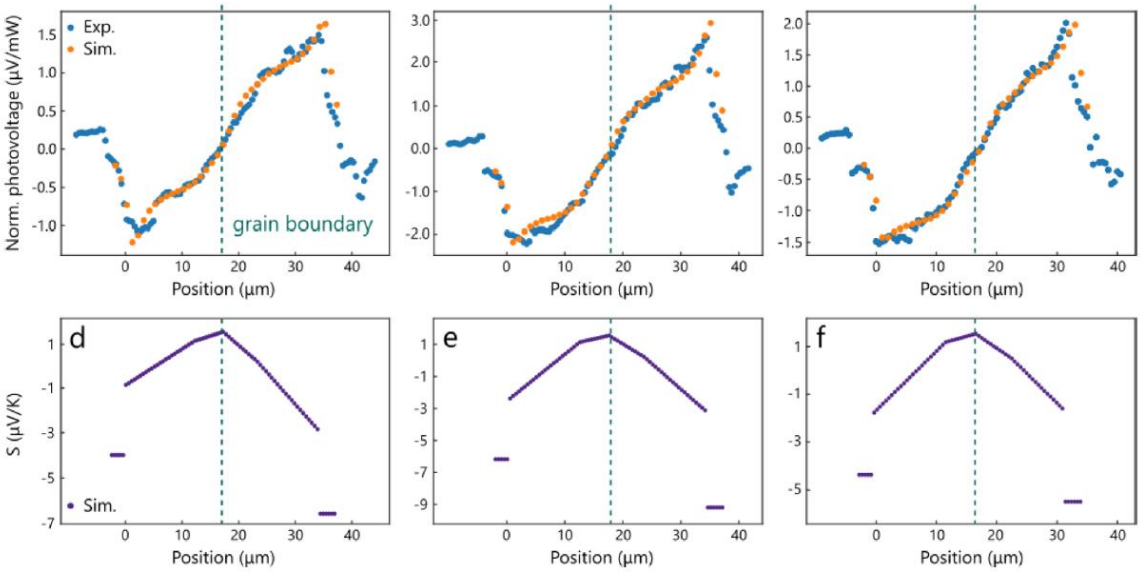

Figure 5.12- simualtion fit to the first chip.

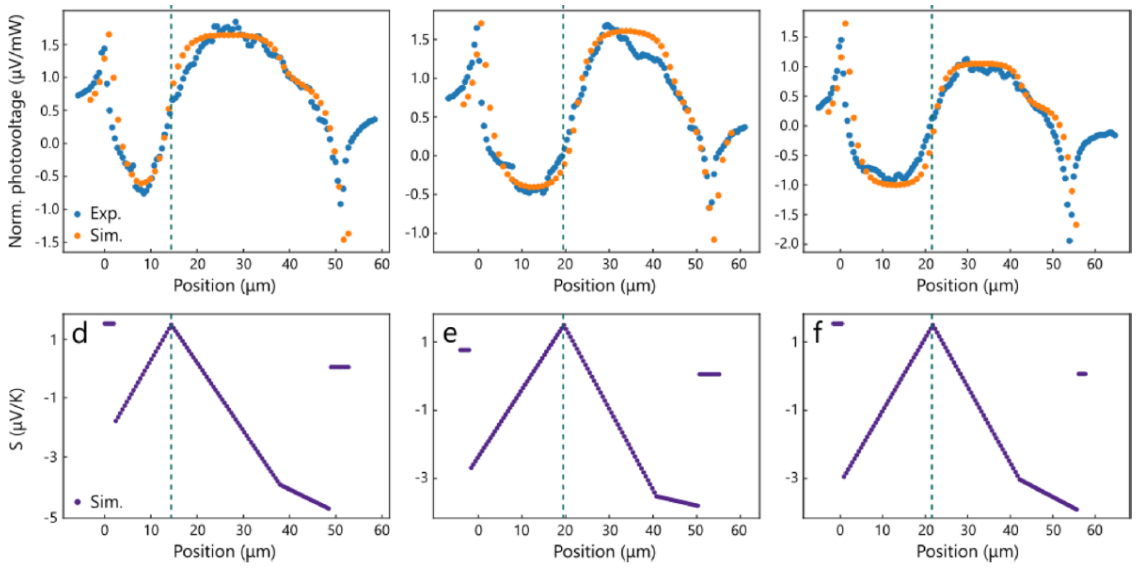

Figure 5.13. Simulation fit to PTE experiemtal on chip 2

Note the difference in Seebeck map of the nanowire to the pads in chip 1 and 2. By comparing the Seebeck map across the device in Fig. 5.12 vs 5.13 we see that the relative Seebeck coefficient change at the pads for these two chips are different. In chip 1 (Fig. 5.12), the Seebeck coefficients of the pads are smaller than the Seebeck coefficient of the nanowire in other words, they follow the same trend of Seebeck coefficient change across the nanowire. For that reason, even though the signal drastically changes at the pads, but the polarity doesn't change before the nanowire and pad interface vs in chip 2 (Fig. 5.13), the Seebeck coefficients of the pads are larger than the Seebeck coefficient of the nanowire; they do not follow the same trend on Seebeck change across the nanowire, so, sign flip of open circuit voltage happens before the pads. This difference can change the polarity of the signal before the pads but the extracted Seebeck map across the nanowire is still extractable. In Fig. 5.14, the *dS* across the nanowire in one device from chip 1 and one device from chip 2 is forced to 0 but the pads have the same Seebeck coefficient. It is obvious that without *dS* across the nanowire, we cannot reproduce the PTE map across the devices.

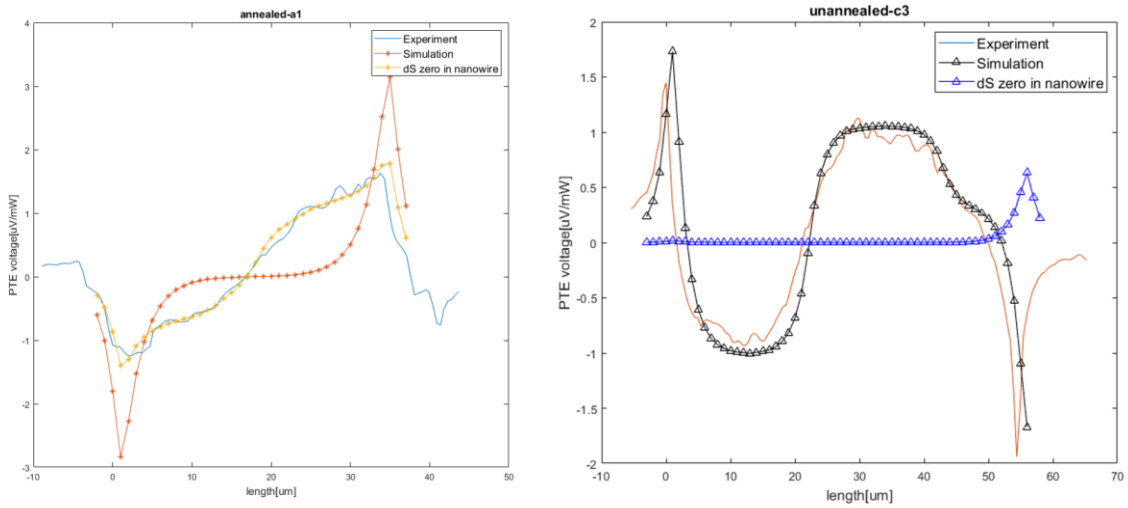

Figure 5.14. right: PTE voltages of experimental values (solid line) and simulated data based on the spatial distribution of S on the left (black triangles). The blue triangle data shows the simulated PTE signal with no variation of S along the length of the wire.

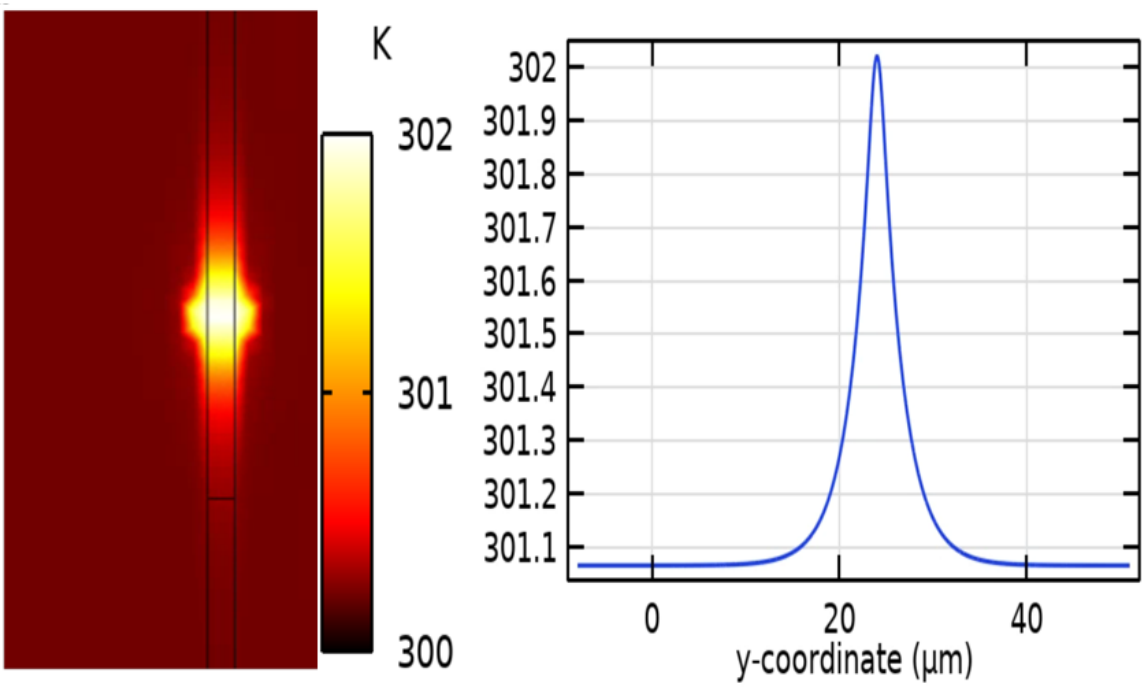

Figure 5.15. a) Surface temperature map of the device under laser illumination. b) Zoomedin surface temperature map of the device centered around the illuminated portion. c) Plot of the temperature distribution along the length of the wire. The FWHM of the temperature distribution is ~10 µm, much smaller than the length of the wire and the maximum temperature rise due to the illumination is 2 K.

Match of Pt distribution from simulation results and Pt diffusion model based on Scheil-Gulliver are shown in Fig. 5.16. The dotted plots are Pt diffusion extracted from Seebeck map simulated in COMSOL and solid blue line correspond to Scheil-Gulliver Pt diffusion model. Fig. 5.16 a and b correspond to two different chip

fabrication that the Au-Pt alloy is heated up to two different temperatures; 1074 ℃ and 1086 ℃, respectively.

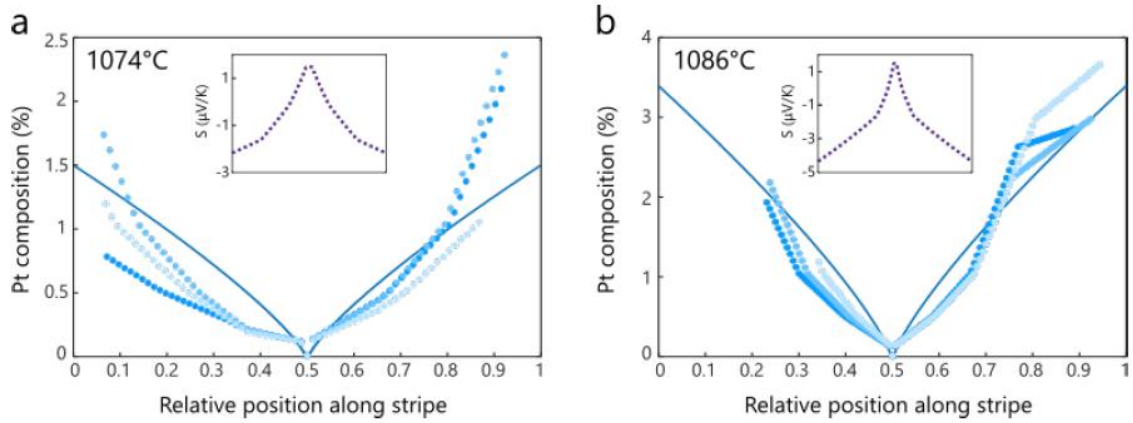

Figure 5.16. a) Using literature [139] values, we estimate the platinum concentration in each of the three 40 μm long bicrystals (blue data points) from the simulated Seebeck coffcient distributions in Fig. 5.12a-c. Fitting a Scheil-Gulliver profile to the data (blue solid line) shows that a 1074℃ maximum annealing temperature could account for the PTE response. b) We estimate the platinum concentration in each of the three 80 μm long bicrystals (blue data points) from the simulated Seebeck coeffcient distributions in Fig. 5.13a-c. Fitting a Scheil-Gulliver profile to the data (blue solid line) shows that a 1086℃ maximum annealing temperature could account for the PTE response. The insets show the Seebeck coeffcient profiles that correspond to the Scheil-Gulliver models.

By scanning a heat source across the structure and measuring open circuit voltage at each point, Seebeck coefficient variation across the device can be mapped. The spatial resolution is limited by the laser spot size, which is ~1.8 μm with the assumption of proper thermal conductivity to the substrate. Characterizing the different factors that affect the Seebeck coefficient is crucial to understand nanostructured thermoelectric materials. This knowledge can be used for probing

intrinsic characteristics of the nanostructures using opto-electrical measurement. Further this knowledge can be used to properly design a thermoelectric system.

While structural defects can dominate the PTE signal (geometry change), we've proven through the experiments and simulations that the crystallographic misorientation and internal strain cause detectable Seebeck change across the device. The order of Seebeck change obtained from simulation matches well with previous studies. Crystal misorientation as well as internal strain change the Seebeck coefficient. The analogous measurements performed on bicrystal gold structures reveal that abrupt higher-angle grain boundaries do not noticeably affect $S(x)$. Annealed bicrystal devices show that the overall photovoltage response associated with misorientation is reduced by a factor of 2.7, again highlighting those changes in dislocation density and strain affect local thermoelectric response. PTE voltages can also serve as a sensitive probe of inhomogeneous platinum impurities in gold, which otherwise cannot be detected using more conventional compositional analysis techniques like SIMS.

Chapter 6

Directionality of hot carrier tunneling in Au-Pt and pure Au MIM structures

6.1. Motivation

Electron tunneling is important in nanometer size circuit design as it causes unwanted current through the nm sized barriers where tunneling probability is high. [141] Tunneling is beneficial in areas like scanning tunneling microscope (STM)[142], 2D based devices [143], spectroscopy of electronic excitation [144], and plasmon resonators [145], [146]. Beyond pure tunneling, ever since the photoelectric effect was first observed by Heinrich Hertz in 1887 [147], the photoemission has been utilized in different structures. Photoemission in semiconductor-based devices can be strongly affected by the semiconductor bandgap. Metal-based photoemissive devices can potentially work over a wide spectrum. Assuming a uniform density of states [148] the hot electrons generated in

metals by photons can range from zero to a maximum of the photon energy above the Fermi level.

In Chapter 2 it was stated that the plasmon modes can decay nonradiatively through Landau damping [35], [66], [149], in which each plasmon quantum produces one electron-hole pair. When the energies of these carriers are larger than thermal excitations at ambient temperature, these carriers are called 'hot carriers' [35]. Electrons are generally excited from the conduction band to higher energy states in the same band, also known as an intraband transition. The excitation can also take place between the conduction band and other bands (e.g., *d* bands) in a process known as interband excitation. The energy levels of *d* bands are substantially (~3 eV) lower than the conduction band energy level for metals such as Au, making the interband excitation far less likely than intraband excitation [148], [150]. The ratio of electron to hole generation depends on the electronic structure and photon energy. Hot carriers can be used in local heating [55], [151], photochemistry [45], [152], photo-desorption where the energy of hot electrons can be used to photo-desorb small molecules form the surface[153]. Hot carriers can be photoemitted from a metal over either a Schottky [29], [154] or oxide tunnel-barrier [155], [156].

In this Chapter hot carrier tunneling is introduced in a MIM junction with dissimilar metals with different plasmonic behaviors in a planar design. These planar designs require less space, have lower weight, and are easier to fabricate compared to stacked MIM designs. In stacked MIM structures, the thickness of the

layers should be designed properly for optimal efficiency [71], [79], [80]. In our devices, the polarity of the open circuit voltage caused by tunneling of these hot carriers is consistent with hot electron tunneling direction based on hot carrier generation from plasmon decay. In these structures it is possible to apply added bias across the junction [71]. However, biased devices need more complicated design, and the bias is potentially a new source of noise to the system. In previous studies where the similar metals were used in planar MIM junctions, the polarity of the open circuit photovoltage was not controllable with direct optical excitation [22] (Fig. 6.2) or with indirectly exciting localized plasmon modes in the gap by SPPs excited from the gratings [23]. Planar MIM tunnel junctions presented here have higher stability even at ambient conditions comparing to previous planar MIM tunnel junctions operating in vacuum [22], [23]. The structures presented here can in principle be used to make photodetectors that are faster and have higher responsivity comparing to PTE based PDs presented in Chapter 4 that require the time scale of electron-phonon and phonon-phonon interactions to operate in steady state [4].

In stacked MIM designs, two plasmon modes can contribute to the signal: one mode is the optical field intensity confined between metal layers and the other one is the propagating mode at the metal-air interface. Plasmon nanoparticles at the top of the stack can increase the localized absorption and the SPPs at the MI interface [79], [157], [158]. Both modes contribute to the hot carrier generation due to plasmon decay. Several studies have shown that the surface plasmon excitation increase the efficiency in MIM structures [79], [159], [160].

In gold nanowires multipolar plasmon modes can couple with dipolar plasmon modes due to breaking of the symmetry through fabricating a nanogap, as shown in Fig. 6.1. In Fig. 6.1 is shown that the nanogap in metallic nanowires can be made either through self-aligned method [89] or by electromigration [82]. In both cases the there's a huge enhancement in SERS signal especially when applying light with polarization perpendicular to the width of the nanowire. That's because of exciting dark plasmon modes that now are coupled to a dipolar mode due to hybridization effect [9] after breaking the symmetry as explained in Chapter 2.

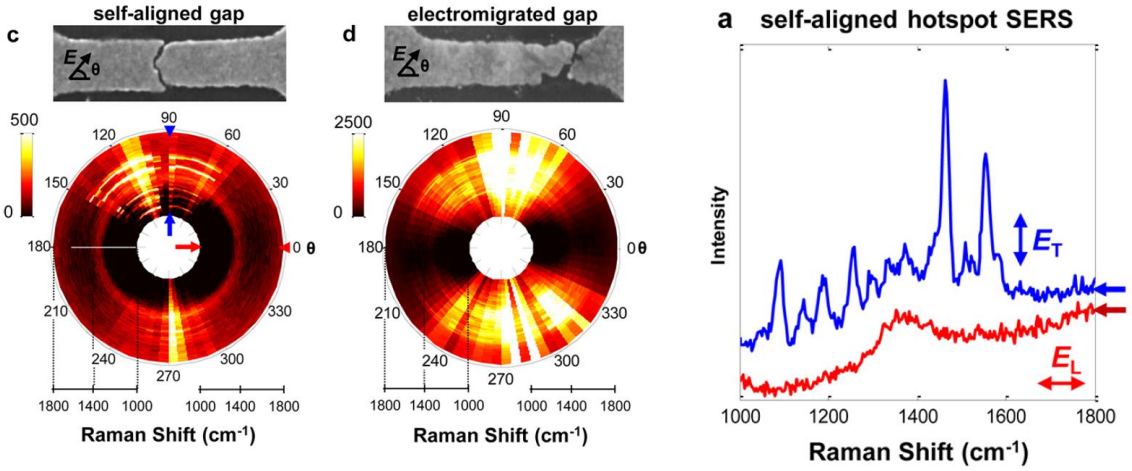

Figure 6.1. multipolar modes can be generated by breaking the symmetry in gold nanowires and increaes the SERS signal.[10]

In Fig. 6.2 the photovoltage map of a pure gold bowtie structure before and after electromigration is shown from Ref [22]. After electromigration, the maximum signal is localized where the gap is, and the amplitude is 1000 times larger than the

unmigrated gap PTE signal due to hot carrier tunneling. However, the polarity of this hot carrier tunneling changes from pixel to pixel and from device to device or even from scan to scan.

In devices presented in this chapter we introduce MIM planar junctions with Au and Pt electrodes and we argue that due to hot carrier generation in Au electrode, the hot carriers tend to tunnel from Au electrode to Pt and so the direction of hot carrier tunneling can be controlled.

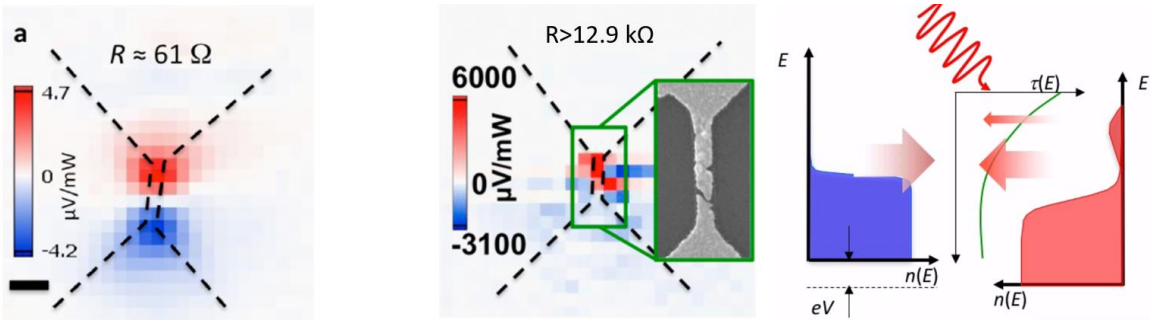

Figure 6.2. after gap the signal is stronger but polarity is not controlable. Three main difference in before and after photovoltage (PV) maps: 1-the maximum signal happens localized at where the gap is formed and no longer at the two ends of the nanowire. 2- the amplitude is enhanced by ~1000 times due to electron tunnling (the response time is also modified but not clear from our steady state measurements). 3-the polarity of the signal from pixel to pixel and not reproducable in a single device as the tunnlieng depends on nanoscale geometry details of the tunnel junciton. Figure used with permission [22]

6.2. Theory and background

Efficiency of MIM photo tunneling current is smaller than 1% [161]. Plasmons have been used to increased the efficiency [79]–[81]. Photoemission

process in these structures happen in three steps similar to previous references[29], [71], [162]–[164]. First, each absorbed photon creates an electron-hole pair. This first step is not efficient for metals as they reflect most of the incoming photons. Exciting LSP modes can enhance the effective area in which metallic nanostructures can absorb photons from (as discussed in Chapter 2). Second, the hot carriers move forward to the metal insulator interface, and third, a portion of these hot carriers can tunnel through the thin layer of insulator to the other electrode (proportional to the transparency coefficient introduced in Chapter 2). In the second step, usually only small number of hot carriers make it to the interface without undergoing inelastic collisions, and this fraction depends on the mean free path of the electrons, which in turn depends on the metal type and the total energy of the hot electron [165]–[167]; for gold at 1.16 eV is ~ 50nm [116], [168], [169]. In the structures presented here, due to the asymmetric nanometer sized gap between the two metallic electrodes, the field enhancement due to multipolar and dipolar plasmon modes is very focused in the gap. So, the hot carriers made from nonradiative decay of plasmons are similarly concentrated near the nanogap (~1nm). This increases the probability of the hot carriers reaching the metal-insulator junction compared to hetero MIM systems (second step). Previous studies have shown that adding an antenna near the MIM interface can increase the photoresponse of the junction. [29], [170], [171]. The hot carrier emission probability (third step) can be subdivided into two steps: first, the probability of the hot carriers to tunnel through the first MI interface and not to be reflected. This depends on the momentum conservation applied at the interface [81]. The roughness of the structure at the interface can help

with relaxing this condition. [172] And second is the probability of this hot carriers to get to the second metallic electrode. This probability decreases exponentially with the thickness of the gap. In our measurement, during the electromigration process, if the resistance of the device is larger than tens of MΩ, the measured photovoltage reduces to almost zero due to the comparatively large gap size between the two electrodes. Note that if the hot carriers have larger energy than the barrier height, the probability in the third step (second part) will be almost 1 and the process will be internal photoemission (introduced in Chapter 2) even though only a small fraction of photoexcited hot electrons make it out of the metal due to very fast carrier energy relaxation processes.

In our planar MIM structures, because the work functions of metals are larger than their LSPR energies, hot electrons with energies of incoming photons cannot escape into vacuum [35]. The hot electrons generated from plasmon decay can form a Fermi-Dirac distribution (shown in Chapter2, Fig. 2.9) in the time scale of electron-electron scattering processes such as Auger transitions [173]. A portion of these hot carriers tunnel to the other electrode, and those that weren't able to tunnel through the barrier to the other side will interact with phonons and heat the lattice and other electrons [174]. Our devices operate in the ohmic regime, but we utilized plasmons in our design to control the directionality of hot carrier tunneling. Au is plasmonically active in the near infrared range. In heterosystems Au is commonly preferred as the absorber layer for its optical properties and long mean free of hot electrons [29], [165].

For modeling the hot carrier generation and tunneling different models have been developed. Landauer theory has been used to define the photocurrent across the nanogap using the transmission function of a single conductor resonance. [22], [175] In Schottky barriers hot carrier current has been modeled by plasmonic absorption spectrum and the transmission probability of the junction for internal photoemission [29], [144]. The three steps model explained previously can also be used to model photocurrent generated in MIM structures. [71]

6.3. Experimental details

We make tunnel junction in metallic nanowires using electromigration. In electromigration method, the applied electrons (through applying a bias) interact with the stationary ions in the wire. These charge carriers can physically move the ions around. The process can be continued until a nanogap is formed. we apply cycles of voltage to gradually break the junction. We use a Keithley 2400 sourcemeter to apply voltage and to measure the resistance of the device simultaneously. One end of the device is connected to the Keithley and the other end is grounded. To form the nanogap between Au and Pt, the wiring configuration during electromigration is important. The gold side of the device should be grounded and the Pt side of the device should be connected to the Keithley, otherwise the gap will be formed at the other end of the gold nanowire. Note that the Pt has a higher melting point than Au, so during electromigration, only the gold nanowire is electromigrated and Pt nanowire remains apparently unchanged. For breaking these structures, several methods have been used. The electromigration

method that breaks the devices with high yield is as follows. For Au-Pt devices first the maximum applied voltage is set between 2-2.5 volts and the threshold to stop the cycle is 0.1% change in the resistance. If the device resistance change doesn't reach 0.1% with the maximum applied voltage, the maximum applied voltage is increased by 0.1 V for the next cycle. If the device could increase its resistance by 0.1%, we let the cycle to repeat itself until the 0.1% current decrease happens at a voltage smaller than 0.7V. Then, the 0.1% is increased to 0.25%. The threshold of the current drop increases gradually to ~20% (different between devices) while keeping the maximum applied voltage smaller than 0.7V. We continue this process until the junction breaks (usually ~1-2.5 hours). Breaking the junction here means to decrease the conductance of the device to be smaller than conductance quantum, G_0. When the conductance of the devices is equal to the conductance quantum (R_0 ~12.9kΩ) it means that the wire most likely has only one transmission channel. And when the resistance of the device is larger than R_0 it means we have created a MIM tunnel junction. Based on fitting to the Simmons model, the nanogap formed in devices presented here is ~1nm. [75]

Equation 6.1. Quantum conductance G_0

$$G_0 = \frac{2e^2}{h}$$

Pure gold devices are more likely to blow up (resistance larger than tens of MΩ) during electromigration. When devices suddenly blow up, the formed gap get so large that the hot carriers generated on one electrode attenuate before getting to

the other electrode, so the open circuit voltage is mostly dominated by the noise of the system. The conductance decays as the gap gets larger with formula below:

Equation 6.2. Conductance of a gap with thickness of d

$$G = G_0 e^{-\beta(d-d_0)}$$

Where β is the attenuation factor (for gold ~18.5 nm^{-1}), d is the gap distance, and d_0 is the lattice constant (for gold ~0.4nm). [176]

For both before and after electromigration photoelectric measurements, we measure the open circuit voltage instead of short circuit current to avoid any possible changes to our device structure caused by short circuit current. In the opto-electrical measurement setup at ambient conditions, a 1060nm CW laser is used as the optical source. The laser is chopped via a chopper with its frequency as the reference for the lock in amplifier frequency. The laser hits the devices in open air and the open circuit voltage of the device is amplified through a low noise preamplifier and then measured via the lock in amplifier. In the opto-electrical measurement setup under vacuum, a 785 nm CW laser is used as the optical source. The devices are under high vacuum and at room temperature. Optimal widths of the gold nanowires for dipolar mode excitation at 785nm and 1060nm incident wavelengths are found based on finite element simulations [4]. The measured open circuit voltage is normalized to the optical power, as both PTE signal and the hot carrier tunneling current are observed to change linearly with applied incident power [22], [71]. At very high optical local powers, optical forces and tunneling

electrons can change the nanometer sized structure at the nanogap, so the optical power after electromigration is reduce to ~0.5 [mW]. Movement of the atoms around to change the gap structure at the nanometer scale can change the plasmonic behavior and measured open circuit voltage. If the electrodes connect at the atomic scale, the plasmon mode energy and the photovoltage decrease. [177], [178]

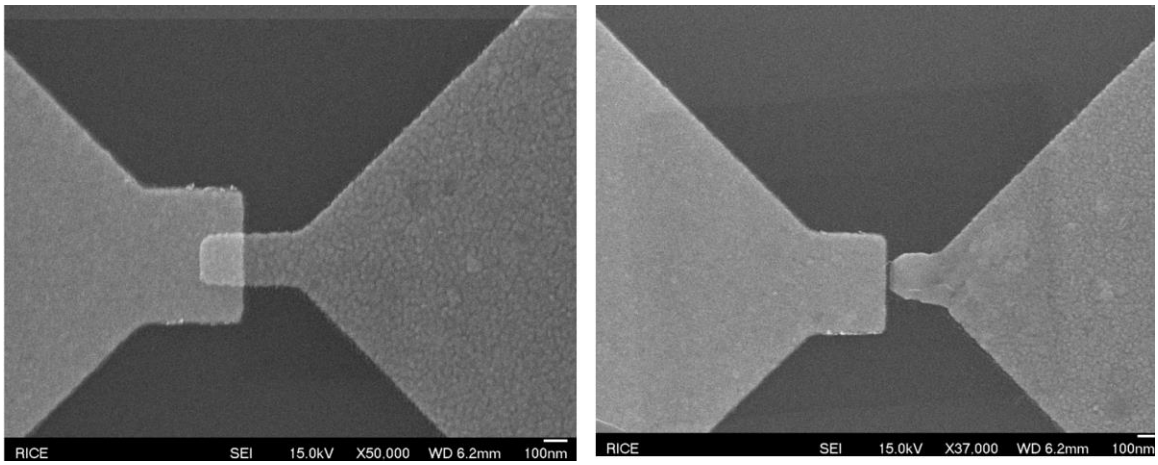

Figure 6.3. Au Pt MIM junction before and after electromigration. A clean gap between Au and Pt is formed after electromigration

6.4. Directionality of hot carrier tunneling in Au-Pt MIM structures

Before electromigration, the photovoltage signal in Au-Pt devices is due to the Seebeck effect and the thermocouple formed by the Au-Pt junction. After electromigration to form a complete nanogap, the photovoltage is dominated by hot carrier tunneling. After electromigration the size of the gap (1 nm) in our planar Au-air-Pt MIM structure is much smaller than the laser spot size(~2 μm). Due to

hybridization of modes in the nanogap, a localized field enhancement is formed in the nanogap. Because Au electrode is more plasmonically active than Pt at the incident photon energy, the hot carriers are preferentially generated in Au electrode and they tunnel to the Pt electrode. In Fig 4.6 the polarity of the signal before and after electromigration is compared. Before electromigration (Fig 4.6a) the PTE signal should be negative based on Seebeck map and the electrical wiring. After electromigration (Fig 4.6b) if the hot carriers are generated in Au nanowire and they tunnel to the Pt side, the open circuit voltage that system builds to counteract the hot carrier tunneling should be negative with the same electrical wiring. So, before and after electromigration the polarity of the signal should remain unchanged, but the amplitude of the signal should get stronger after electromigration due to hot carrier tunneling. Fig 4.7 shows the photovoltage map measurement results of a particular device. As it is shown, before electromigration, the PTE signal follows the transverse dipolar plasmon mode of the gold nanowire. After electromigration, as expected, the polarity of the signal is the same as before electromigration but the amplitude is ~100 times stronger. The polarization of the signal follows the dipolar plasmon mode of the nanowire but due to localized hybridized modes in the nanogap, the polarization dependency gets stronger. Note that the gap gets unstable under constant illumination that is why the polar plots after electromigration is not perfectly symmetrical.

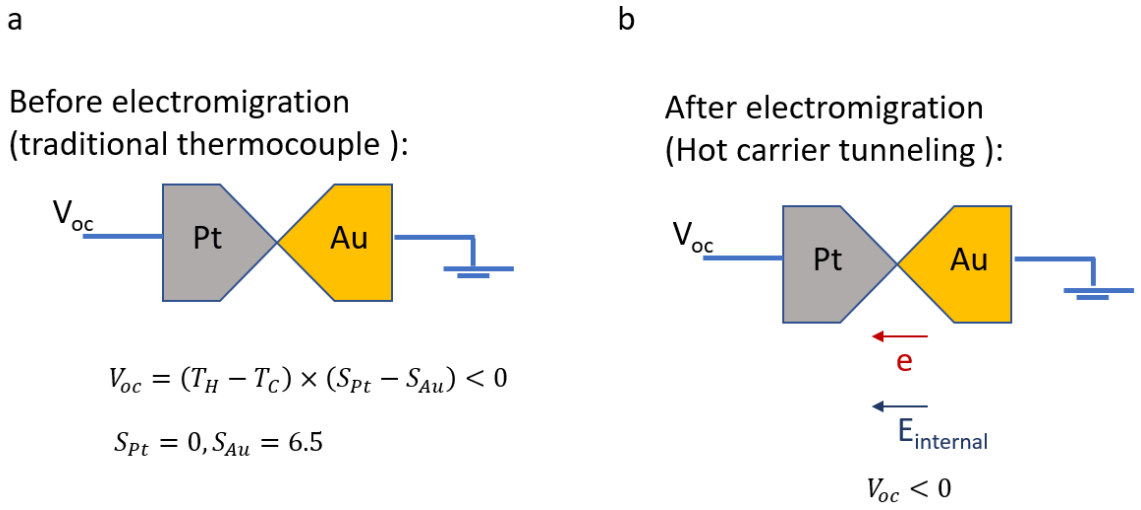

Figure 6.4. Before and after electromigration the polarity of open circuit voltage should be the same. a) before electromigration the signal is dominated by PTE. b) after electromigration the signal is dominated by hot carrier tunneling.

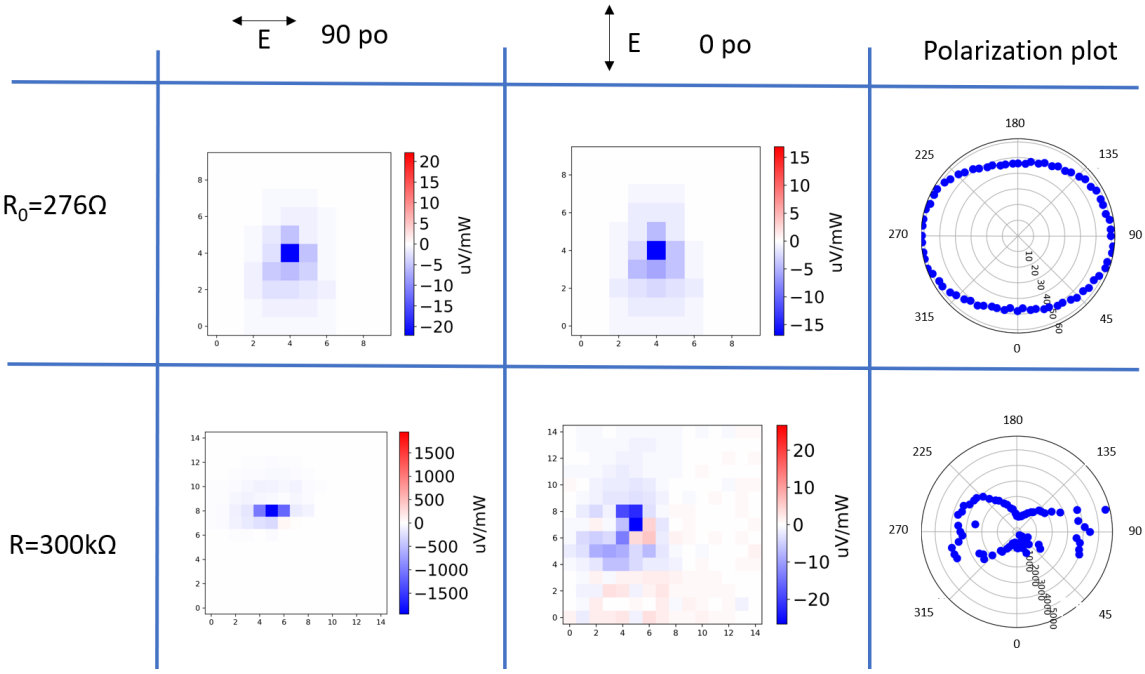

Figure 6.5. An experimental measuremnt example of a Au-Pt junction. The sign of the photovoltage before and after electromigration is the same, consistent

with expectations. The amplitude is much stronger after electromigration due to hot carrier tunneling. The signal for perpendicular light polarization is dominant before and after electromigration, consistent with transverse LSPs in the gold wires playing the key role in both heating (before migration) and hot carrier generation (post-migration).

To prove the plasmonic origin of the photovoltage after electromigration, two different widths of Au nanowires are made for Au-Pt devices, to test for transverse plasmon resonances. The results are shown in Fig. 6.5. When the width of the gold nanowire is closer to the dipolar plasmon peak (red triangles), the generated photovoltage is stronger. The best width for the Au nanowire to have a transverse mode resonant at 1060nm is ~300nm but the electromigration of such wide nanowire can be tricky and the nanogap might not be formed at between Au and Pt. In Au-Pt devices shown in blue circles in Fig. 6.5, where the width of the nanowire is farther away from the dipolar resonance, after electromigration, ~20% of the devices have shown a dominant signal at the polarization along the nanowire (perpendicular to the transverse dipole mode) versus all the Au-Pt devices with widths closer to the transverse dipole mode (red triangles) show much stronger signal at incident transverse polarization of light. This is another observation that confirms the plasmonic source of the photovoltage. Fig 6.6 also shows that remains of Au nanowire on the Pt after electromigration does not dominant the photovoltage signal.

In our devices, even though the built-in electric field caused by the work function difference in the asymmetric MIM structure should tend to favor electrons going from Pt to the Au electrode [71], the hot carriers are generated in Au side and

cause an asymmetric electron distribution across the MIM structure (similar diagram as reverse bias diagram shown in Fig. 2.12) so the net tunneling current is dominated from Au to Pt. The directional effect by the built-in electric field in the insulator in MIM structures is dominant when the mean free path of e-ph scattering in the insulator is smaller than the insulator thickness [71], which is not true for our devices where the gap is vacuum or air and the gap size is smaller than 1nm.

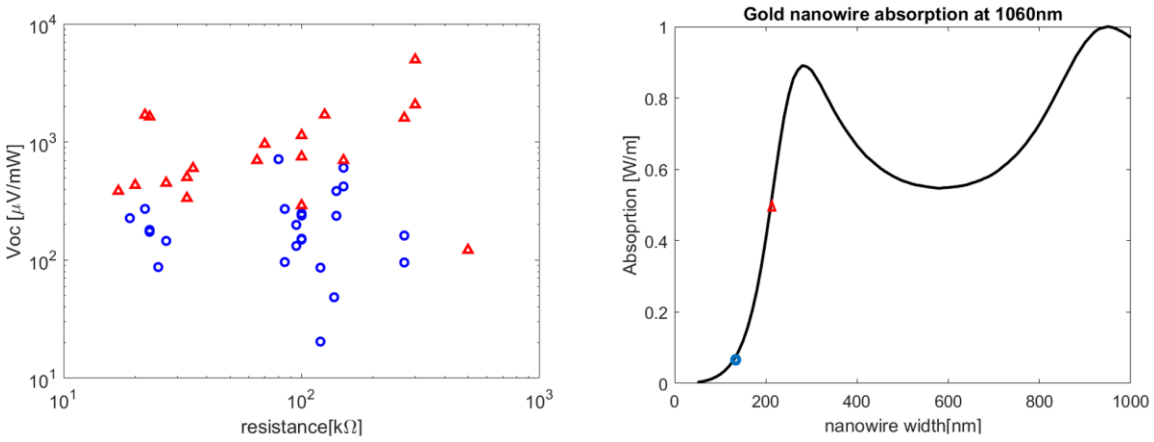

Figure 6.6. Red and blue dots show open circuit voltage of the Au-Pt devices with ~230nm and 160nm width for the gold nanowire respectively. The red signal are higher than blue signals. This supports the role of plasmons in the behavior of these junctions.

The asymmetric tunneling barrier is formed by difference between work function between Au and Pt. Because the energy of hot carriers are smaller than the works function of either side, our MIM devices are operating in ohmic region. Increasing the difference in the work function can increase the probability of tunneling as it may decrease the effective thickness of the barrier for hot carriers (Similar to Fig. 2.10b). Neither Au nor Pt oxidize in ambient conditions and are

therefore good options for this design. By choosing other metals instead of Pt, either the metal oxidizes (Au-Mo in Appendix) or it formed an alloy with Au (Au-Pd in Appendix). Other than stability of Au and Pt, in our wavelength Au is plasmonically active vs Pt which is not. So, the carriers are generated preferentially on the Au side; the energy distribution looks like a reversed bias applied to the structure (Fig. 2.12a). The hot carriers tunnel to the Pt side and they system will build up an open circuit voltage to counteract the hot carrier tunneling. The energy of hot carriers is ~1.16 eV which is much smaller than interband transition in gold (~2.4 eV) so the hot carriers distribution are generated due to intraband transition in sp band of Au. As a result, the hot carrier distribution consists of hot electrons and cold holes. Even though the DOS of Pt is more than DOS of Au near fermi level [179] but it's been shown previously the DOS does not force the hot carrier tunneling direction. [71]

6.5. Pure gold devices

6.5.1. Results at room P and T

Fig. 6.7 shows the SEM image of pure Au junction after electromigration. The wire is completely symmetric before electromigration. This figure shows two opposite wiring during electromigration. As explained previously, switching the wiring causes the nanogap to form at the other end of the gold nanowire. For pure gold devices shown in Fig. 6.8, correct wiring for forming the gap where the width changes are shown. If the wiring is reversed, the gap will form at the other end of the thin side. Electromigrating these pure gold devices should be done within a day

after fabricating them. Note that electromigration and photovoltage of measurements of these devices are done in ambient condition. If devices are left for 2-3 days, the electromigration mostly will fail; either the device blows up or the gap forms at the end of the wider nanowire (Figure in Appendix)

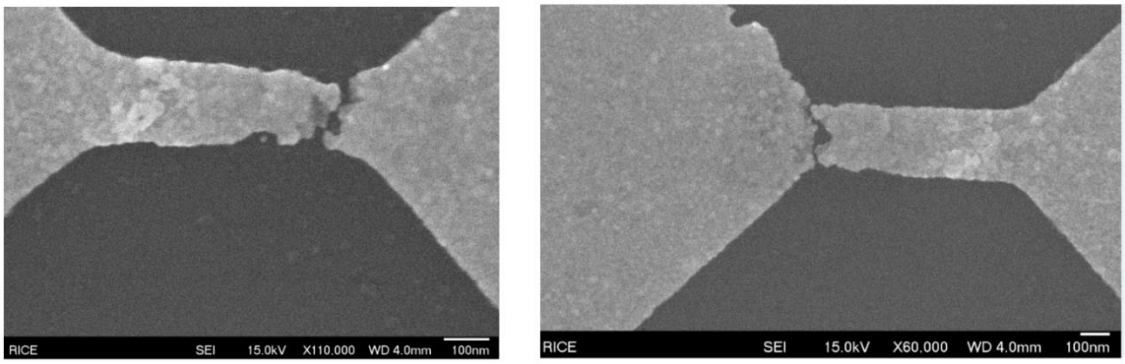

Figure 6.7. In symmetrical Ti/Au devices, when the wiring switches the place of electromigrated gap switches.

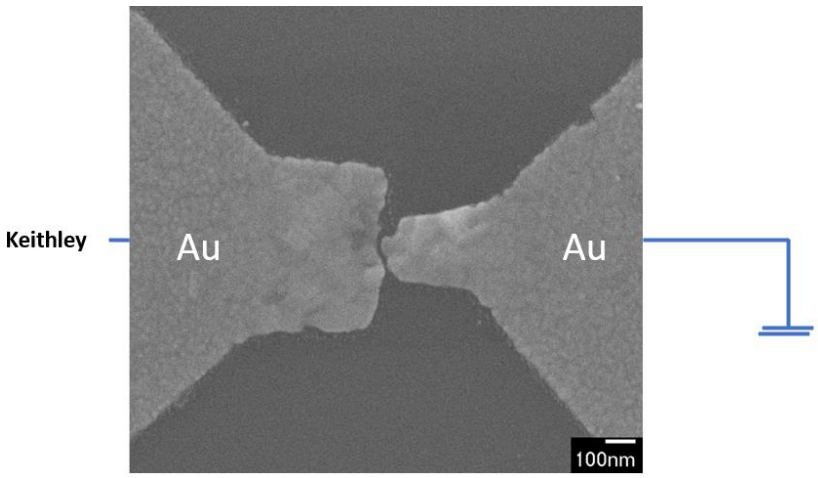

Figure 6.8. correct wiring configuration for breaking at the junction

Polarity of signal in pure gold devices after electromigration is not consistent which means there's no preference in hot carrier tunneling direction in pure gold devices. Pure gold devices are unstable in ambient conditions, and they tend to blow up easily. Results are shown in Fig. 6.9. The widths of the nanowire at two sides of the nanogap are shown with blue circles in absorption plot below. The absorptions at two ends are almost similar. The thinner side has stronger dipolar plasmon mode vs the wider side which has more volume; the normalized absorption to the volume for the thinner side is stronger than for the wider side. As shown below, the hot carriers sometimes tunnel from thin side to wider side (positive polarity) and sometimes the other way (negative polarity).

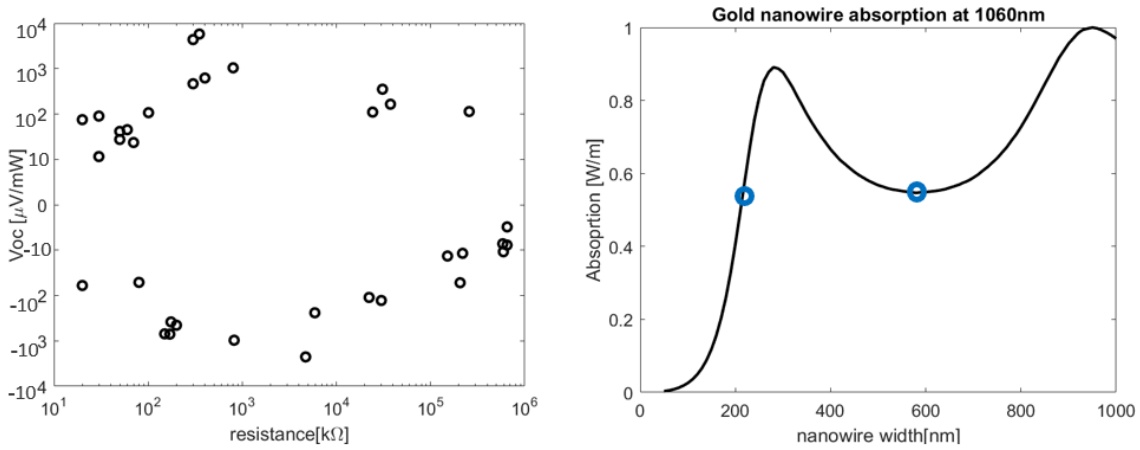

Figure 6.9. Tunneling direction in pure gold MIM junctions for 1060nm wavelength

6.5.2. Results at room T and in vacuum

We have measured pure gold devices with similar design but for 785 nm wavelength and measured them under high vacuum. In these devices, the polarity of the signal is not consistent either which means carriers do not have a favorable direction for tunneling. Fig. 6.10a shows the SEM image of such device after electromigration with corresponding widths shown with blue circles in absorption plot shown in Fig. 6.10b. Fig. 6.10c shows that measurements done under high vacuum (785 nm incident wavelength) and in ambient condition (1060 nm incident wavelength), the polarity of open circuit voltage in pure gold devices is random.

Plot of log of open circuit voltage vs the distance between two gold electrodes calculated by Eq. 2.6 is shown in Fig. 6.10d. At first, when the gap is getting larger, it increases the resistance across the nanowire. Using the ohmic formula to calculate the open circuit voltage ($Voc=R\times I_p$), the increase in resistance

causes the open circuit voltage to increase. The behavior continues to resistance between ~300 kΩ and 500 kΩ which correspond to 0.57 nm to 0.6 nm gap distance. Beyond that separation, the open circuit voltage decreases due to decreasing the hot carrier tunneling current; I_p. The probability of hot carrier tunneling decreases exponentially with increasing the thickness of gap.

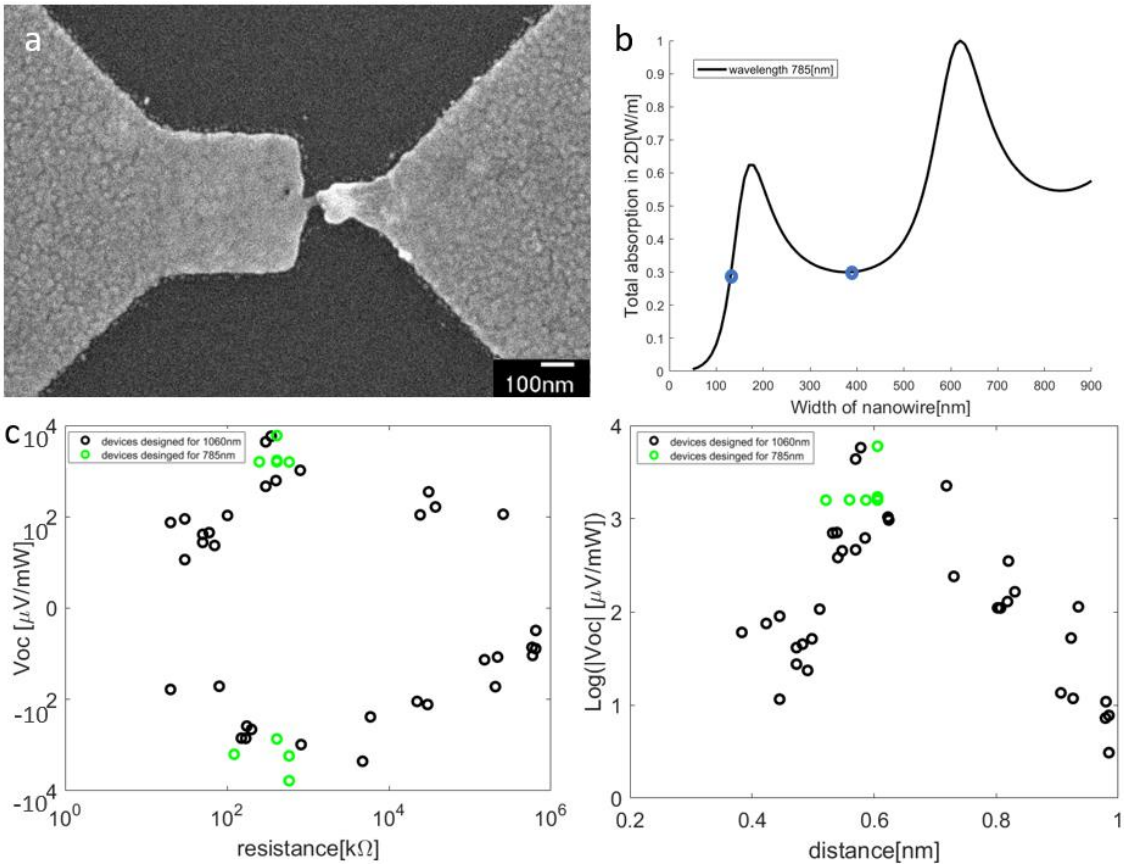

Figure 6.10. a) SEM image of a pure gold device designed for 785nm after electromigration. b) the absorption plot for a gold nanowire with different width at 785nm. The blue circles correspond to the width of nanowires on two sides of the nanogap. c) the open circuit voltage of pure gold devices at 1060

nm and 785 nm electromigrated to different resistances. d) Log of open circuit voltage vs distance between two gold electrodes.

6.5.3. Modeling the open circuit voltage vs gap size in pure gold devices

The hot carrier tunneling under optical illumination in these MIM structures can be modeled based on Landauer formula [22], [175].

Equation 6.3. Hot carrier tunneling current across MIM structure based on Landauer formula

$$I_p = \frac{e}{\pi\hbar}\frac{\dot{N}_I}{\hbar\omega_I}L(\omega_I)\int_{-\infty}^{\infty} d\varepsilon \frac{\tau_e(\varepsilon)}{\rho(\varepsilon)}\frac{\tanh\left(\frac{\varepsilon\beta_e}{2}\right)}{1+e^{-\beta_e\omega_I}\cosh(\varepsilon\beta_e)}\mathcal{T}(\varepsilon)$$

In this equation, I_p is tunneling current caused by optical excitation. e, $\hbar$, and ε, are electron charge, Planck's constant, and energy of the electrons, respectively. β_e is equal to $(k_B T_e)^{-1}$ in which k_B is the Boltzmann constant and T_e is the electronic temperature. ω_I, $\dot{N}_I$,τ_e, and $\rho(\varepsilon)$ are incident photon frequency, rate of photons hitting the sample per atom, carrier lifetime, and carriers density of states per atom, respectively. $L(\omega_I)$ is the absorption spectrum and $\mathcal{T}(\varepsilon)$ is the transmission function. For the absorption spectrum, to within a constant of proportionality we simply utilized the squared of the field enhancement between two dimers as a function of distance between them for low incoming optical power.[180], [181] The normalized squared of the field enhancement is shown in Fig. 6.11a. This spectrum is multiplied by a proper intensity enhancement coefficient of 10^5 based on the previous simulations in similar structures.[12]

Tunneling transmission function is used as $\mathcal{T}(\varepsilon)$ in Eqn.6.3 which is defined by:

Equation 6.4. Electron tunneling transmission function

$$\mathcal{T}(L,\varepsilon) = \frac{1}{cosh^2(\beta L) + \left(\frac{\gamma}{2}\right)^2 sinh^2(\beta L)}$$

In which

$$\left(\frac{\gamma}{2}\right)^2 = \frac{1}{4}\left(\frac{1-\frac{\varepsilon}{U_0}}{\frac{\varepsilon}{U_0}} + \frac{\frac{\varepsilon}{U_0}}{1-\frac{\varepsilon}{U_0}} - 2\right)$$

$$\beta = \alpha \times \sqrt{\frac{2m}{\hbar^2}(U_0 - \varepsilon)}$$

In equations above, L, U_0, and ε are barrier thickness (gap size), potential barrier height, and energy of the hot carriers. For fulfilling the tunneling condition, we should have $\varepsilon < U_0$ which is correct based on energy range of the hot carriers (~1.5 eV) and the work function of the two electrodes (W_{Au}~5.1 eV and W_{Pt}~5.7 eV). In these calculations, U_0 is approximated to be 5.4 eV. In simple MIM tunneling models, α is 1. We should note that the energy diagram here is not a simple form of what is shown in Fig. 2.11 due to image charge potential energy and electron exchange-correlation potential [78]. Also, the approximations for work functions of the Au and Pt film electrode are used. Here by choosing α of 0.7, this simple model can resonate well with the experimental data shown in Fig. 6.11d. Corresponding I_p

plot is shown in Fig.6.11c. Normalized tunneling currents for other values of α are shown in Fig. 6.11b. It is shown that when α is 1, V_{oc} follows the exponential decay of I_p and as the α gets smaller, the effect of I_p decay on V_{oc} decreases. Note that in the measurements, the resistance of the devices is recorded before the photovoltage measurements. The optical source changes the nanometer-sized details of the gap and effects the hot carrier tunneling direction and amplitude as well as the resistance of the devices drastically even at low optical power; see Fig. 8.1b and Ref [22]. Most of the time, the resistance of the device after optical measurements is higher than right after forming the gap through the electromigration process. That is the reason why the open circuit voltage fades away at larger gap distances in this model (Fig.6.11d) comparing to experimental results (Fig. 6.10d)

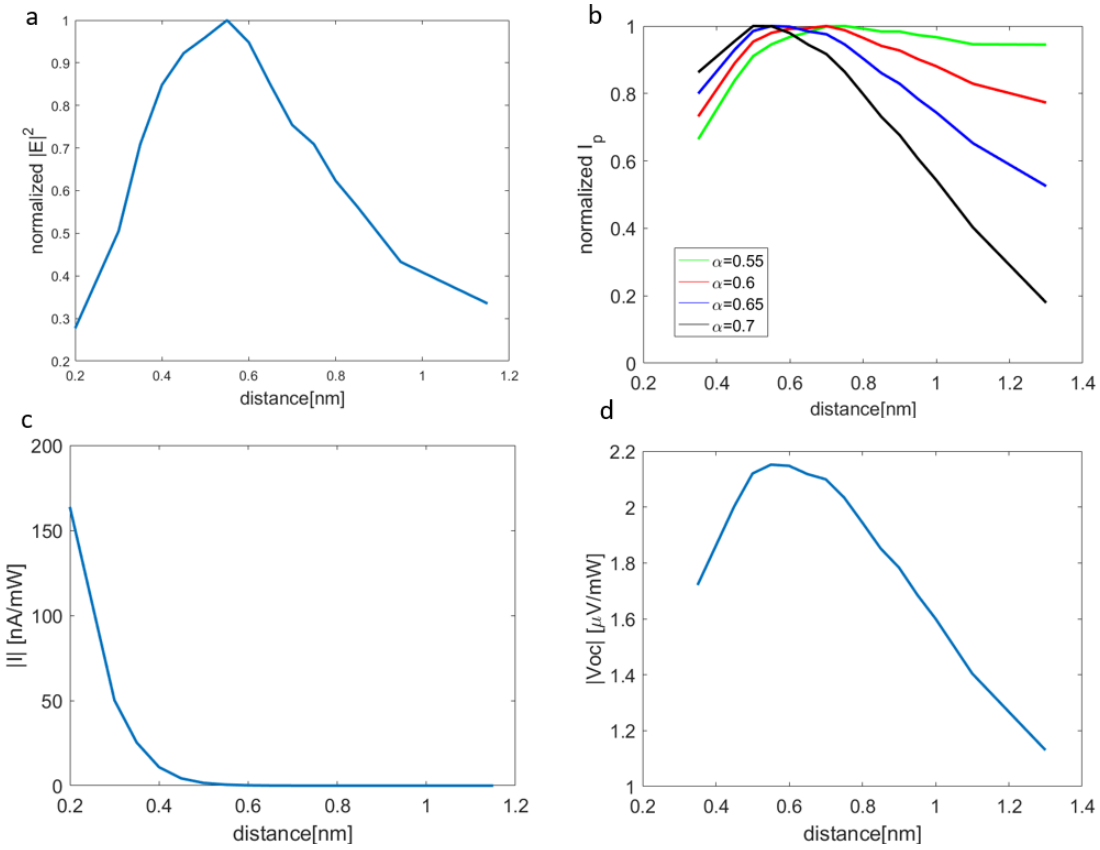

Figure 6.11. Modeling of hot carrier tunneling current and open circuit voltage vs gap size in pure gold devices. a) The normalized squared of field enhancement vs distance between two dimers based on Ref [180]. b) normalized tunneling current for different α values. c) Tunneling current corresponding to $\alpha = 0.7$. d) Open circuit voltage vs gap size corresponding to α= 0.7.

Here we introduced planar MIM junction that the hot carrier tunneling can be controlled. Also, these devices can operate at ambient conditions. Even though the MIM junction behaves in ohmic regime based on Simmons model, but by utilizing different plasmonic resonances at two sides of the nanogap, we could control the hot carrier tunneling direction in Au-air-Pt tunnel junction.

Chapter 7

Characterizing plasmon modes in metallic nanogap

This chapter is based in part on the publications:

"Electrically Driven Hot-Carrier Generation and Above-Threshold Light Emission in Plasmonic Tunnel Junctions," L. Cui, Y, Zhu, **M. Abbasi**, A. Ahmadivand, B. Gerislioglu, P. Nordlander and D. Natelson, Nano Letters, 20, 6067-6075 (2020),

7.1. Motivation and introduction

In Chapter 7, the excitation of high energy plasmon modes in plasmon MIM structure with a nanometer sized gap using an optical source was discussed. These modes can also be excited by applying voltage and through inelastic electron tunneling in similar structures. When the photons emitted due to the radiative decay of these plasmon modes have energies less than the bias-driven tunneling

electrons, the emission is called below-threshold light emission [11], [83]. Recent study in our lab show above-threshold light emission in plasmonic tunnel junctions in pure gold, where the energies of emitted photons are larger than the tunneling electron energy. Above threshold light emission has attracted interest in nano-optics [131], [182], photochemistry[183], [184], and optoelectronics[185], [186]. Previous works have developed different multi-electron models to address above threshold light emission. Models like: blackbody thermal radiation, multielectron interactions, and interpretation involving finite temperature effects [187]. The microscopic model presented here demonstrates that the above threshold light emission is caused by the recombination of plasmon-induced hot carrier dynamics in plasmonic MIM structures. COMSOL simulations are used to characterize the field enhancement and plasmonic behavior of these MIM structures.

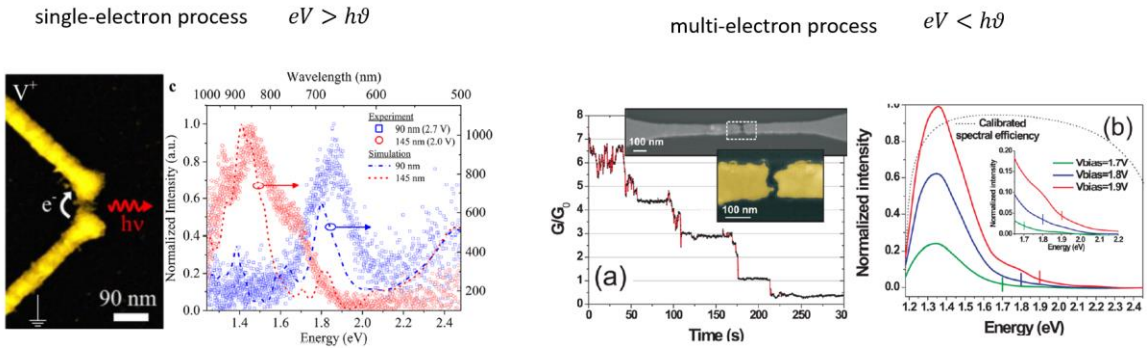

Figure 7.1. below threshold light emission vs above threshold light emission. a) shows below threshold light emission process[83]. b) above threshold ligth emission process [188]

Tunneling gaps here are formed by electromigration. Bias voltage is applied and the tunneling current and light emission are measured simultaneously. In a

pure gold nanojunction all the emitted photons can be above threshold as shown in Fig.7.2b. The light emission in Au/Cr devices are partially above threshold [12]. In what follows, COMSOL Multiphysics results along with relevant experiment results are presented to define plasmons effect in these above threshold light emissions.

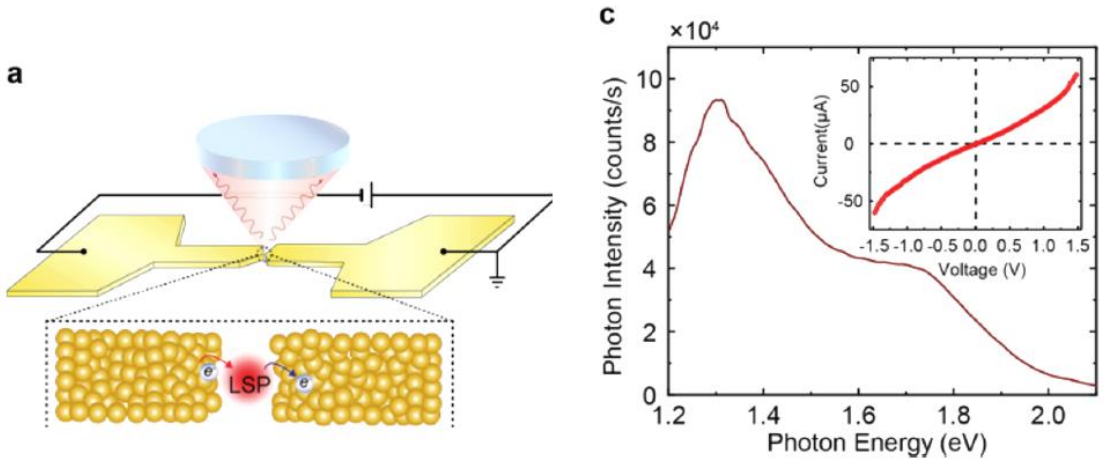

Figure 7.2. a) Schematics of the experimental setup capable of simultaneous electrical transport and optical spectroscopy measurements. LSP denotes the localized surface plasmons excited by the inelastic tunneling electrons. B) Measured light emission spectrum of the Au tunnel junction at 1.0 V. Inset shows the dc I–V characteristics of the junction. [12]

7.2. Field enhancement vs emission photon yield

In order to study the plasmonic effect of above threshold light emission in pure gold devices, the light emission measurement and field enhancement simulations are done using materials with different plasmonic properties. Au without Cr adhesion layer, Au/Cr (Au with Cr adhesion layer), Au0.6Pd0.4/Cr , and Pd/Cr are measured and simulated. These materials are written in order of

decreasing the plasmonic behavior in the red part of the visible spectrum. Au has the best plasmonicity (small imaginary part for permittivity [189]) Having Cr as adhesion layer behaves as a damping medium [190], [191]. and attenuate plasmon resonance. Pd has the worst plasmonicity here due to high resistivity and interband transitions (large imaginary part of permittivity). Au0.6Pd0.4 alloy has plasmonicity between Au and Pd.

The nano gap in the experiment is formed using electromigration method that has been described in detail in Chapter 6. It is not possible to control the nano details in the geometry of the nanogap formed by electromigration. For field enhancement COMSOL simulations, an arbitrary asymmetric metallic MIM structure is used. That is shown in Fig. 7.3a. The finite-element modelling (FEM) of the plasmonic resonances of tunnel junctions is performed using COMSOL Multiphysics in ewfd physics interface (Electromagnetic Waves Frequency Domain Physics). The metallic nanowire structure with an asymmetric gap structure (resembling the geometry of a typical tunneling junction studied here) on top of 200-nm-thick SiO2 is calculated to obtain the electrical field intensity enhancement ($|E|^2$) at different wavelengths in the tunneling gap. A linearly polarized plane wave (both in the longitudinal and transverse directions) with an electrical field amplitude of 2.5×10^5 V/m is applied normally incident on the metallic nanowire to induce the plasmonic excitations confined in the subnanometer-sized tunneling gap. Results from both polarizations are used to calculate the total electrical field intensity enhancement at different wavelengths to reveal the dominant plasmonic modes of the nanowire and the enhanced electromagnetic field is assessed in the tunneling gap region. The

wavelength dependent relative permittivity of Au, Cr, $Au_{0.6}Pd_{0.4}$ and Pd are taken from previous work [94], [97], [192], [193]. Simulation results in Fig. 7.4 are for 1nm gap size and at 785 nm incident wavelength. We have also conducted numerical simulations at different wavelength and gap sizes. Fig. 7.5 shows the calculation results for plane waves at 955 nm in a tunnel junction with the gap size of 1 nm. 955 nm corresponds to the observed typical low energy light emission peak shown in Fig. 7.2. It can be seen that the calculated plasmonic enhancement increased by approximately a factor of 10-20 from Pd/Cr to Au tunnel junctions in both figures 7.5 and 7.4. Furthermore, the plasmonic mode and enhancement effects in a tunnel junction with gap size of 4 nm was also evaluated. As shown in Fig. 7.5e to h, the electric field intensity enhancement is found to be smaller in the larger gap scenario as expected for a gap that is beyond the tunneling regime. Similar to the 1 nm gap case, the plasmonic intensity enhancement effects among different materials only differ by one order of magnitude. In experimental results shown in figure 7.2 a and b, the photon yield (#photons/#electrons) differs by four orders of magnitude of difference in above-threshold light emission. But similar to simulations, photon yield follows plasmonic characteristic of the devices meaning gold has the highest and Pd has the lowest photon yield. These numerical calculations provide details to validate our claim that the observed above-threshold light emission and the giant material dependence in photon yield cannot be simply explained by the plasmonically enhanced optical density of states in the tunneling gap. In Ref [12] a model is developed that shows above threshold light emission can be modeled by

Boltzmann distribution and plasmonic characteristic of the nanogap. The model is briefly explained in section 7.2.1.

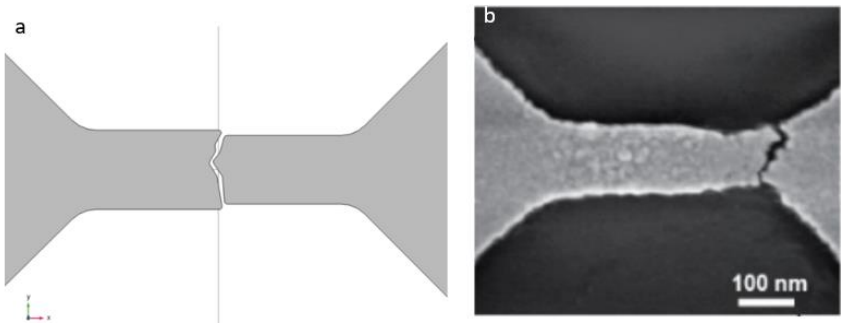

Figure 7.3. asymmetric MIM structure in a)simulation and b)one device in experiment

The Field enhancement simulation results are compared with the experiemntal photon yield (emitted photons per incident electrons: U/I in which U is the total photon counts and I is the tunnling current.). In what follows, it is shown that this mismatch is due to recommbination of hot carriers generated from the plasmon decay in these structures.

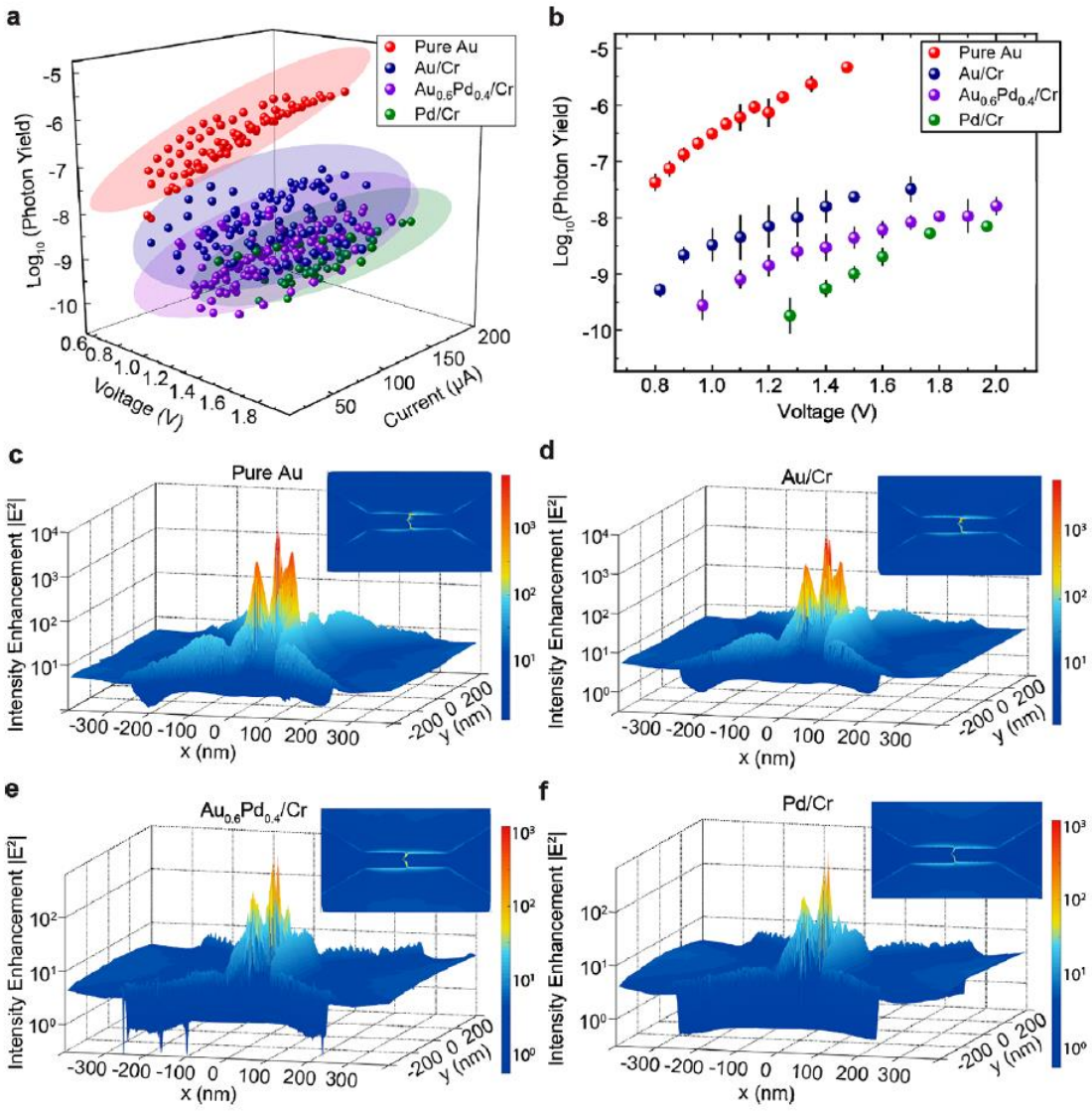

Figure 7.4. Field enhancement in the gap and photon yield. a) Measured photon yield (plotted on logarithmic scale) for ~100 tunnel junction devices made of different materials versus applied voltage and tunneling current. The ellipsoids correspond to a 95% confidence interval fit to the experimental data. b) Finite-element simulation results of plasmon-induced electric field intensity enhancement (proportional to the local photon density of states in the gap) at 785 nm (corresponds to the peak wavelength of the observed light emission) for the Au junction. The insets show the top-view of the 3D plots, indicating the geometry of the simulated junction and the 2D intensity. (d–f)

168

Same as (c), but for junctions made of other materials. The field enhancement is seen to be smaller than that in (c). add reference for a and b.

Plasmon-induced radiative field enhancement (a direct indicator of the strength of the plasmonic resonances) can be inferred directly from the calculation of the electrical field intensity within the tunneling gap. The quality of a plasmonic material can be quantified by its plasmonicity [189] and is mainly determined by the imaginary part of the relative permittivity. The permittivities at 785 nm are Au, −22.855 + 1.4245i; Cr, −2.0612 + 21.601i; and Pd, −21.243 + 20.086i, clearly showing the superiority of Au as a plasmonic material.

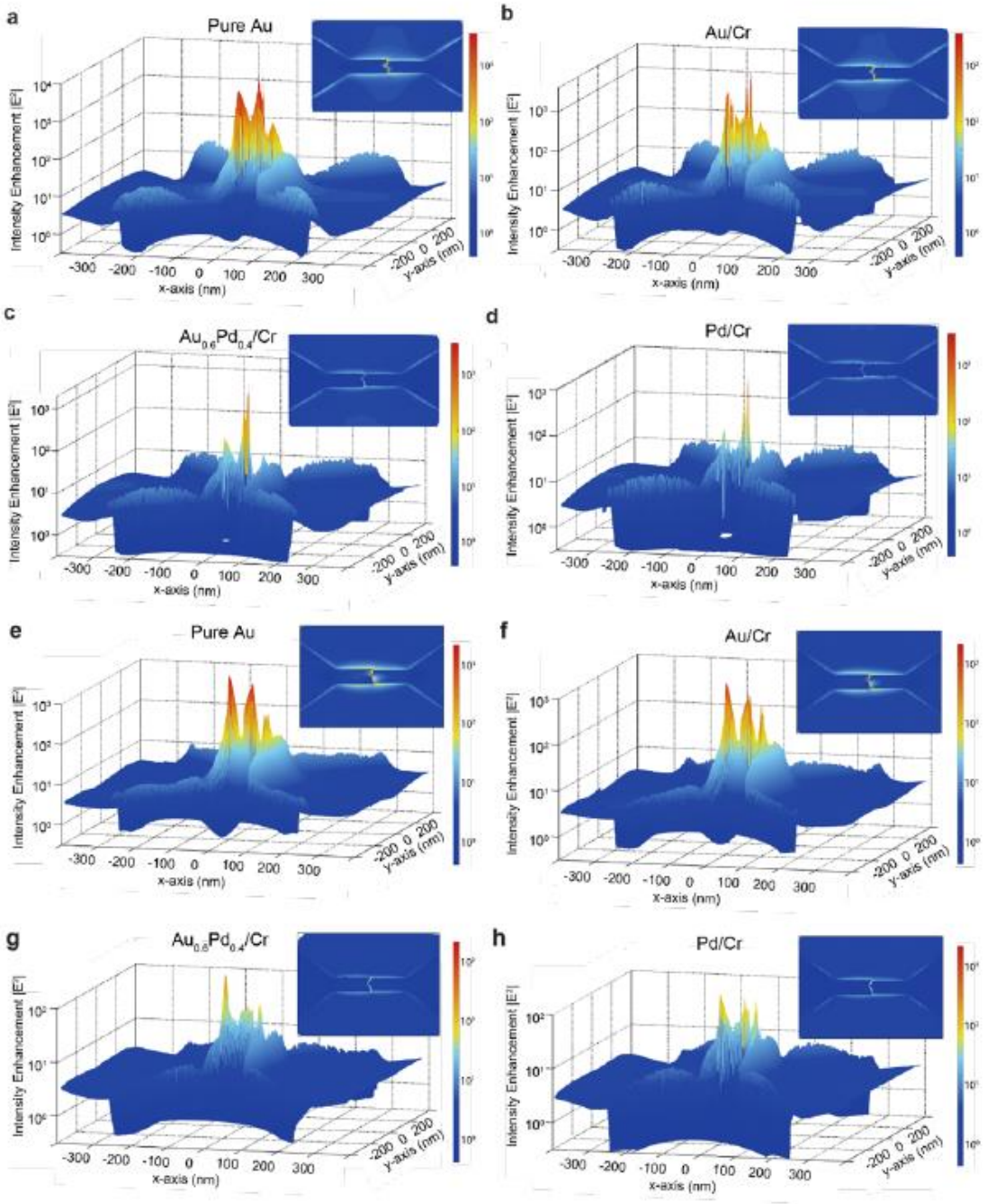

Figure 7.5. Calculated electric field intensity enhancement in the tunneling gap for different wavelength and gap sizes. a to d) show the calculation for 955

nm (~1.3 eV, corresponding to the typically observed low energy light emission peak) for different materials with 1 nm tunneling gap. The gap size in this simulation is the same as that in Fig. 3c to 3f. e to h) show the results for 785 nm (corresponding to the high energy light emission peak) for different materials with 4 nm tunneling gap. The insets show the top-view of the 3D plots, indicating the geometry of the simulated junction and the intensity enhancement

7.2. Plasmonic characteristics of the nanogap

The emission spectra at different voltages are first normalized to the spectrum obtained at the highest voltage. [12], [187]. The normalization separates the contribution of voltage-independent plasmonic resonances of the tunnel junction, which depends only on junction geometry and the material type, from the voltage-dependent component of observed light emission. Normalized intensity in logarithmic scale vs photon energy is linear as shown in Fig. 7.6a. This energy dependence of light emission can be described by a Boltzmann statistics factor

Equation 7.1. Boltmzann statistics with an effective temperature

$$e^{-\frac{\hbar\omega}{k_\beta T_{eff}}}$$

Where Teff is an effective temperature of the hot carriers, out of equilibrium with the lattice and the background of cold electrons that exceed 2000K. The reason for this high temperature is that the time interval between consecutive tunneling events (~e/I=0.16ps at 10uA). These LSPs decay nonradiatively into hot electron-hole pairs and through electron-electron scattering form a steady-state distribution

as the generation rate of hot carriers outpaces the decay rate. Based on Fig. 7.6, we see that at higher applied voltages, this temperature is higher. The correlation between T_{eff} and applied V is further investigated in Fig. 7.6b. As shown in Fig. 7.6b. a linear relationship between T_{eff} and the applied voltage is clearly indicated. This observation shows that electrically driven generation and relaxation of plasmon-induced hot carriers are responsible for these above threshold emissions. Moreover Fig. 7.6b shows that T_{eff} of materials with poorer plasmonicity is lower. This observation provides evidence that plasmons play a key role in the generation of the hot carriers. On contrary, in previous thermal models, the blackbody radiation of the hot electron gas generates broadband above threshold light emission, the T_{eff} linearly changed with dissipated power [188], [194]. In blackbody radiation the T_{eff} doesn't change with the gap distance which is not the case in our system. [187]

Even though the realistic quantitative theory is extremely challenging, our microscopic model can capture the essential physics of electrically driven process of hot carrier generation and relaxation. Inelastic tunneling electrons can excite all localized plasmon modes (bright and dark) in the tunnel junction [195]. Excited LSPs decay nonradiatively in which a plasmon energy quantum $\hbar\omega_{LSP}$ is decay through landau damping [66] and generate an individual conduction hot electron-hole pair. The energy distribution of these hot carriers is centered around the Fermi level E_F and extends to $E_F \pm eV$. If the rate of tunneling events outpaces carrier relaxation, a steady-state hot carrier distribution is sustained, with its specific form depending on the time interval between successive electron tunneling events ($\propto e/I$) and the hot carrier lifetimes (approximately hundreds of femtoseconds)[62].

For devices with higher resistance that have smaller tunneling current, tunneling time interval decreases and so the effective temperature. The above-threshold light emission originates from the plasmon-enhanced radiative recombination of hot electrons and holes with high energies in the hot-carrier distribution. Here, a prediction is that a steady-state effective temperature of the hot carriers is directly correlated with the bias window (eV) applied to drive the plasmonic process, rather than the dissipated electrical power.

Equation 7.2. T_{eff} depends on the applied voltage and plasmonic characteristic

$$k_B T_{eff} \propto \beta eV$$

where β is material-dependent parameter correlated with the quality of plasmonic response of a material.

Spectral intensity of the light emission can be well described by a Boltzmann distribution with T_{eff}, the tunneling current that changes nonlinearly with the emission and the plasmonic characteristics of the gap:

Equation 7.3. Emission spectrum

$$U(\omega) \approx \rho(\omega) I^{\alpha} \hbar\omega e^{-\hbar\omega/k_B T_{eff}}$$

where $\rho(\omega)$ is the local photon density of states (which gives the radiative field enhancement effect due to LSPs for a given junction), α indicates the nonlinear tunneling current-dependence of the above-threshold light emission. The value of α,

always greater than 1, is obtained from the experimental results. This model is inspired by the hot carrier model [196] to explain anti-stokes photoluminescence in plasmonic nanoparticles with light emission energy above energy of the applied photons. Using eq 2, combined with the Teff obtained from the Boltzmann statistics, it is possible to extract *ρ(ω)*. This *ρ(ω)* contains plasmonic characteristic of the nanogap which is independent of the applied voltage. As shown in Fig. 7.6c all the *ρ(ω)* plots for a particular device at different applied voltages collapse together. Further, this plasmonic characteristic of the nanogap matches well with plasmonic characteristics modeled using COMSOL simulation: inset of Fig. 7.6c. Exact plasmonic characteristics here depends on nano-scaled details in nanogap geometry [181]. That is why experimental achieved *ρ(ω)* shown in Fig. 7.6c is unique for each broken junction. And that is why there is a small mismatch between simulations and experimentally achieved *ρ(ω)*.

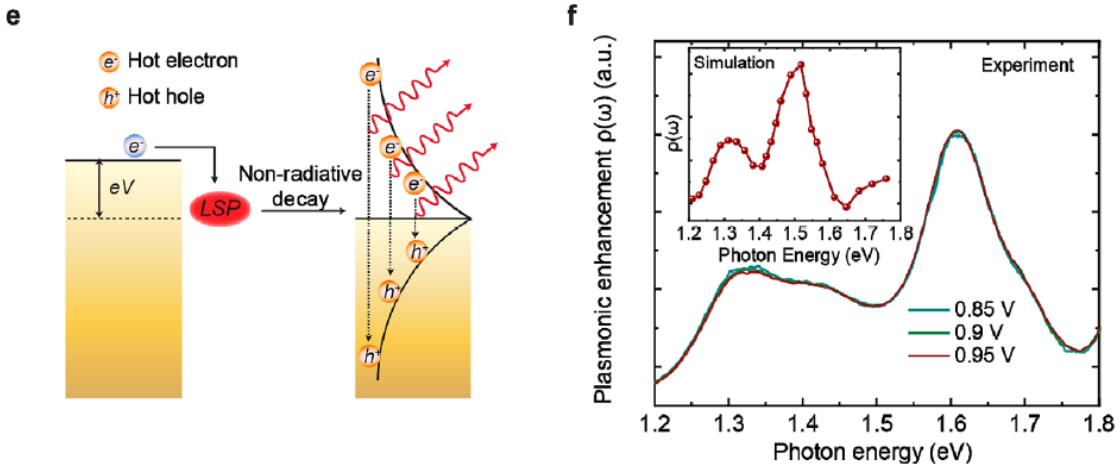

Figure 7.6. a) Normalization analysis of the spectra in Fig1.a., by dividing the measured spectrum at 0.8, 0.85, and 0.9 V with reference to the spectrum at 0.95 V. The linear decay of the normalized spectra (on logarithmic scale) is

fitted to a Boltzmann energy distribution exp(-hω/k_BT_{eff}) (solid red lines), where Teff is the effective temperature of hot carriers (electrons and holes). b) Statistical analysis on Teff as a function of applied voltage (V). The solid lines are the best linear fit to the data. Error bars are the standard deviation over the ensemble of junctions for each material at the applied voltage. c) Extracted voltage-independent spectral plasmonic enhancement, ρ(ω), due to LSPs in the tunnel junction from applying eq7.3. Inset shows the numerically calculated plasmonic enhancement for a tunnel junction with a similar geometry.

For simulating the plasmonic behavior of the nanogap, different experimental references of permittivity for gold have been simulated as well as different geometry. These simulations show that plasmonic behavior in the nanogap is not very sensitive to small changes in permittivity but rather it follows geometry details; see Appendix A. Even though field enhancement COMSOL simulation show the plasmonic characteristics of these MIM structures with nano-meter sized gap, but it cannot solely describe the strong material dependent photon yield in the experiments as the recombination of hot electron-hole pairs formed by plasmon decay are responsible for the emission observed in the experiment. After processing the experimental results, the plasmonic characteristic of the nanogap can be extracted that matches with the plasmonic behavior simulated in the nanogap.

Chapter 8

Conclusion and future directions

8.1. Summary and Conclusion

This thesis mainly discussed two categories: PTE signal in gold nanowires (Chapters 4 and 5) and hot carriers generation gold nanowires (Chapter 7 and 8).

It is shown that the photothermoelectric effect can be used for photodetectors that do not need an external bias or a cooling unit to operate (Chapter 4). As a result, the noise of these detectors can potentially be limited by thermal noise and these devices require smaller space than competing designs. In comparison with PV based photodetectors, PTE based photodetectors can be slower in response. The response of PTE based photodetectors are wider in spectrum comparing to PV based photodetectors that their response is limited to bandgap of the active material. In the IR range where the band gap of the material should be small in PV based photodetectors, the dark current can increase. Plasmons are

utilize in PTE based single metal photodetectors to increase the heating. By doing so, photodetectors are sensitive to wavelength and polarization of incoming light. Later in Chapter 5, PTE measurement are used to probe the internal characteristics of gold nanowires. A simple PTE measurement gives us high accuracy in measuring internal strain, crystal misorientation, and Pt impurity in single crystalline gold nanowires. In this thesis COMSOL simulation is used to extract the Seebeck map across these devices. By using Seebeck coefficient change extracted from simulation and by comparison with experiments, we calculated the accuracy in our detection technique.

COMSOL Multiphysics Simulations are used throughout this thesis for either characterizing the behavior of our devices and to back up the proposed process in the experimental results (Chapter 4-7) or to design our structures prior to measurements (Chapter 4).

In second part of the thesis, hot carrier generation in gold nanowires are discussed. In Chapter 6 we presented planar MIM junctions with dissimilar metallic electrodes; Au and Pt. Due to symmetry breaking in sub-nanometer gap, we can excite localized high energy plasmon modes in the nanogap with optical excitation. The hot carrier distributions caused by plasmon decay are asymmetric in this design. So, the hot carriers generated in the vicinity of the gap have a preferred tunneling direction; from Au to Pt. By controlling hot carrier tunneling direction, the polarity of photovoltage can be controlled. Potentially these structures can be used to build photodetectors with higher responsivity and faster response time

comparing to PTE based photodetectors. In stacked MIM devices, controlling the hot carrier tunneling direction is easier as the top electrode absorption is higher than the bottom electrode. The LSPs on the surface of the top electrode as well as SPPs in the MI interface can both contribute to the absorption. [79], [81] In our planar design, due to exciting extremely localized plasmon modes in the nanogap, the hot carriers are generated very close to MI interface. This increases the efficiency of hot carrier tunneling to the other electrode comparing to stacked MIM devices in which the light decay evanescently from surface of the top electrode to the MI interface. Here we showed by utilizing dissimilar metals with different plasmonic characterizations, we can control the hot carrier tunneling even when both electrodes are excited in the same plane. These in planar junctions require less space and have lower weight comparing to stacked MIM devices.

Above threshold light emission in these MIM tunnel junction with similar metallic electrodes are discussed in Chapter 7. The localized plasmons modes in the nanogap are excited by inelastic tunneling of electrons through applying a bias across the junction. The above threshold light emission in these devices is modeled through an effective Boltzmann distribution with an effective temperature, that represents the quasithermal distribution of generated hot carriers due to plasmon decay, times the plasmonic characteristic of the nanogap. Both simulations and experiments show that these plasmonic characteristics follows geometry details in the nanogap. (See Appendix A.2.6)

8.2. Future direction

By comparing results from Chapter 6 and Chapter 7 we see that pure gold nanogaps are more stable in their plasmonic behavior so in their nanometer details in the nanogap. If we measure them optically for detecting hot carrier tunneling, the photovoltage changes from scan to scan even by using low laser power ~50 μW. Even though the electroluminescence data are taken at 5 K and PV data are taken at room T shown in this thesis, similar instability in photovoltage at low temperatures has been observed previously. [22] Power dependent photovoltage measurement of these nanogaps can reveal possible nonlinearity and instability of these junction under direct illumination comparing to what is seen in electroluminescence. Other than direct illumination, remote excitation of LSP through coupling to optically excited SPPs from gratings far from the gap can increase the stability of these gaps. The grating dimension simulated for 1060 nm incident wavelength for gold bowtie structures are shown in Appendix 2.1 for future references.

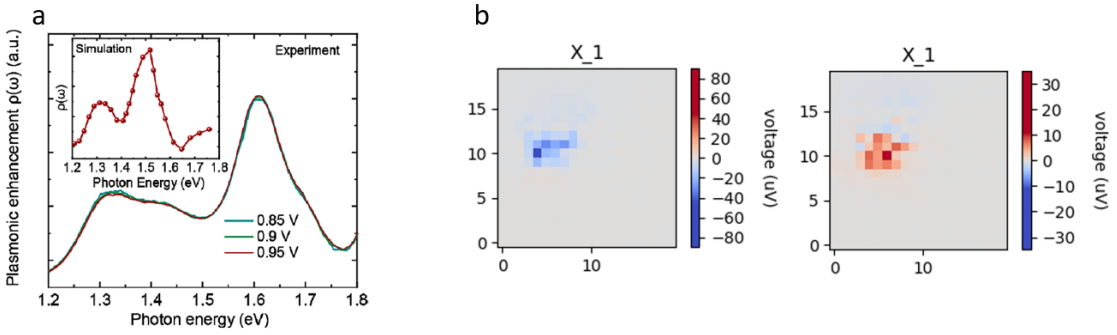

Figure 8.1. Stability of nanogaps in pure gold devices under high vacuum. a) the plasmonic characteristic of the device calculated from

electroluminascence at 5K. b) Two subsequent photovoltage maps at room T with 50 μW CW laser.

The light and matter interaction increases with exciting localized plasmons (polarization dependent), surface roughness, and on corners of the nanowire due to lightening rod effect (polarization independent) [91] PTE measurements at two polarizations can be used to extract the surface map to some extent. See Appendix A.

In Chapter 7 and in Appendix A.2.6 it is shown that the geometry details of the nanogap can change the plasmonic characteristic of our tunnel junctions. Controlling these details is not possible in electromigrated gaps. Gaps formed by self-aligned method [10], [89]or mechanically[197] can give us more control in details of the nanogap. Currently COMSOL simulation studies characterizing details of the plasmons modes caused by the symmetry-breaking geometry of the nanogaps in gold nanowires are in progress in our lab.

Increasing the underlying oxide thickness can increase the heating and so the responsivity of our photodetectors. Using thicker oxide can also protect our devices in wire bonding process. If the bonder can pierce through the oxide, the optical excitation can couple to the silicon underneath and the photovoltage is no longer from our metallic nanowire. Energy flux reached to the Si underneath is simulation and shown in Appendix A.2.2. Measuring these photodetectors at lower temperature can increase their responsivity as well because the thermal boundary resistance to the substrate increases at lower temperatures.[24]

We've seen that different plasmon modes causes different change distribution on our metallic nanostructure (see Fig.2.7). Applying a static magnetic field can move the surface charges around and so it can change the plasmon energy and so the photovoltage response of our devices. Early simulation results for this effect are shown in Appendix A.2.3.

For shifting the plasmonic response, other than changing the geometry, we can utilize other plasmonic materials. Appendix A.2.5 show the plasmonic response of Au, Al, and Ag nanowires at different incident wavelength and at different widths for future designs. Note that the oxide layer formed on Al nanowires can red shift the plasmon peak as shown in Appendix A.2.6.

Our Andor iXon3 camera can be used to image the light emission from these nanogaps by Electron Multiplying Charge Coupled Device (EMCCD) with great details. These images can give valuable information about the location of light emission in the nanogap. See Appendix A.2.7.

Integrating our metallic based photodetectors with 2D materials can be beneficial in their performance and possible future application. Integrating our metallic based photodetectors with 2D semiconductors like MoS_2 can increase the figure of merit (*ZT*) and make them also suitable for energy harvest application. Graphene by itself is not a good thermoelectric material because of its high thermal conductivity and small Seebeck coefficient [198], [199] however due to its zero-bandgap and high mobility, it is possible to produce a non-equilibrium effect in graphene by applying photons. Because the electron-phonon interaction in

graphene is weak [200], nonequilibrium heating of charge carriers gets much higher than lattice temperature and cause PTE based PDs that are fast with high responsivity. Similar to Ref [201], graphene in our gold nanogap can make a localized photodetector.

In our MIM planar junction with dissimilar electrode, Au can be used with other metals junction but either the measurement should be done under high vacuum or a flow of nitrogen gas should be equipped to avoid oxidization of the other metal. The self-aligned method [89] might be more appropriate for metallic junctions that oxidize as it takes about 1 hour to break a junction properly through the electromigration process.

References

[1] C. Wood, “Materials for Thermoelectric Energy Conversion,” *Reports on Progress in Physics*, vol. 51, p. 495, 1988.

[2] A. J. Minnich, M. S. Dresselhaus, Z. F. Ren, and C. Chen, “Bulk Nanostructured Thermoelectric Materials: Current Research and Future Prospects,” *Energy & Environmental Science*, vol. 2, pp. 466–479, 2009.

[3] M. Buscema, M. Barkelid, V. Zwiller, H. S. J. van der Zant, G. A. Steele, and A. Castellanos-Gomez, “Large and Tunable Photothermoelectric Effect in Single-Layer MoS2,” *Nano Letters*, vol. 13, no. 2, pp. 358–363, 2013.

[4] M. Abbasi, C. Evans, L. Chen, and D. Natelson, “Single Metal Photodetectors Using Plasmonically-Active Asymmetric Gold Nanostructures,” *ACS Nano*, vol. 14, no. 12, pp. 17535–17542, 2020.

[5] X. Lu, L. Sun, P. Jiang, and Z. Bao, “Progress of Photodetectors Based on the Photothermoelectric Effect,” *Adv. Mater.*, vol. 31, no. 50, 2019.

[6] G. P. Szakmany, “Novel Nanoscale Single-Metal Polarization-Sensitive Infrared Detectors,” *IEEE Transactions on Nanotechnology*, vol. 12, no. 2, pp. 379–383, 2015.

[7] N. F. Mott, H. Jones, H. Jones, and H. Jones, *The theory of the properties of metals and alloys*. Courier Dover Publications, 1958.

[8] A. Mortlock, “The Effect of Tension on the Thermoelectric Properties of Metals,” *Australian Journal of Physics*, vol. 6, no. 4, pp. 410–419, 1953.

[9] E. Prodan, C. Radloff, N. J. Halas, and P. Nordlander, "A Hybridization Model for the Plasmon Response of Complex Nanostructures," *Science*, vol. 302, no. 5644, pp. 419–422, 2003.

[10] J. B. Herzog, M. W. Knight, Y. Li, K. M. Evans, N. J. Halas, and D. Natelson, "Dark Plasmons in Hot Spot Generation and Polarization in Interelectrode Nanoscale Junctions," *Nano Letters*, vol. 13, no. 3, pp. 1359–1364, 2013.

[11] J. Lambe and S. L. McCarthy, "Light Emission from Inelastic Electron Tunneling," *Physical Review Letters*, vol. 37, p. 923, 1976.

[12] L. Cui *et al.*, "Electrically Driven Hot-Carrier Generation and Above-Threshold Light Emission in Plasmonic Tunnel Junctions," *Nano Letters*, vol. 20, no. 8, pp. 6067–6075, 2020.

[13] L. Landau and E. Lifshitz, "Statistical Physics," in *Statistical Physics*, London, 1958.

[14] C. Kittel, *Introduction to Solid State Physics*.

[15] A. M. Guenault, "A Physical Picture for Phonon Drag Thermoelectric Power," *Journal of Physics F: Metal Physics*, vol. 1, no. 373, 1971.

[16] F. A. Otter Jr., "Thermoelectric Power and Electrical Resistivity of Dilute Alloys of Mn, Pd, and Pt in Cu, Ag, and Au," *Journal of Applied Physics*, vol. 27, no. 197, 1956.

[17] G. P. Szakmany, A. O. Orlov, G. H. Bernstein, and W. Porod, "Single-Metal Nanoscale Thermocouples," *IEEE Transactions on Nanotechnology*, vol. 13, no. 6, pp. 1234–1239, 2014.

[18] W. Sun, H. Liu, W. Gong, L.-M. Peng, and S.-Y. Xu, "Unexpected Size Effect in the Thermopower of Thin-Film Stripes," *Journal of Applied Physics*, vol. 110, no. 083709, 2011.

[19] X. Wang, C. I. Evans, and D. Natelson, "Photothermoelectric Detection of Gold Oxide Nonthermal Decomposition," *Nano Letters*, vol. 18, no. 10, pp. 6557–6562, 2018.

[20] H. Liu, W. Sun, and S.-Y. Xu, "An Extremely Simple Thermocouple Made of a Single Layer of Metal," *Advanced Materials*, vol. 24, no. 24, pp. 3275–3279, 2012.

[21] P. Zolotavin, C. I. Evans, and D. Natelson, "Substantial Local Variation of the Seebeck Coefficient in Gold Nanowires," *Nanoscale*, vol. 9, pp. 9160–9166, 2017.

[22] P. Zolotavin, C. I. Evans, and D. Natelson, "Photothermoelectirc Effects and Large Photovoltages in Plasmonic Au Nanowires with Nanogaps," *Journal of Physical Chemistry Letters*, vol. 8, no. 8, pp. 1739–1744, 2017.

[23] C. I. Evans and D. Natelson, "Remote Excitation of Hot Electrons via Propagating Surface Plasmons," *Journal of Physical Chemistry C*, vol. 123, no. 15, pp. 10057–10064, 2019.

[24] P. Zolotavin, A. Alabastri, P. Nordlander, and D. Natelson, "Plasmonic Heating in Au Nanowires at Low Temperatures: The Role of Thermal Boundary Resistance," *ACS Nano*, vol. 10, no. 7, pp. 6972–6979, 2016.

[25] A. I. Boukai, Y. Bunimovich, J. Tahir-Kheli, J.-K. Yu, W. A. Goddard III, and J. R. Heath, "Silicon Nanowires as Efficient Thermoelectric Materials," *Nature*, vol. 451, pp. 168–171, 2008.

[26] L. D. Hicks and M. S. Dresselhaus, "Effect of Quantum-Well Structures on the Thermoelectric Figure of Merit," *Physical Review B*, vol. 47, no. 19, pp. 12727–12731, 1993.

[27] K. J. Tielrooij *et al.*, "Hot-carrier photocurrent effects at graphene–metal interfaces," *Journal of Physics: Condensed Matter*, vol. 27, no. 16, p. 164207, 2015.

[28] N. M. Gabor *et al.*, "Hot Carrier-Assisted Intrinsic Photoresponse in Graphene," *Science*, vol. 334, no. 6056, pp. 648–652, 2011, doi: 10.1126/science.1211384.

[29] M. W. Knight, H. Sobhani, P. Nordlander, and N. J. Halas, "Photodetection with Active Optical Antennas," *Science*, vol. 332, no. 6030, pp. 702–704, 2011.

[30] A. M. Bagher, M. M. A. Vahid, and M. Mohsen, "Types of solar cells and application," *American Journal of optics and Photonics*, vol. 3, no. 5, pp. 94–113, 2015.

[31] H. J. Goldsmid, *Introduction to Thermoelectricity*. Springer Berlin Heidelberg, 2009.

[32] R. Franz and G. Wiedemann, "Ueber die Wärme-Leitungsfähigkeit der Metalle," *Annalen der Physik*, vol. 165, no. 8, pp. 497–531, 1853.

[33] Y.-M. Lin, X. Sun, and M. S. Dresselhaus, "Theoretical Investigation of Thermoelectric Transport Properties of Cylindrical Bi Nanowire," *Physical Review B*, vol. 62, no. 4610, 2000.

[34] A. I. Hochbaum *et al.*, "Enhanced Thermoelectric Performance of Rough Silicon Nanowires," *Nature*, vol. 451, pp. 163–167, 2008.

[35] M. L. Brongersma, N. J. Halas, and P. Nordlander, "Plasmon-Induced Hot Carrier Science and Technology," *Nature Nanotechnology*, vol. 10, pp. 20–34, 2015.

[36] K. A. Willets and R. P. Van Duyne, "Localized Surface Plasmon Resonance Spectroscopy and Sensing," *Annaul Review of Physical Chemistry*, vol. 58, pp. 267–297, 2007.

[37] L. Novotny and N. van Hulst, "Antennas for Light," *Nature Photonics*, vol. 5, pp. 83–90, 2011.

[38] L. Novotny and B. Hecht, *Principles of Nano-Optics*, 2nd ed. Cambridge University Press, 2012.

[39] J. M. Luther, P. K. Jain, T. Ewers, and A. P. Alivisatos, "Localized Surface Plasmon Resonances Arising from Free Carriers in Doped Quantum Dots," *Nature Materials*, vol. 10, pp. 361–366, 2011.

[40] H. Wang, D. W. Brandl, F. Le, P. Nordlander, and N. J. Halas, "Nanorice: A Hybrid Plasmonic Nanostructure," *Nano Letters*, vol. 6, no. 4, pp. 827–832, 2006.

[41] S. J. Oldenburg, R. D. Averitt, S. L. Westcott, and N. J. Halas, "Nanoengineering of Optical Resonances," *Chemical Physics Letters*, vol. 288, no. 2–4, pp. 243–247, 1998.

[42] M. B. Mohamed, V. Volkov, S. Link, and M. A. El-Sayed, "The 'Lightning' Gold Nnaorods: Fluerescence Enhancement of Over a Million Compared to the Gold Metal," *Chemical Physics Letters*, vol. 317, no. 6, pp. 517–523, 2000.

[43] K. M. Evans, P. Zolotavin, and D. Natelson, "Plasmon-Assisted Photoresponse in Ge-Coated Bowtie Nanojunctions," *ACS Photonics*, vol. 2, no. 8, pp. 1192–1198, 2015.

[44] M. Moskovits, "Surface-Enhanced Spectroscopy," *Review of Modern Physics*, vol. 57, p. 783, 1985.

[45] J. I. Gersten and A. Nitzan, "Photophysics and Photochemistry near Surfaces and Small Particles," *Surface Science*, vol. 158, no. 1–3, pp. 165–189, 1985.

[46] E. Kretschmann and H. Raether, "Notizen: Radiative Decay of Non Radiative Surface Plasmons Excited by Light," *Journal of Nature Research A*, vol. 23, no. 12, pp. 2135–2136, 1968.

[47] A. Otto, "Excitation of Nonradiative Surface Plasma Waves in Silver by the Method of Frusrated Total Reflection," *Journal of Physics*, vol. 216, no. 398–410, p. 1968.

[48] C. I. Evans, P. Zolotavin, A. Alabastri, J. Yang, P. Nordlander, and D. Natelson, "Quantifying Remote Heating from Propagating Surface Plasmon Polaritons," *Nano Letters*, vol. 17, no. 9, pp. 5646–5652, 2017.

[49] D. Benner, J. Boneberg, P. Nurnberger, R. Waitz, P. Leiderer, and E. Scheer, "Lateral and Temporal Dependence of the Transport through an Atomic Gold Contact under Light Irradiation: Signature of Propagating Surface Plasmon Polaritons," *Nano Letters*, vol. 14, no. 9, pp. 5218–5223, 2014.

[50] P. Alonso-Gonzalez *et al.*, "Acoustic Terahertz Graphene Plasmons Revealed by Photocurrent Nanoscopy," *Nature Nanotechnology*, vol. 12, pp. 31–35, 2017.

[51] H. A. Atwater, "The promise of plasmonics," *Scientific American*, vol. 296, no. 4, pp. 56–63, 2007.

[52] K. and Catchpole and A. Polman, "Plasmonic solar cells," *Optics express*, vol. 16, no. 26, pp. 21793–21800, 2008.

[53] J. A. Schuller, E. S. Barnard, W. Cai, Y. C. Jun, J. S. White, and M. L. Brongersma, "Plasmonics for extreme light concentration and manipulation," *Nature materials*, vol. 9, no. 3, pp. 193–204, 2010.

[54] G. Lozano *et al.*, "Plasmonics for solid-state lighting: enhanced excitation and directional emission of highly efficient light sources," *Light: Science & Applications*, vol. 2, no. 5, pp. e66–e66, 2013.

[55] L. R. Hirsch *et al.*, "Nanoshell-mediated near-infrared thermal therapy of tumors under magnetic resonance guidance," *Proceedings of the National Academy of Sciences*, vol. 100, no. 23, pp. 13549–13554, 2003.

[56] F. Le *et al.*, "Metallic nanoparticle arrays: a common substrate for both surface-enhanced Raman scattering and surface-enhanced infrared absorption," *ACS nano*, vol. 2, no. 4, pp. 707–718, 2008.

[57] F. Hao, E. M. Larsson, T. A. Ali, D. S. Sutherland, and P. Nordlander, "Shedding Light on Dark Plasmons in Gold Nanorings," *Chemical Physics Letters*, vol. 458, no. 4–6, pp. 262–266, 2008.

[58] A. L. Koh *et al.*, "Electron Energy-Loss Spectroscopy (EELS) of Surface Plasmons in Single Silver Nanoparticles and Dimers: Influence of Beam Damage and Mapping of Dark Modes," *ACS Nano*, vol. 3, no. 10, pp. 3015–3022, 2009.

[59] Y. Wu and P. Nordlander, "Plasmon Hybridization in Nanoshells with a Nonconcentric Core," *Journal of Chemistry Physics*, vol. 125, no. 124708, 2006.

[60] S. Viarbitskaya *et al.*, "Plasmonic Hot Printing in Gold Nanoprisms," *ACS photonics*, vol. 2, no. 6, pp. 744–751, 2015.

[61] J. Larmor, "On a Dynamical Theory of the Electric and Luminiferous Medium," *Philosophical Transactions of the Royal Society A: Mathematical, Physical and Engineering Sciences*, vol. 190, pp. 205–300, 1897.

[62] J. G. Liu, H. Zhang, S. Link, and P. Nordlander, "Relaxation of plasmon-induced hot carriers," *Acs Photonics*, vol. 5, no. 7, pp. 2584–2595, 2017.

[63] J. B. Herzog, M. W. Knight, and D. Natelson, "Thermoplasmonics: quantifying plasmonic heating in single nanowires," *Nano letters*, vol. 14, no. 2, pp. 499–503, 2014.

[64] B. Luk'yanchuk *et al.*, "The Fano resonance in plasmonic nanostructures and metamaterials," *Nature materials*, vol. 9, no. 9, pp. 707–715, 2010.

[65] M. Frimmer, T. Coenen, and A. F. Koenderink, "Signature of a Fano resonance in a plasmonic metamolecule's local density of optical states," *Physical review letters*, vol. 108, no. 7, p. 077404, 2012.

[66] X. Li, D. Xiao, and Z. Zhang, "Landau damping of quantum plasmons in metal nanostructures," *New Journal of Physics*, vol. 15, no. 2, p. 023011, 2013.

[67] H. Inouye, K. Tanaka, I. Tanahashi, and K. Hirao, "Ultrafast dynamics of nonequilibrium electrons in a gold nanoparticle system," *Physical Review B*, vol. 57, no. 18, p. 11334, 1998.

[68] S. A. Hosseini Jebeli *et al.*, "Wavelength-Dependent Photothermal Imaging Probes Nanoscale Temperature Differences among Subdiffraction Coupled Plasmonic Nanorods," *Nano Letters*, 2021.

[69] Y. Jeliazova, M. Kayser, B. Mildner, A. W. Hassel, and D. Diesing, "Temperature stability of thin anodic oxide films in metal/insulator/metal structures: A comparison between tantalum and aluminium oxide," *Thin Solid Films*, vol. 500, no. 1–2, pp. 330–335, 2006.

[70] C. B. Duke, "Chapter 3, P 62," in *Tunneling in Solids*, New York: Academic, 1969.

[71] P. Thissen, B. Schindler, D. Diesing, and E. Hasselbrink, "Optical response of metal–insulator–metal heterostructures and their application for the detection of chemicurrents," *New Journal of Physics*, vol. 12, no. 11, p. 113014, 2010.

[72] A. Thon, M. Merschdorf, W. Pfeiffer, T. Klamroth, P. Saalfrank, and D. Diesing, "Photon-assisted tunneling versus tunneling of excited electrons in metal–insulator–metal junctions," *Applied Physics A*, vol. 78, no. 2, pp. 189–199, 2004.

[73] L. Goldin and G. Novikova, *Introduction to Quantum Physics*. Moscow, 1988.

[74] L. Landau, *Quantum Mechanics: Non-relativistic Theory*. EM Lifsihtz, 2013.

[75] J. G. Simmons, "Generalized formula for the electric tunnel effect between similar electrodes separated by a thin insulating film," *Journal of applied physics*, vol. 34, no. 6, pp. 1793–1803, 1963.

[76] J. G. Simmons, "Electric tunnel effect between dissimilar electrodes separated by a thin insulating film," *Journal of applied physics*, vol. 34, no. 9, pp. 2581–2590, 1963.

[77] P. Zhang, "Scaling for quantum tunneling current in nano-and subnano-scale plasmonic junctions," *Scientific reports*, vol. 5, no. 1, pp. 1–11, 2015.

[78] S. Banerjee and P. Zhang, "A generalized self-consistent model for quantum tunneling current in dissimilar metal-insulator-metal junction," *AIP Advances*, vol. 9, no. 8, p. 085302, 2019.

[79] F. B. Atar, E. Battal, L. E. Aygun, B. Daglar, M. Bayindir, and A. K. Okyay, "Plasmonically enhanced hot electron based photovoltaic device," *Optics express*, vol. 21, no. 6, pp. 7196–7201, 2013.

[80] F. Wang and N. A. Melosh, "Plasmonic energy collection through hot carrier extraction," *Nano letters*, vol. 11, no. 12, pp. 5426–5430, 2011.

[81] H. Chalabi, D. Schoen, and M. L. Brongersma, "Hot-electron photodetection with a plasmonic nanostripe antenna," *Nano letters*, vol. 14, no. 3, pp. 1374–1380, 2014.

[82] H. Park, A. K. Lim, A. P. Alivisatos, J. Park, and P. L. McEuen, "Fabrication of metallic electrodes with nanometer separation by electromigration," *Applied Physics Letters*, vol. 75, no. 2, pp. 301–303, 1999.

[83] J. Kern, R. Kullock, J. Prangsma, M. Emmerling, M. Kamp, and B. Hecht, "Electrically driven optical antennas," *Nature Photonics*, vol. 9, no. 9, pp. 582–586, 2015.

[84] M. N. Sadiku, "A simple introduction to finite element analysis of electromagnetic problems," *IEEE Transactions on education*, vol. 32, no. 2, pp. 85–93, 1989.

[85] D. Sullivan, J. Liu, and M. Kuzyk, "Three-dimensional optical pulse simulation using the FDTD method," *IEEE transactions on microwave theory and techniques*, vol. 48, no. 7, pp. 1127–1133, 2000.

[86] F. Paris, J. Canas, and J. Cañas, *Boundary element method: fundamentals and applications*. Oxford University Press, USA, 1997.

[87] D. R. Ward, D. A. Corley, J. M. Tour, and D. Natelson, "Vibrational and electronic heating in nanoscale junctions," *Nature nanotechnology*, vol. 6, no. 1, pp. 33–38, 2011.

[88] B. Y. Zheng, H. Zhao, A. Manjavacas, M. McClain, P. Nordlander, and N. J. Halas, "Distinguishing between plasmon-induced and photoexcited carriers in a device geometry," *Nature communications*, vol. 6, no. 1, pp. 1–7, 2015.

[89] Y. Li, M. L. Simeral, and D. Natelson, "Surface-enhanced infrared absorption of self-aligned nanogap structures," *The Journal of Physical Chemistry C*, vol. 120, no. 39, pp. 22558–22564, 2016.

[90] L. V. Brown, K. Zhao, N. King, H. Sobhani, P. Nordlander, and N. J. Halas, "Surface-enhanced infrared absorption using individual cross antennas tailored to chemical moieties," *Journal of the American Chemical Society*, vol. 135, no. 9, pp. 3688–3695, 2013.

[91] P. F. Liao and A. Wokaun, "Lightning rod effect in surface enhanced Raman scattering," *The Journal of Chemical Physics*, vol. 76, no. 1, pp. 751–752, 1982.

[92] S. A. Maier, *Plasmonics: fundamentals and applications*. Springer Science & Business Media, 2007.

[93] G. Mie, "Beiträge zur Optik trüber Medien, speziell kolloidaler Metallösungen," *Annalen der physik*, vol. 330, no. 3, pp. 377–445, 1908.

[94] P. B. Johnson and R.-Wjp. Christy, "Optical constants of the noble metals," *Physical review B*, vol. 6, no. 12, p. 4370, 1972.

[95] D. E. Aspnes and A. A. Studna, "Dielectric functions and optical parameters of si, ge, gap, gaas, gasb, inp, inas, and insb from 1.5 to 6.0 ev," *Physical review B*, vol. 27, no. 2, p. 985, 1983.

[96] I. H. Malitson, "Interspecimen comparison of the refractive index of fused silica," *Josa*, vol. 55, no. 10, pp. 1205–1209, 1965.

[97] A. Alabastri *et al.*, "Molding of plasmonic resonances in metallic nanostructures: Dependence of the non-linear electric permittivity on system size and temperature," *Materials*, vol. 6, no. 11, pp. 4879–4910, 2013.

[98] G. A. Maugin, *The thermomechanics of nonlinear irreversible behaviours*, vol. 27. World scientific, 1999.

[99] K.-C. Lee, S.-J. Lin, C.-H. Lin, C.-S. Tsai, and Y.-J. Lu, "Size effect of Ag nanoparticles on surface plasmon resonance," *Surface and Coatings Technology*, vol. 202, no. 22–23, pp. 5339–5342, 2008.

[100] F. Hao, C. L. Nehl, J. H. Hafner, and P. Nordlander, "Plasmon resonances of a gold nanostar," *Nano letters*, vol. 7, no. 3, pp. 729–732, 2007.

[101] C. F. Bohren, "How can a particle absorb more than the light incident on it?," *American Journal of Physics*, vol. 51, no. 4, pp. 323–327, 1983.

[102] G. P. Szakmany, A. O. Orlov, G. H. Bernstein, and W. Porod, "Shape engineering of antenna-coupled single-metal nanothermocouples," *Infrared Physics & Technology*, vol. 72, pp. 101–105, 2015.

[103] C. I. Evans *et al.*, "Detection of Trace Impurity Gradients in Noble Metals by the Photothermoelectric Effect," *The Journal of Physical Chemistry C*, 2021.

[104] C. I. Evans *et al.*, "Thermoelectric response from grain boundaries and lattice distortions in crystalline gold devices," *Proceedings of the National Academy of Sciences*, vol. 117, no. 38, pp. 23350–23355, 2020.

[105] E. Briones *et al.*, "Seebeck nanoantennas for the detection and characterization of infrared radiation," *Optics express*, vol. 22, no. 106, pp. A1538–A1546, 2014.

[106] K. W. Mauser *et al.*, "Resonant thermoelectric nanophotonics," *Nature nanotechnology*, vol. 12, no. 8, pp. 770–775, 2017.

[107] W. Liu, W. Wang, Z. Guan, and H. Xu, "A plasmon modulated photothermoelectric photodetector in silicon nanostripes," *Nanoscale*, vol. 11, no. 11, pp. 4918–4924, 2019.

[108] A. L. Hsu *et al.*, "Graphene-based thermopile for thermal imaging applications," *Nano letters*, vol. 15, no. 11, pp. 7211–7216, 2015.

[109] X. Cai *et al.*, "Sensitive room-temperature terahertz detection via the photothermoelectric effect in graphene," *Nature nanotechnology*, vol. 9, no. 10, pp. 814–819, 2014.

[110] T. J. Echtermeyer *et al.*, "Photothermoelectric and photoelectric contributions to light detection in metal–graphene–metal photodetectors," *Nano letters*, vol. 14, no. 7, pp. 3733–3742, 2014.

[111] M. González-Cardel, P. Arguijo, and R. Díaz-Uribe, "Gaussian beam radius measurement with a knife-edge: a polynomial approximation to the inverse error function," *Applied optics*, vol. 52, no. 16, pp. 3849–3855, 2013.

[112] M. Cattani, M. C. Salvadori, A. R. Vaz, F. S. Teixeira, and I. G. Brown, "Thermoelectric power in very thin film thermocouples: Quantum size effects," *Journal of Applied Physics*, vol. 100, no. 11, p. 114905, 2006.

[113] V. D. Das and N. Soundararajan, "Size and temperature effects on the Seebeck coefficient of thin bismuth films," *Physical Review B*, vol. 35, no. 12, p. 5990, 1987.

[114] C. Y. Ho, R. H. Bogaard, T. C. Chi, T. N. Havill, and H. M. James, "Thermoelectric power of selected metals and binary alloy systems," *Thermochimica acta*, vol. 218, pp. 29–56, 1993.

[115] S. F. Lin and W. F. Leonard, "Thermoelectric power of thin gold films," *Journal of Applied Physics*, vol. 42, no. 9, pp. 3634–3639, 1971.

[116] K. Fuchs, "The conductivity of thin metallic films according to the electron theory of metals," in *Mathematical Proceedings of the Cambridge Philosophical Society*, 1938, vol. 34, no. 1, pp. 100–108.

[117] M. Freitag, T. Low, and P. Avouris, "Increased responsivity of suspended graphene photodetectors," *Nano letters*, vol. 13, no. 4, pp. 1644–1648, 2013.

[118] D. Wu *et al.*, "Plasmon-enhanced photothermoelectric conversion in chemical vapor deposited graphene p–n junctions," *Journal of the American Chemical Society*, vol. 135, no. 30, pp. 10926–10929, 2013.

[119] Z. Fang, Z. Liu, Y. Wang, P. M. Ajayan, P. Nordlander, and N. J. Halas, "Graphene-antenna sandwich photodetector," *Nano letters*, vol. 12, no. 7, pp. 3808–3813, 2012.

[120] I. J. Luxmoore, P. Q. Liu, P. Li, J. Faist, and G. R. Nash, "Graphene–metamaterial photodetectors for integrated infrared sensing," *ACS photonics*, vol. 3, no. 6, pp. 936–941, 2016.

[121] L. Viti *et al.*, "Black phosphorus terahertz photodetectors," *Advanced Materials*, vol. 27, no. 37, pp. 5567–5572, 2015.

[122] M. Chen *et al.*, "Annealing temperature-dependent terahertz thermal–electrical conversion characteristics of three-dimensional microporous graphene," *ACS applied materials & interfaces*, vol. 11, no. 6, pp. 6411–6420, 2019.

[123] D. Sun *et al.*, "Ultrafast hot-carrier-dominated photocurrent in graphene," *Nature nanotechnology*, vol. 7, no. 2, pp. 114–118, 2012.

[124] F. J. Duarte, *Laser Pulse Phenomena and Applications*. BoD–Books on Demand, 2010.

[125] K.-J. Tielrooij *et al.*, "Generation of photovoltage in graphene on a femtosecond timescale through efficient carrier heating," *Nature nanotechnology*, vol. 10, no. 5, pp. 437–443, 2015.

[126] G. Ghione, *Semiconductor devices for high-speed optoelectronics*, vol. 116. Cambridge University Press Cambridge, 2009.

[127] J. C. Song, M. S. Rudner, C. M. Marcus, and L. S. Levitov, "Hot carrier transport and photocurrent response in graphene," *Nano letters*, vol. 11, no. 11, pp. 4688–4692, 2011.

[128] C. C. Williams and H. K. Wickramasinghe, "Microscopy of chemical-potential variations on an atomic scale," *Nature*, vol. 344, no. 6264, pp. 317–319, 1990.

[129] S. Cho *et al.*, "Thermoelectric imaging of structural disorder in epitaxial graphene," *Nature materials*, vol. 12, no. 10, pp. 913–918, 2013.

[130] E.-S. Lee, S. Cho, H.-K. Lyeo, and Y.-H. Kim, "Seebeck effect at the atomic scale," *Physical review letters*, vol. 112, no. 13, p. 136601, 2014.

[131] P. Reddy, S.-Y. Jang, R. A. Segalman, and A. Majumdar, "Thermoelectricity in molecular junctions," *Science*, vol. 315, no. 5818, pp. 1568–1571, 2007.

[132] K. Zhang, X. B. Pitner, R. Yang, W. D. Nix, J. D. Plummer, and J. A. Fan, "Single-crystal metal growth on amorphous insulating substrates," *Proceedings of the National Academy of Sciences*, vol. 115, no. 4, pp. 685–689, 2018.

[133] G. Langer, J. Hartmann, and M. Reichling, "Thermal conductivity of thin metallic films measured by photothermal profile analysis," *Review of Scientific Instruments*, vol. 68, no. 3, pp. 1510–1513, 1997.

[134] E. Pop, "Energy dissipation and transport in nanoscale devices," *Nano Research*, vol. 3, no. 3, pp. 147–169, 2010.

[135] M. S. Dresselhaus *et al.*, "New directions for low-dimensional thermoelectric materials," *Advanced materials*, vol. 19, no. 8, pp. 1043–1053, 2007.

[136] J. K. A. Amuzu, "The effect of tensile stress on the thermoelectric EMF in copper, gold, and silver," *physica status solidi (a)*, vol. 63, no. 1, pp. K7–K10, 1981.

[137] A. J. Forty, "Direct observations of dislocations in crystals," *Advances in Physics*, vol. 3, no. 9, pp. 1–25, 1954.

[138] C. A. Domenicali and F. A. Otter, "Thermoelectric power and electron scattering in metal alloys," *Physical Review*, vol. 95, no. 5, p. 1134, 1954.

[139] R. P. Huebener and C. Van Baarle, "Thermoelectric Power of Annealed and Quenched Gold-Platinum Alloys," *Physical Review*, vol. 159, no. 3, p. 564, 1967.

[140] R. P. Huebner and C. Van Baarle, "Thermoelectric power of annealed and quenched gold-platinum alloys at low temperatures," *Physics Letters*, vol. 23, no. 3, pp. 189–190, 1966.

[141] D. J. Frank, R. H. Dennard, E. Nowak, P. M. Solomon, Y. Taur, and H.-S. P. Wong, "Device scaling limits of Si MOSFETs and their application dependencies," *Proceedings of the IEEE*, vol. 89, no. 3, pp. 259–288, 2001.

[142] J. Tersoff and D. R. Hamann, "Theory of the scanning tunneling microscope," *Physical Review B*, vol. 31, no. 2, p. 805, 1985.

[143] V. Enaldiev, A. Bylinkin, and D. Svintsov, "Plasmon-assisted resonant tunneling in graphene-based heterostructures," *Physical Review B*, vol. 96, no. 12, p. 125437, 2017.

[144] D. A. Kovacs, J. Winter, S. Meyer, A. Wucher, and D. Diesing, "Photo and particle induced transport of excited carriers in thin film tunnel junctions," *Physical Review B*, vol. 76, no. 23, p. 235408, 2007.

[145] K. J. Savage, M. M. Hawkeye, R. Esteban, A. G. Borisov, J. Aizpurua, and J. J. Baumberg, "Revealing the quantum regime in tunnelling plasmonics," *Nature*, vol. 491, no. 7425, pp. 574–577, 2012.

[146] M. S. Tame, K. R. McEnery, Ş. Özdemir, J. Lee, S. A. Maier, and M. S. Kim, "Quantum plasmonics," *Nature Physics*, vol. 9, no. 6, pp. 329–340, 2013.

[147] H. Hertz, "Ueber einen Einfluss des ultravioletten Lichtes auf die electrische Entladung," *Annalen der Physik*, vol. 267, no. 8, pp. 983–1000, 1887.

[148] T. P. White and K. R. Catchpole, "Plasmon-enhanced internal photoemission for photovoltaics: theoretical efficiency limits," *Applied Physics Letters*, vol. 101, no. 7, p. 073905, 2012.

[149] J. G. Endriz and W. E. Spicer, "Surface-plasmon-one-electron decay and its observation in photoemission," *Physical Review Letters*, vol. 24, no. 2, p. 64, 1970.

[150] C. N. Berglund and W. E. Spicer, "Photoemission studies of copper and silver: theory," *Physical Review*, vol. 136, no. 4A, p. A1030, 1964.

[151] G. Baffou, R. Quidant, and F. J. García de Abajo, "Nanoscale control of optical heating in complex plasmonic systems," *ACS nano*, vol. 4, no. 2, pp. 709–716, 2010.

[152] L. Brus, "Noble metal nanocrystals: plasmon electron transfer photochemistry and single-molecule Raman spectroscopy," *Accounts of chemical research*, vol. 41, no. 12, pp. 1742–1749, 2008.

[153] M. Bonn *et al.*, "Phonon-versus electron-mediated desorption and oxidation of CO on Ru (0001)," *Science*, vol. 285, no. 5430, pp. 1042–1045, 1999.

[154] D. W. Peters, "An infrared detector utilizing internal photoemission," *Proceedings of the IEEE*, vol. 55, no. 5, pp. 704–705, 1967.

[155] S. Faris, T. Gustafson, and J. Wiesner, "Detection of optical and infrared radiation with DC-biased electron-tunneling metal-barrier-metal diodes," *IEEE Journal of Quantum Electronics*, vol. 9, no. 7, pp. 737–745, 1973.

[156] M. Heiblum, S. Wang, J. Whinnery, and T. Gustafson, "Characteristics of integrated MOM junctions at dc and at optical frequencies," *IEEE Journal of Quantum Electronics*, vol. 14, no. 3, pp. 159–169, 1978.

[157] J. Chen, G. A. Smolyakov, S. R. Brueck, and K. J. Malloy, "Surface plasmon modes of finite, planar, metal-insulator-metal plasmonic waveguides," *Optics express*, vol. 16, no. 19, pp. 14902–14909, 2008.

[158] J. Jacob, A. Babu, G. Mathew, and V. Mathew, "Propagation of surface plasmon polaritons in anisotropic MIM and IMI structures," *Superlattices and microstructures*, vol. 44, no. 3, pp. 282–290, 2008.

[159] M. G. Nielsen, A. Pors, O. Albrektsen, and S. I. Bozhevolnyi, "Efficient absorption of visible radiation by gap plasmon resonators," *Optics express*, vol. 20, no. 12, pp. 13311–13319, 2012.

[160] C. Wadell, T. J. Antosiewicz, and C. Langhammer, "Optical absorption engineering in stacked plasmonic Au–SiO2–Pd nanoantennas," *Nano letters*, vol. 12, no. 9, pp. 4784–4790, 2012.

[161] Z. Burshtein and J. Levinson, "Photo-induced tunnel currents in Al-Al 2 O 3-Au structures," *Physical Review B*, vol. 12, no. 8, p. 3453, 1975.

[162] W. E. Spicer, "Photoemissive, photoconductive, and optical absorption studies of alkali-antimony compounds," *Physical review*, vol. 112, no. 1, p. 114, 1958.

[163] W. E. Spicer, "Negative affinity 3–5 photocathodes: Their physics and technology," *Applied physics*, vol. 12, no. 2, pp. 115–130, 1977.

[164] R. H. Fowler, "The analysis of photoelectric sensitivity curves for clean metals at various temperatures," *Physical review*, vol. 38, no. 1, p. 45, 1931.

[165] W. G. Spitzer, C. R. Crowell, and M. M. Atalla, "Mean free path of photoexcited electrons in Au," *Physical Review Letters*, vol. 8, no. 2, p. 57, 1962.

[166] H. Kanter, "Slow-electron mean free paths in aluminum, silver, and gold," *Physical Review B*, vol. 1, no. 2, p. 522, 1970.

[167] D. Bejan, "Ballistic electron distribution for hot electron in metals," *Romanian Reports in Physics*, vol. 58, no. 2, p. 149, 2006.

[168] R. L. Olmon *et al.*, "Optical dielectric function of gold," *Physical Review B*, vol. 86, no. 23, p. 235147, 2012.

[169] S. M. Sze, J. L. Moll, and T. Sugano, "Range-energy relation of hot electrons in gold," *Solid-state electronics*, vol. 7, no. 7, pp. 509–523, 1964.

[170] M. W. Knight *et al.*, "Embedding plasmonic nanostructure diodes enhances hot electron emission," *Nano letters*, vol. 13, no. 4, pp. 1687–1692, 2013.

[171] Y. K. Lee, C. H. Jung, J. Park, H. Seo, G. A. Somorjai, and J. Y. Park, "Surface plasmon-driven hot electron flow probed with metal-semiconductor nanodiodes," *Nano letters*, vol. 11, no. 10, pp. 4251–4255, 2011.

[172] A. Giugni *et al.*, "Hot-electron nanoscopy using adiabatic compression of surface plasmons," *Nature nanotechnology*, vol. 8, no. 11, pp. 845–852, 2013.

[173] K. Watanabe, D. Menzel, N. Nilius, and H.-J. Freund, "Photochemistry on metal nanoparticles," *Chemical reviews*, vol. 106, no. 10, pp. 4301–4320, 2006.

[174] T. Inagaki, K. Kagami, and E. T. Arakawa, "Photoacoustic observation of nonradiative decay of surface plasmons in silver," *Physical Review B*, vol. 24, no. 6, p. 3644, 1981.

[175] M. Kornbluth, A. Nitzan, and T. Seideman, "Light-induced electronic non-equilibrium in plasmonic particles," *The Journal of chemical physics*, vol. 138, no. 17, p. 174707, 2013.

[176] D. R. Ward, F. Hüser, F. Pauly, J. C. Cuevas, and D. Natelson, "Optical rectification and field enhancement in a plasmonic nanogap," *Nature nanotechnology*, vol. 5, no. 10, pp. 732–736, 2010.

[177] R. Esteban, A. G. Borisov, P. Nordlander, and J. Aizpurua, "Bridging quantum and classical plasmonics with a quantum-corrected model," *Nature communications*, vol. 3, no. 1, pp. 1–9, 2012.

[178] R. Esteban *et al.*, "A classical treatment of optical tunneling in plasmonic gaps: extending the quantum corrected model to practical situations," *Faraday discussions*, vol. 178, pp. 151–183, 2015.

[179] N. E. Christensen, "Spin-orbit projected d densities-of-states of Pd, Ag, Pt, and Au," *Journal of Physics F: Metal Physics*, vol. 8, no. 3, p. L51, 1978.

[180] D. C. Marinica, A. K. Kazansky, P. Nordlander, J. Aizpurua, and A. G. Borisov, "Quantum plasmonics: nonlinear effects in the field enhancement of a plasmonic nanoparticle dimer," *Nano letters*, vol. 12, no. 3, pp. 1333–1339, 2012.

[181] W. Zhu *et al.*, "Quantum mechanical effects in plasmonic structures with subnanometre gaps," *Nature communications*, vol. 7, no. 1, pp. 1–14, 2016.

[182] R. Chikkaraddy *et al.*, "Single-molecule strong coupling at room temperature in plasmonic nanocavities," *Nature*, vol. 535, no. 7610, pp. 127–130, 2016.

[183] P. Wang, A. V. Krasavin, M. E. Nasir, W. Dickson, and A. V. Zayats, "Reactive tunnel junctions in electrically driven plasmonic nanorod metamaterials," *Nature nanotechnology*, vol. 13, no. 2, pp. 159–164, 2018.

[184] L. Zhou *et al.*, "Quantifying hot carrier and thermal contributions in plasmonic photocatalysis," *Science*, vol. 362, no. 6410, pp. 69–72, 2018.

[185] J. Yang, R. Faggiani, and P. Lalanne, "Light emission in nanogaps: overcoming quenching," *Nanoscale horizons*, vol. 1, no. 1, pp. 11–13, 2016.

[186] F. Bigourdan, J.-P. Hugonin, F. Marquier, C. Sauvan, and J.-J. Greffet, "Nanoantenna for electrical generation of surface plasmon polaritons," *Physical review letters*, vol. 116, no. 10, p. 106803, 2016.

[187] Y. Zhu, L. Cui, and D. Natelson, "Hot-carrier enhanced light emission: The origin of above-threshold photons from electrically driven plasmonic tunnel junctions," *Journal of Applied Physics*, vol. 128, no. 23, p. 233105, 2020.

[188] M. Buret *et al.*, "Spontaneous hot-electron light emission from electron-fed optical antennas," *Nano letters*, vol. 15, no. 9, pp. 5811–5818, 2015.

[189] R. Zhang *et al.*, "How to identify plasmons from the optical response of nanostructures," *ACS nano*, vol. 11, no. 7, pp. 7321–7335, 2017.

[190] H. Aouani *et al.*, "Crucial role of the adhesion layer on the plasmonic fluorescence enhancement," *ACS nano*, vol. 3, no. 7, pp. 2043–2048, 2009.

[191] T. G. Habteyes *et al.*, "Metallic adhesion layer induced plasmon damping and molecular linker as a nondamping alternative," *ACS nano*, vol. 6, no. 6, pp. 5702–5709, 2012.

[192] K. J. Palm, J. B. Murray, T. C. Narayan, and J. N. Munday, "Dynamic optical properties of metal hydrides," *Acs Photonics*, vol. 5, no. 11, pp. 4677–4686, 2018.

[193] S. Kadkhodazadeh, F. A. A. Nugroho, C. Langhammer, M. Beleggia, and J. B. Wagner, "Optical property–composition correlation in noble metal alloy nanoparticles studied with EELS," *ACS Photonics*, vol. 6, no. 3, pp. 779–786, 2019.

[194] C. Ott, S. Götzinger, and H. B. Weber, "Thermal origin of light emission in nonresonant and resonant nanojunctions," *Physical Review Research*, vol. 2, no. 4, p. 042019, 2020.

[195] F. G. De Abajo, "Optical excitations in electron microscopy," *Reviews of modern physics*, vol. 82, no. 1, p. 209, 2010.

[196] Y.-Y. Cai *et al.*, "Anti-Stokes emission from hot carriers in gold nanorods," *Nano letters*, vol. 19, no. 2, pp. 1067–1073, 2019.

[197] D. Natelson, "Mechanical break junctions: Enormous information in a nanoscale package," *ACS nano*, vol. 6, no. 4, pp. 2871–2876, 2012.

[198] W. Cai *et al.*, "Thermal transport in suspended and supported monolayer graphene grown by chemical vapor deposition," *Nano letters*, vol. 10, no. 5, pp. 1645–1651, 2010.

[199] P. Wei, W. Bao, Y. Pu, C. N. Lau, and J. Shi, "Anomalous thermoelectric transport of Dirac particles in graphene," *Physical review letters*, vol. 102, no. 16, p. 166808, 2009.

[200] J. Yan *et al.*, "Dual-gated bilayer graphene hot-electron bolometer," *Nature nanotechnology*, vol. 7, no. 7, pp. 472–478, 2012.

[201] S.-F. Shi, X. Xu, D. C. Ralph, and P. L. McEuen, "Plasmon resonance in individual nanogap electrodes studied using graphene nanoconstrictions as photodetectors," *Nano letters*, vol. 11, no. 4, pp. 1814–1818, 2011.

[202] B. Sepúlveda, J. B. González-Díaz, A. García-Martín, L. M. Lechuga, and G. Armelles, "Plasmon-induced magneto-optical activity in nanosized gold disks," *Physical review letters*, vol. 104, no. 14, p. 147401, 2010.

[203] A. D. Rakić, "Algorithm for the determination of intrinsic optical constants of metal films: application to aluminum," *Applied optics*, vol. 34, no. 22, pp. 4755–4767, 1995.

[204] K. M. McPeak *et al.*, "Plasmonic films can easily be better: rules and recipes," *ACS photonics*, vol. 2, no. 3, pp. 326–333, 2015.

[205] M. A. Ordal, R. J. Bell, R. W. Alexander, L. A. Newquist, and M. R. Querry, "Optical properties of Al, Fe, Ti, Ta, W, and Mo at submillimeter wavelengths," *Applied optics*, vol. 27, no. 6, pp. 1203–1209, 1988.

[206] M. W. Knight, N. S. King, L. Liu, H. O. Everitt, P. Nordlander, and N. J. Halas, "Aluminum for plasmonics," *ACS nano*, vol. 8, no. 1, pp. 834–840, 2014.

Appendix A

A.1. **Fabrication notes**

The main challenge in fabricating Au-Pt devices was that after fabricating Pt, the film had elevated edges as shown below that prevented Au film to be electrically connected to the Pt film. The source of the sputterer is at an angle with the sample and that causes these edges to form. Double layer PMMA with different thicknesses for the layers have been tested. Some ratios of thicknesses help with reducing the edge but not removing them. Solution that works is to use a thin layer of PMMA (950A2 at 4000rpm) and turn off the rotation of the sample in the sputter. The sample should be aligned in a way that the nanowire points to the Pt source in the sputterer. If the PMMA is thick, then by turning off the rotation, the thickness of the film at the nanowire gets very thin and the film wouldn't have good quality for our measurements.

Recipe for fabricating pure Au- pure Pt devices:

Clean the chip (already prepared with gold pads and diced using dicing saw) by 5 min sonicating in acetone, soaking in IPA and blow dry. Then clean the chip using plasma cleaning @medium power for 5 minutes. Use PMMA 950A2 at 4000 rpm for 40 seconds, post bake at 180 degrees (200 degrees on our hot plate) for 1 min. Do the electron lithography using Elionix with settings of 3 by 3 for pitch number and 1300 $\mu C/cm^2$ for area dose for Pt side electrodes. Note that your

writing file should have at least 2 alignment marks so they can be used in the second lithography step. Develop with PMMA developer (3:1 ratio) for 1 min. Soak in IPA and blow dry. Plasma clean for 5 seconds at low power right before sputtering Pt for stronger adhesion. Use sputtering for Pt. Load the sample in a way that finding the direction of the device is easy after loading the sample in. You can load as shown below so that once you find the screws on the sample holder, you know the direction of your device. You must align the Pt source in a way that Pt source would be in the direction of your Pt nanowire then you must turn off the rotation on the sputter and use my recipe for Pt in the sputter computer to sputter ~20 nm Pt.

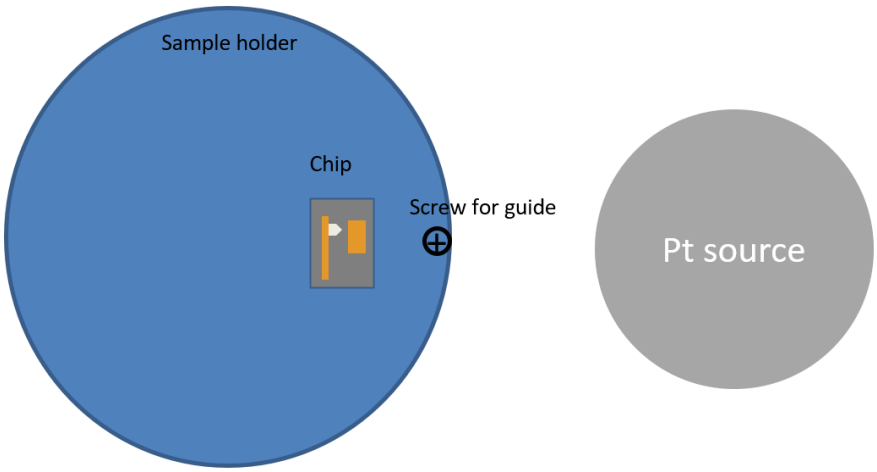

Note that if you do not turn off the rotation or if the source is not in the direction of the nanowire, the film will have raised edges and the fabrication might fail when evaporating Au in the next step. You can see examples film edges after lift off of the first layer below.

Soak the sample in acetone for ~3 hours or more and use acetone for lift off. Note that even when using pure Pt devices (without adhesion layer), during lift off you can sonicate your sample in acetone for ~5 seconds and the film won't come off as long as the film has got properly cleaned in previous steps.

For the second step of lithography (pure Au layer), we should use double layer PMMA. You can plasma clean the sample for 10 s at medium. Use PMMA 495 on plan A, bake @200◦C for 50 seconds, for the second layer, use PMMA 950C4 on plan J and bake @210 ◦C for 1 min. In lithography process using Elionix use 3 by 3 for pitch numbers and 2200 $\mu C/cm^2$ for area dose and use alignemnt marks from previous lithography to align your pattern. After develpement, evaporate 18 nm gold (without adhesion layer). After soaking the sample in acetone for ~3 hours or more, very gently do the lift off and do not use sonication for this step otherwise the gold film lifts off from the Pt surface and the electrical connection fails.

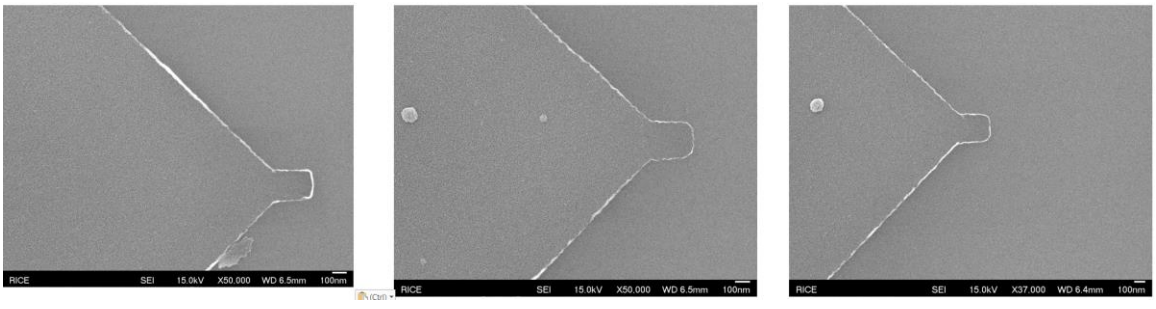

Other than Au-Pt, Au-Mo and Au-Pd devices have also been fabricated. Au-Mo devices are always open due to oxidization of Mo on the surface that prevents the Au film to be electrically connected. Au-Pd devices are shown below, form the third

metal (their alloy) in the middle and after electromigration, and there is no clear gap:

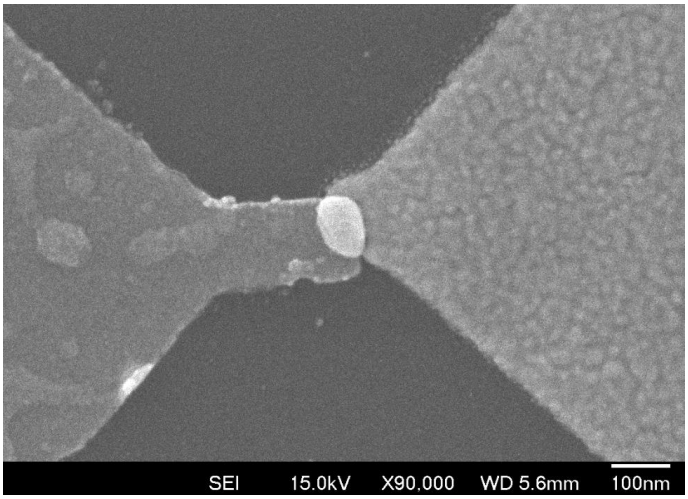

Electromigration direction: when the pure gold devices are measured after two days in ambient conditions, the electromigration gets harder because the device gets annealed. The electromigration with the same wiring shown in Fig. 6.8, can cause the nanogap to be formed at the wider end of the nanowire:

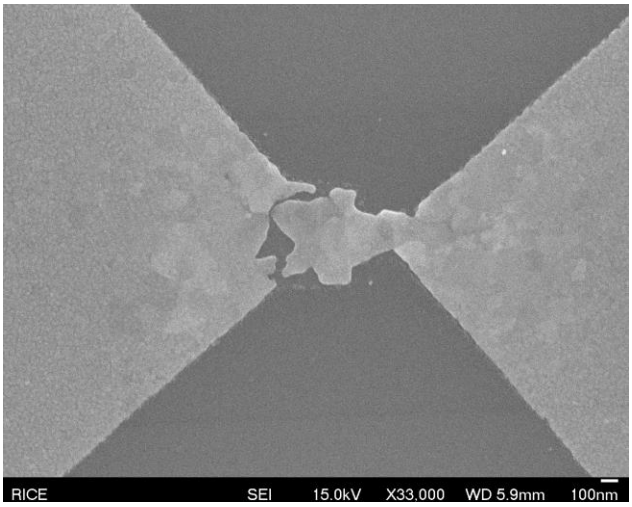

A.2. Simulation notes

Simulation projects useful for future applications.

A.2.1. Propagating SSPs dimensions for 1060 nm wavelengths

In this section, the propagations of SPPs are modeled in 2D. The symmetry is broken by adding gratings to the gold bowtie structure, so, the SPPs can be excited. In this 2D model, a Gaussian beam with wavelength and diameter that matches with experiments is applied to the middle of the grating structure. The gratings' widths and distance between them are parameters in change to find the best design for the most efficient SPP generation. The energy flux in this model is probed at a fixed spot several microns away from the grating.

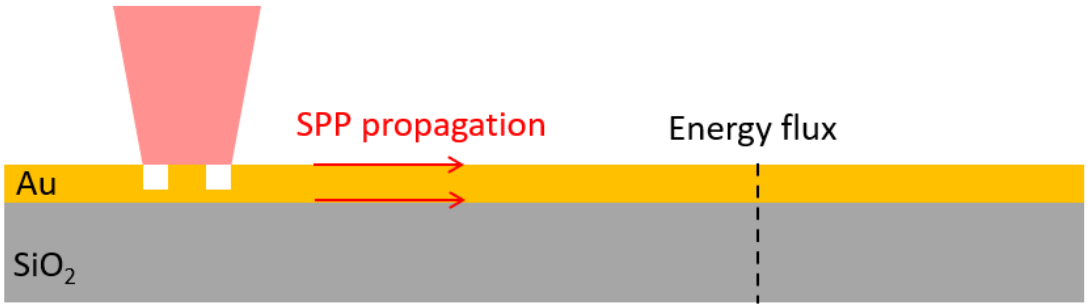

Here we show the results for two gratings with optical wavelength of 785nm. D is the slit width. Maximum flux is almost at D=250nm and distance between two slits 250nm:

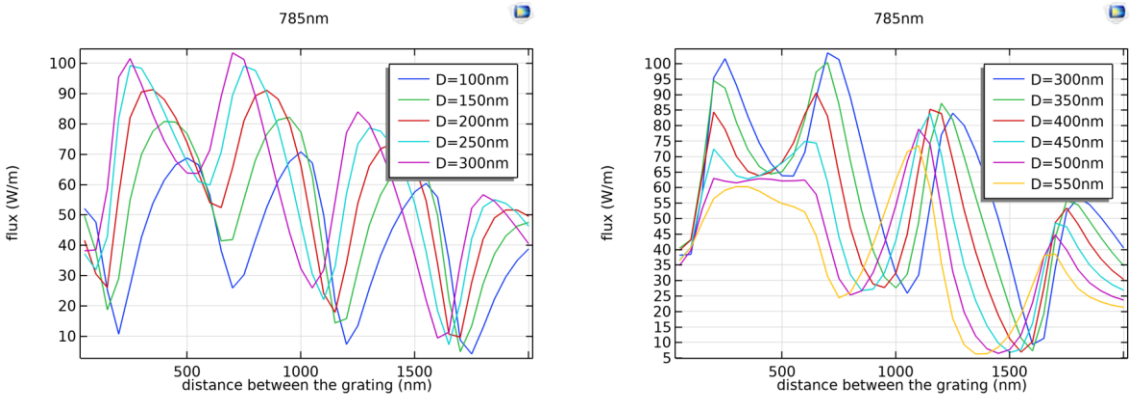

Here we show the results for two gratings with optical wavelength of 1060nm. D is the slit width. Best flux is almost at D=370nm and distance between two slits 380nm:

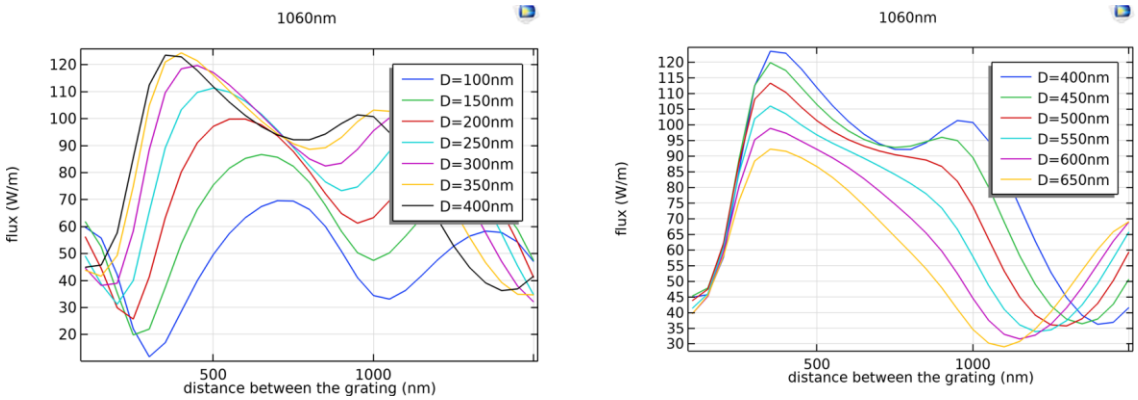

The wavelength of the SPP can be calculated as:

$$\lambda_{SPP} = \frac{2\pi}{k_x{}'}$$

In which

$$k_x = k'_x + ik''_x$$

$$k'_x = \frac{\omega}{c}\sqrt{\frac{\varepsilon'_m \varepsilon_d}{\varepsilon'_m + \varepsilon_d}}$$

And

$$k''_x = \frac{\omega}{c}\sqrt{\frac{\varepsilon'_m \varepsilon_d}{\varepsilon'_m + \varepsilon_d}}\frac{\varepsilon''_m \varepsilon_d}{2\varepsilon'_m(\varepsilon'_m + \varepsilon_d)}$$

Note: *m* and *d* refer to metal and dielectric, respectively.

One might think if we design Bragg reflectors in-plane and out of two metals in the distance between grating and the nanowire, it might make a strong standing SPP wave at the nanowire. But because the refractive index of metals is small, the width of in-plane metallic structures gets large ($\lambda/4n$). The other SPPs decay rapidly. As expected, simulation results show that when the imaginary part of permittivity in this proposed structure is zero, there will be strong field enhancement in the nanowire but in reality (non-zero imaginary part of permittivity), there will be no field enhancement at the nanowire.

A.2.2. Thickness of SiO2 and coupling with the incoming light

This simulation shows the energy flux probed at the SiO_2 and Si boundary. In this model, the thickness of Si is infinite and the thickness of SiO_2 is in change. If device preparation, during wire bonding the chip, if the needle pierces through the SiO_2, when light is shined close to that particular device (and not hitting the device), an open circuit voltage is measured due to coupling of light to the charge carriers in

Si. Overall, if the thickness of SiO_2 is greater, the wire bonding process is safer, but very thick SiO_2 layer can reduce the resolution during electron lithography. This simulation can help find the optimum thickness for SiO2 for 785nm and 1060nm.

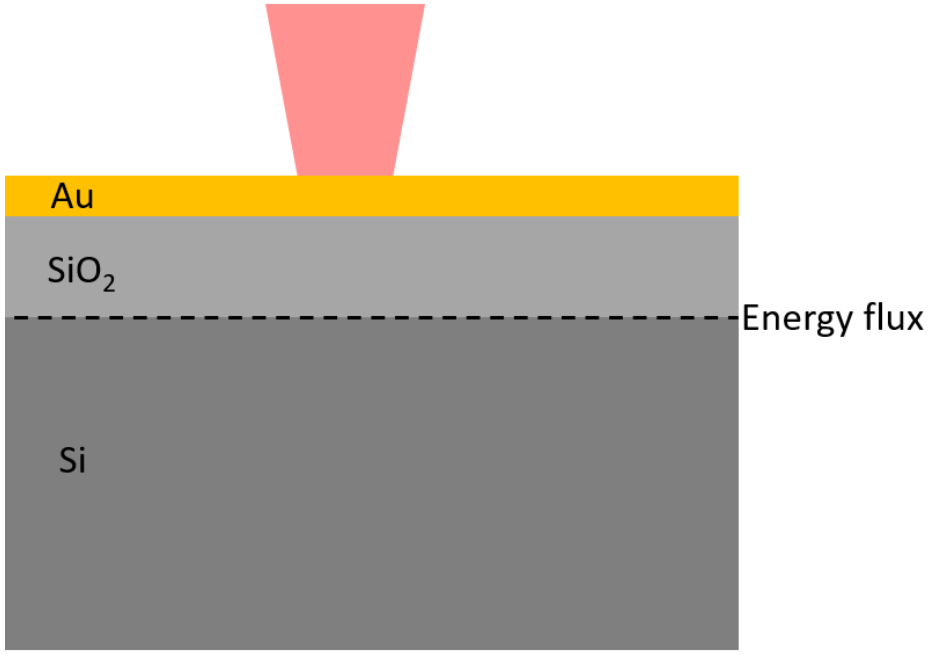

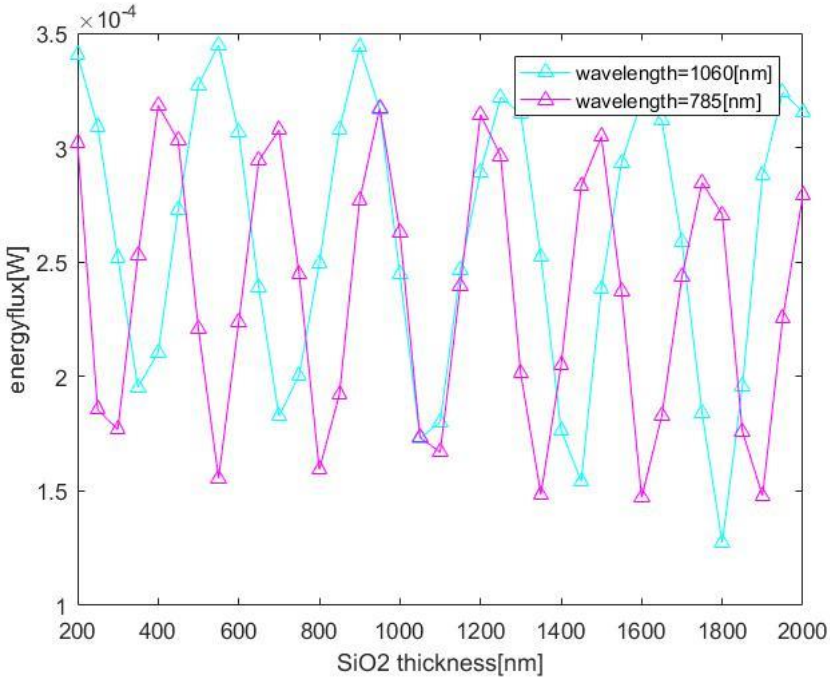

A2.3. Static B field effect on Plasmons

Simulation results of how static B field in z direction changes the surface charge distribution in metallic nanostructures.

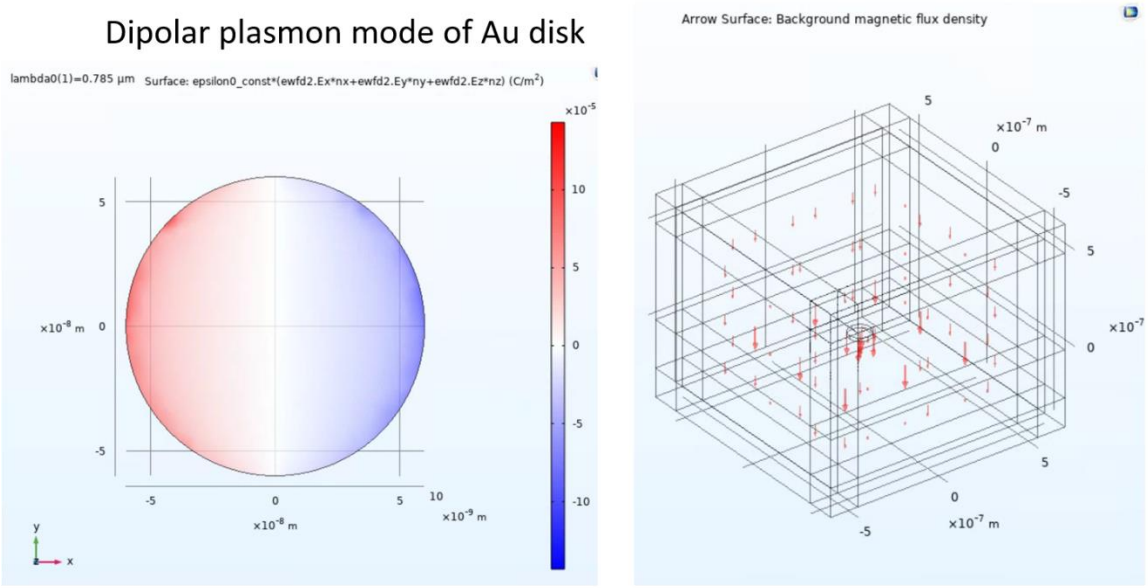

Ways of coupling static B field to ewfd physics interface in COMSOL.

1- Similar to Ref [202], permittivity tensor can be defined. The B field changes the cyclotron frequency and so the off-diagonal permittivity. All calculation is solved in one ewfd physics interface.In this implementation, the surface change distribution changes just for 0.7 degrees even under very high static field of 800 T.

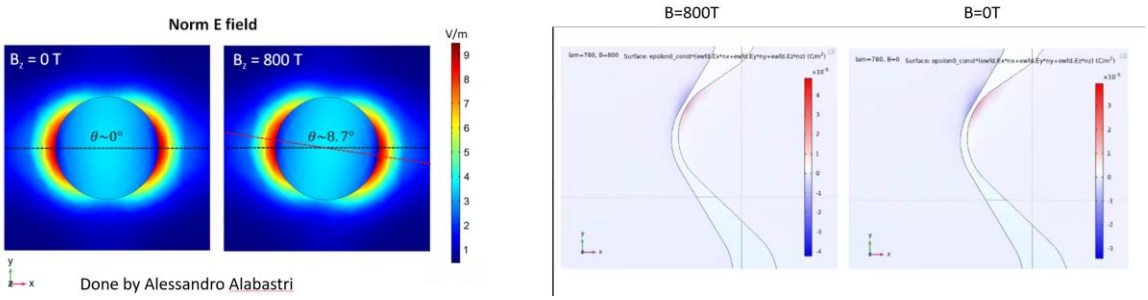

2- by coupling the ewfd model to magnetic field (mf) physics interface:

In this method, ewfd and mf physics interfaces are coupled together. In ewfd, the initial surface charge distribution is calculated, the static B field is applied to the module through mf physic interface. The physics interfaces are coupled together by defining a charge density distribution as an input in mf physics interface. This charge density is calculated in ewfd module.

A.2.4. Surface map with PTE measurements

PTE measurements can be used as a method to map out the simple structural change in the surface of the device. For example, in the case of having a step along x direction in a gold film in x-y plane, the PTE map of the structure while using y polarized light can show some characteristics of the step in the surface of the device. The width of the step should be wide enough to let us characterize the edge properly (based on the laser spot size and thermal conductivity of the film). The reason for this behavior is that by using perpendicular polarization, the interaction of light with the edge of the step increases and due to some defect on the surface of the film near the edge of the step, the scattering pattern of the film changes and so does the Seebeck coefficient. As a result, we could use PTE measurements as a method to create a surface map. This behavior is modeled using simulations by coupling ewfd, ht, and ec physics interfaces in COMSOL.

A.2.5. Width dependent simulations for Au, Al and Ag nanowires

Absorption cross section for different nanowires at different wavelengths. These data may be used for finding the best width of the nanowire based on wavelength and material.

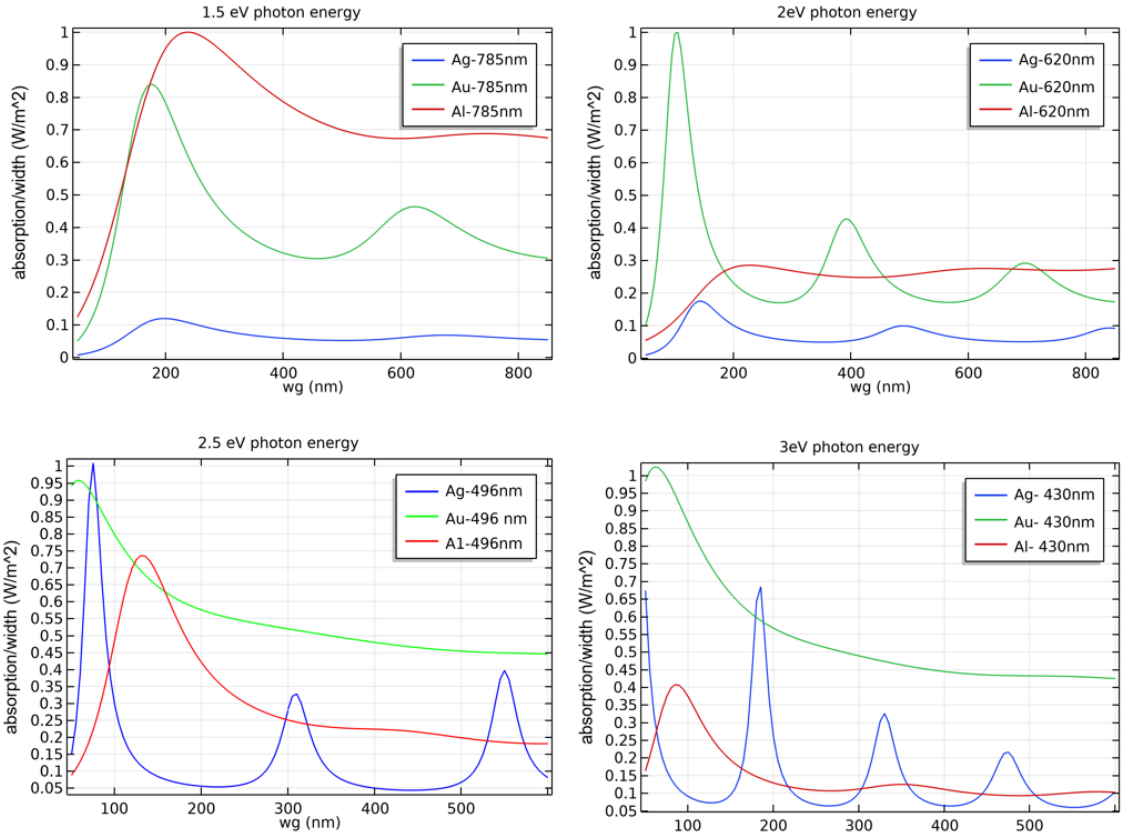

A.2.6. Nanogap in Al wire using different geometries and references for permittivity

Field enhancements in the nanogap of Al nanowire are simulated and shown below. The gap size for Fig. a is 3 nm. The geometry for all three others is the same with 1 nm gap size using different references as permittivity for Al. As it is shown, the

spectrum does not drastically change using same geometry. Figures b-d correspond to Refs [203]–[205] for Al permittivity, respectively.

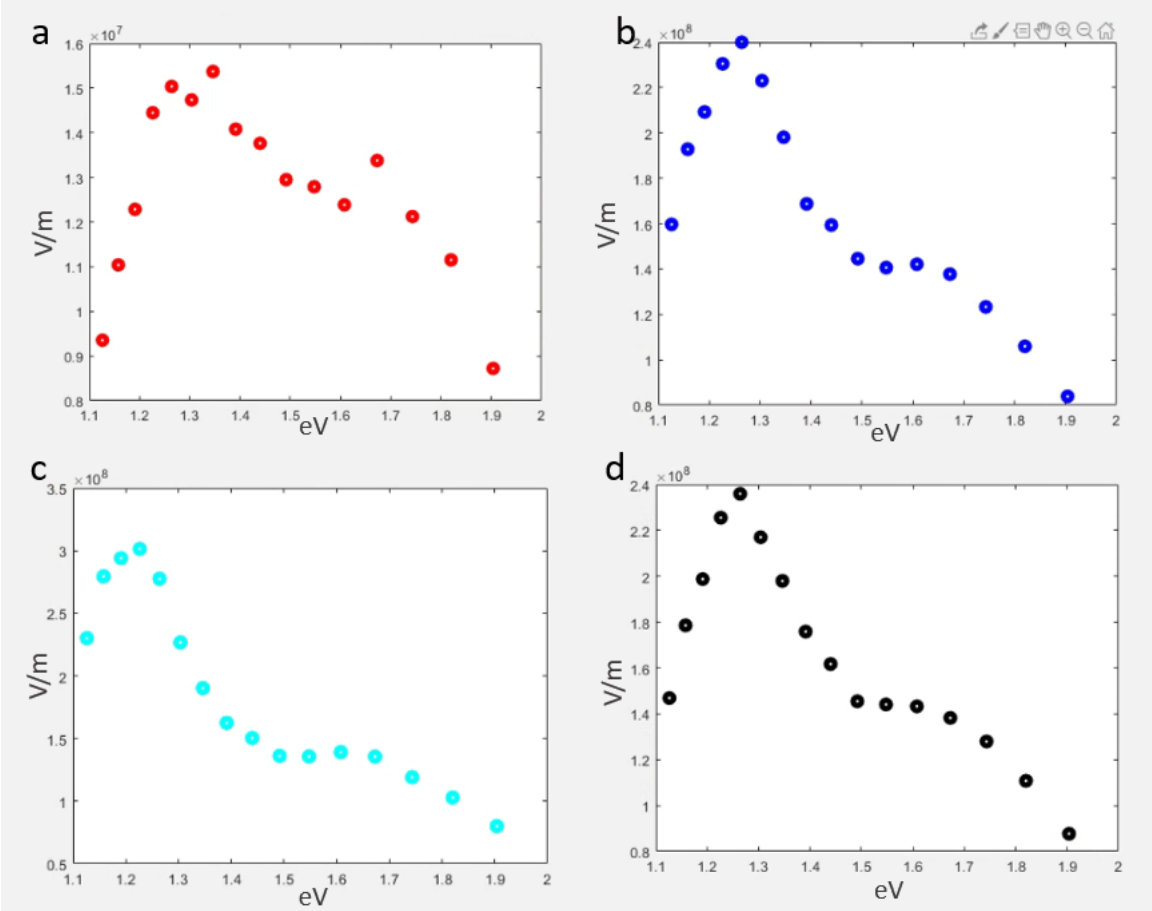

Adding oxide on top should red-shift the spectrum. The spectrum for a cross section of a wire is shown below. The results are similar to Ref [206].

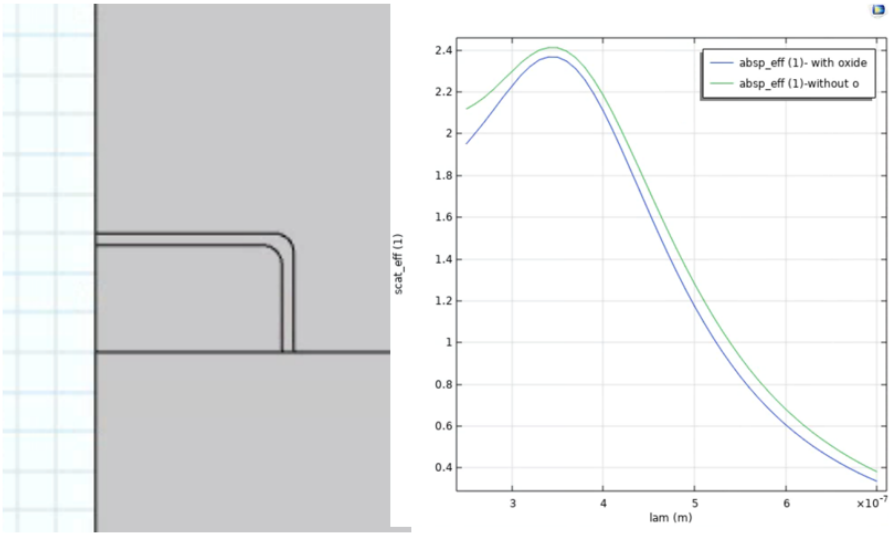

A.3. Andor iXon3 Camera notes

For using the Andor iXon3 camera, these steps need to be taken:

The controller card needs to be installed in the PCI or PCI express slot in the motherboard of the computer. The new version of the controller card, CCI-24, is installed in my PC in the lab. The older version controller card, CCI-23, is installed in the old case next to my PC case in our lab. Proper cables that are in the box of the camera will connect this controller card to the camera.

The micromanagers should be downloaded and installed in the computer. (I've done it on my computer in the lab):

For 64-bit computer: https://valelab4.ucsf.edu/~MM/nightlyBuilds/2.0.0-gamma/Windows/MMSetup_64bit_2.0.0-gamma1_20200615.exe

For 32-bit computer: https://valelab4.ucsf.edu/~MM/nightlyBuilds/2.0.0-gamma/Windows/MMSetup_32bit_2.0.0-gamma1_20200615.exe

Then the drivers need to be installed: (Done on my PC in the lab):

https://oxinst-my.sharepoint.com/:u:/g/personal/m_khan_andor_com/EVWtiiZYs39BmP9swPhk87MBp_EQQq-3XAvtDEewuD8OTg?e=6Vju9Q

Note that the camera is super sensitive to light. Make sure the c-mount cap of the camera is used and the inside shutter is closed whenever camera is not used. Please refer to:

https://physiology.case.edu/media/eq_manuals/eq_manual_ixon3_hardware_guide.pdf

and

http://www.mvi-inc.com/wp-content/uploads/Andor_iXon_897_Specifications.pdf

As a software interface, you can use the opensource software to control all the camera features:

https://valelab4.ucsf.edu/~MM/nightlyBuilds/2.0.0-gamma/Windows/MMSetup_64bit_2.0.0-gamma1_20210224.exe